ABSTRACT

Hadroproduction of Charm Mesons

Andrew Faulkner Wallace
Yale University
May 1997

We measure forward and differential cross-sections, the latter with respect to Feynman-x (x_F) and transverse momentum (p_T), for production of D^+, D^0, D_s, and D^{*+} in collisions of $\pi^\pm$, $K^\pm$, and p on a nuclear target. These results provide unique information on the beam dependence of charm production. In addition to significant high-statistics contributions to current knowledge on π^- and p-induced production, we present the first precise K^- beam measurements as well as the only measurements for π^+ and K^+. These results are compared to predictions of next-to-leading order (NLO) perturbative QCD using modern parametrizations of the pion and nucleon parton distributions. Production induced by different beam particles is found to be the same within statistics. Strange final states are seen to contribute appreciably to the total charm cross-section, which our measurements indicate is larger than but consistent with QCD predictions. The energy dependence mapped out by these and previous measurements is consistent with theory. We observe in the shapes of the differential cross-sections the differences expected in production induced by projectiles with different gluon distributions, harder distributions being indicated for mesons than for protons. Leading-particle asymmetry measurements for K and p-induced charm production are also presented.

Hadroproduction of Charm Mesons

A Dissertation
Presented to the Faculty of the Graduate School
of
Yale University
in Candidacy for the Degree of
Doctor of Philosophy

By
Andrew Faulkner Wallace

Dissertation Director: Paul Karchin

May 1997

© Copyright 1997

by

Andrew Faulkner Wallace

All Rights Reserved

Acknowledgements

First and foremost, I'd like to thank my advisor Paul Karchin for all of the wisdom, good will, forbearance, and friendship he has shown these many years. I have enjoyed what I consider a very rewarding and fruitful experience in the physics department at Yale, and for this Paul deserves much of the credit.

Next, I'd like to thank the other members of my thesis committee: Profs. Michael Schmidt, Shiva Kumar, Alan Chodos, and Steve Manly. My gratitude also goes to Prof. Julia Thompson of the University of Pittsburgh, who served as my outside reader.

I consider myself lucky to have worked in the E769 collaboration. My research has depended from the beginning on the groundwork laid by its members, many of whom had moved on by the time I showed up and whom consequently I never met. In addition to these people, I would like to thank the "core" group whose expertise and good humor made coming out to Fermilab for group meetings a pleasure: Jeff Appel, Marleigh Sheaff, Austin Napier, Jeff Spalding, Simon Kwan, Dave Passmore, Dave Dagenhart, Juan Astorga, Alberto Reis, Helio da Motta Filho, Chris Darling, and Chris Kennedy. I won't try to name all of the past E769 graduate students whose work and advice helped me along the way, but a few names stick out: Rob Jedicke, Steve Takach, Ali Rafatian. Thanks also to Lisa Chen-Tokarek, Candies Kastner, and Marcia Streetman for the help they provided.

During my time at Yale, I received more help than I can recall from many people in the department. Thanks to you all, and most especially to Jean Belfonti, Brenda Kuhn, Carole DeVore, Rochelle Lauer, Elia Mikhail, Peter Martin, and Hannah Smith. I would also like to acknowledge the work of the faculty members whose

courses I attended, with whom I taught PHYS 165/166, or whose advice I sought.

My regards also go to my friends in the ranks of the physics graduate students. Good luck to those of you who are still working at it! Finally, thank you to my wife Ling-Yi for being a source of strength, support, and love during these sometimes difficult years and for bringing little Giselle into the world; she is a buoyant force of joy to both of us!

For Ling-Yi and Giselle

Contents

Acknowledgements **iii**

1 Introduction **1**

2 Theory **4**

2.1 Motivation 5

2.2 Renormalization 7

2.3 Hard-scattering processes 10

2.4 Factorization 12

2.5 Non-perturbative effects 16

2.6 Predictions and uncertainties 19

2.6.1 Absolute cross-sections 21

2.6.2 Differential cross-sections 23

3 Fermilab E769 **28**

3.1 Beams 29

3.2 Beam particle identification 30

3.3 Target 33

3.4 Charged particle analysis 34

3.4.1 Silicon microstrip detector 35

3.4.2 Drift chambers 36

3.4.3 Magnets 37

3.4.4 Čerenkov counters 38

3.5 Triggers 39

3.6 Scalers 42

4 Monte Carlo **44**

4.1 Event generation 45

4.2 Digitization 47

5 Analysis **49**

5.1 Event reconstruction 49

5.2 Cut variables 51

5.3 Pair strip 54

5.4 Substrip 55

5.5 Cut optimization 56

5.6 Final cuts 59

6 Data **61**

6.1 Event weeding 62

6.2 Data subsets 63

6.3 Data signals 64

6.3.1 Data signals vs. x_F 71

6.3.2 Data signals vs. p_T^2 73

7 Acceptance **75**

7.1 Definition and calculation 75

7.2 Monte Carlo weighting 77

7.2.1 Trigger efficiency 77

7.2.2 Čerenkov efficiency 79

7.2.3 Differential distributions 81

7.2.4 Lifetime distributions 84

7.2.5 Drift chamber efficiency 85

7.2.6 Data subset combination 86

7.3 MC signals 87

7.3.1 MC signals vs. x_F 88

7.3.2 MC signals vs. p_T^2 91

7.4 Results 91

8 Forward Cross-sections **99**

8.1 Definition and calculation 99

8.2 Systematic errors 107

8.2.1 Data signals 108

8.2.2 Acceptance 109

8.2.3 Flux 112

8.2.4 Summary 113

8.3 Results 114

8.3.1 Forward cross-sections 114

8.3.2 Beam particle dependence 120

8.3.3 Hadronization 123

8.3.4 Leading-particle asymmetries 127

9 Differential Cross-sections **129**

9.1 Definition and calculation 129

9.2 Systematic errors 132

9.3 Results 135

9.3.1 Differential cross-sections 135

9.3.2 Beam particle dependence 147

9.3.3 Hadronization 150

10 Conclusions **157**

A Glossary of Acronyms **159**

Bibliography **162**

Chapter 1

Introduction

The absolute cross-section for charm production in high-energy hadronic interactions, despite more than twenty years of experimental activity, remains an issue of considerable interest. Early cross-section measurements are characterized by orders-of-magnitude discrepancies. Results from modern experiments (i.e., capable of full mass reconstruction and/or decay vertex detection) are relatively few in number and, although agreement among them has improved, still suffer from low statistics and large systematic errors [42]. The $c\bar{c}$ cross-sections for collisions of light hadrons (π, K, p) on nuclei are an independent test of assumptions underlying perturbative QCD predictions for heavy-quark production, which for even the heavier b system are not well-established [38]. Precise knowledge of the charm cross-section will improve understanding of leptonic backgrounds relevant to B physics and heavy-particle searches. In addition, it has been proposed that enhanced production of open charm above this baseline might be used as an indicator and probe of quark-gluon plasma formation in heavy-ion collisions [27].

Perturbative QCD provides a predictive framework in which we can calculate not only the amount of $c\bar{c}$ production in a given reaction, but also the momentum distributions of the charm quarks. These predictions depend, through the dominant gluon-gluon fusion process, on the momentum distributions of the gluons in the projectile and target particles [32]. Furthermore, the shapes of these differential cross-sections are relatively insensitive to theoretical uncertainties [33]. Although non-perturbative

processes, particularly hadronization, additionally impact the x_F and p_T distributions of charm hadrons, these effects are reasonably assumed to be independent of initial-state gluon distributions. As a consequence, the shapes of these differential cross-sections should be sensitive to differences in beam-particle gluon distributions.

In this thesis, we present an analysis of Fermilab E769 data, some 400 million events collected during the 1987-88 fixed-target run. Inclusive reactions of the form

$$B\ N \rightarrow D\ X$$

are studied at a hadronic center-of-mass energy of 21.7 GeV, where the beam particle B is π^-, K^-, π^+, K^+, or p, the target is a nucleon N, and D is one of the charm mesons D^+, D^0, D_s, or D^{*+} (or a corresponding antimeson).[1] For each of these reactions, absolute and differential ($d\sigma/dx_F$ and $d\sigma/dp_T^2$) cross-sections are measured. For K and p beams, measurements of leading-particle asymmetries are also presented, addressing for the first time the effect of a leading strange quark. (A leading charm particle is defined, for $x_F > 0$, as one which shares at least one light valence quark or antiquark flavor with the beam particle.) With the exception of a few $d\sigma/dx_F$ measurements which extend to negative x_F, present results are confined to D mesons produced in the forward hemisphere (as measured in the hadronic center-of-mass frame).

Signals for these particles are obtained through full reconstruction of the following charged hadronic decay modes:

$$\begin{array}{lcll}
D^+ & \rightarrow & K^-\pi^+\pi^+, & (D^+ \rightarrow K\pi\pi) \\
D^0 & \rightarrow & K^-\pi^+, & (D^0 \rightarrow K\pi) \\
D_s^+ & \rightarrow & \left\{ \begin{array}{l} \phi\,\pi^+,\ \phi \rightarrow K^+K^- \\ \overline{K}^*(892)^0 K^+,\ \overline{K}^{*0} \rightarrow K^-\pi^+, \end{array} \right. & \begin{array}{l} (D_s \rightarrow \phi\pi) \\ (D_s \rightarrow K^*K) \end{array} \\
D^{*+} & \rightarrow & D^0\pi^+,\ D^0 \rightarrow K^-\pi^+, & (D^* \rightarrow D^0\pi)
\end{array}$$

The righthand column above contains the shorthand names used to refer to these

[1]Throughout this text, names of charm particles (decays) generically denote the particles (decays) and their charge conjugates, unless otherwise stated or in contexts in which the sign of the D meson matters (e.g., in discussions of the leading-particle effect).

decay modes; combined $D_s \to \phi\pi$ and $D_s \to K^*K$ modes are referred to as "$D_s \to KK\pi$".

The central results presented in this thesis have appeared in two papers published concurrently in *Physical Review Letters* [10, 11].

Chapter 2

Theory

In this chapter we examine Standard Model cross-section[1] predictions for the production of charm in hadronic collisions. The inclusive reaction can be written as follows:

$$H_B + H_T \rightarrow \; c\bar{c} + x' \; \rightarrow H_c + H_{\bar{c}} + X, \tag{2.1}$$

where H_B (H_T) is the beam (target[2]) hadron, H_c ($H_{\bar{c}}$) is any hadron containing a c ($\bar{c}$) valence (anti)quark, and X (x') indicates all non-charm hadrons (partons) in the final (intermediate) state. Unitarity of the hadronization process (depicted by the arrow on the right) requires that it occur with 100% probability;[3] more interesting is the hard scattering (left arrow) of H_B and H_T's constituent partons, resulting in $c\bar{c}$ pair production. Not depicted are the weak and electromagnetic processes by which the charm and other unstable hadrons decay into stable particles.

[1]See Sections 8.1 and 9.1 for the relevant definitions.

[2]Although the E769 target is comprised of various nuclei, the target hadron is considered a nucleon. Support for the independence of charm production on the nuclear environment is given in Section 8.1.

[3]The hadronization process as written above neglects the contribution of charmonium states to the total charm particle cross-section. At the center-of-mass energy achieved by E769, however, this contribution is negligible.

2.1 Motivation

Calculation of a scattering amplitude, even in the context of non-relativistic time-independent quantum mechanics, is a problem often made tractable only through the use of perturbative methods, i.e., expression of the amplitude as a power-series expansion in some small parameter (say, g). Results obtained via this procedure are necessarily approximate; their reliability (at any given order in g) is contingent upon whether and/or how rapidly the series converges. For this reason, an important consideration is the "smallness" of g, which must be sufficient to render insignificant (at some desired level of accuracy) the error associated with truncation of the series. In practice, if the magnitude of the $(n+1)$th-order term in the series cannot be well-estimated, it will be difficult to determine whether g is small enough to make an nth-order calculation useful.

For a relatively simple case, such as scattering of a non-relativistic electron by a static charge distribution, iterative procedures (e.g., the Born approximation) can be used to obtain a solution to Schrodinger's equation expressible in powers of V_{int}, the scattering potential. In treating a more complicated case, however, for example inelastic scattering in which the destruction and creation of particles are involved, we make use of the more sophisticated formalism underlying the Standard Model of particle interactions, namely quantum field theory. In this picture, each fundamental interaction is described as acting via the exchange or "mediation" of a particular (set of) vector boson(s). Feynman, in an approach directly motivated by his "many-paths" formulation of quantum mechanics, developed a prescription for grouping and calculating all paths[4] contributing to a particular physical process to a given order in the coupling strength g of the theory. Each topologically distinct path, integrated over all internal momenta, can be represented by a Feynman diagram, a simple schematic

[4]In this context, "path" indicates a particular evolution in spacetime (generally entailing particle creation, destruction, and exchange) connecting sets of specified initial and final particle states. These paths must be consistent with the conservation laws obeyed by the particular interaction(s) involved and are most usefully evaluated in momentum space, with definite 4-momenta (and possibly other quantum numbers) assigned to the initial, final, and intermediate states.

in which the number of vertices indicates the relevant order in perturbation theory.[5] For a particular process, Feynman diagrams are readily written down and connected to the corresponding integrals via a set of Feynman rules; the amplitude for the process is then given by the sum of all contributing diagrams.

A measurable quantity such as a cross-section is proportional not to an amplitude, which is in general a complex number, but rather to the product of an amplitude and its complex conjugate (i.e., the *square* of the amplitude's norm). Therefore, economy of expression dictates that the resulting perturbative expansion be expressed as a series in a parameter proportional to g^2, which is designated α. For example, the fine-structure constant α ($\sim \frac{1}{137}$) of electrodynamics is equal (in CGS units) to $\frac{e^2}{4\pi}$, where the elementary charge e plays the role of the coupling strength g. We hereafter use the term "coupling strength" to indicate α rather than g, unless otherwise specified.

In this chapter, we concern ourselves with the hadronic production of charm, a phenomenon caused by strong interactions. Although in principle this physics is sensitive at some level to electroweak effects, the extreme relative weakness of all other interactions with respect to the strong[6] allows us to neglect consideration of these corrections in the following discussion. The Feynman rules needed to generate the relevant diagrams are therefore all derivable from a Lagrangian containing two classes of terms: (1) kinetic terms governing the propagation of free quarks and (2) terms associated with the SU(3) color symmetry underlying Quantum Chromodynamics (QCD). These latter include terms corresponding to quark-gluon coupling, gluon-gluon coupling, and gluon kinetic energy.

"Canonical" perturbative QCD predictions for charm production are provided by Nason, Dawson, and Ellis (NDE), who have published full next-to-leading order (NLO) calculations (i.e., to order α_S^3) of total and differential cross-sections for the hadronic production of heavy quarks [36, 37]. The theorists Mangano, Nason, Ridolfi, and Frixione (in various permutations) have provided follow-up studies of these results

[5] For purposes of this discussion, we assume that all vertices in the contributing diagrams correspond to a single coupling strength g.

[6] Relative interaction strength depends on the distance scale at which the comparison is made, as will be discussed further in this chapter. At scales relevant to charm production, the strong coupling α_S is more than fifty times greater than the electromagnetic coupling α.

as well [32, 26, 38]. In the following sections, we discuss issues surrounding these calculations, followed by the numerical predictions themselves.

2.2 Renormalization

Evaluation of Feynman integrals is complicated by the presence of divergences, which can be classified into two types: ultraviolet and infrared. The former (latter) are associated with integrations over internal loop momenta k^μ which diverge as $k^\mu \to \infty\,(0)$.[7] Such infinities are a typical feature of quantum field theories, including QCD. The procedure known as renormalization, by which ultraviolet divergences are subtracted order-by-order in perturbation theory, rendering predictions finite, is well known. Without delving too deeply into technical details, we discuss some features of renormalization which are relevant to the interpretation of QCD predictions for charm hadroproduction.

Essentially, if a theory is renormalizable, each divergent diagram can be associated in a consistent manner with one or more of the input parameters of the theory (e.g., particle mass, field normalization, coupling strength) in such a way that these "bare" parameters absorb the infinities and yield analogous "renormalized" quantities which are finite. Removal of these infinities alone, however, does not completely determine these quantities; there remains some freedom in deciding what *finite* contributions of the divergent graphs will be absorbed into the definitions of the renormalized parameters. Specific prescriptions for eliminating this residual arbitrariness are called renormalization schemes and consist of fixing the values of renormalized parameters at particular mass scales. The coupling strength α is defined in terms of a sum of corrected vertex diagrams evaluated at a mass scale μ_R, which we call the renormalization scale.

An expression for a physical quantity, written as an expansion in α so defined, therefore includes terms which depend on μ_R, typically logarithmically. The scale at which we choose to "define the theory", however, is arbitrary; this expression,

[7] If light quarks are treated as massless, infrared divergences also include infinities resulting from collinear emission by a quark of a gluon; these are called collinear or mass divergences.

evaluated at a particular order in perturbation theory, must be *independent* of μ_R. This requirement[8] allows us to make the scale dependence of α explicit. The resulting "running" coupling constant $\alpha(\mu)$, evaluated at μ_R, can then be associated directly with each corrected vertex in a given diagram.

The expression for the dimensionless coupling $\alpha(\mu)$ must include another mass scale; for this purpose, the fundamental scale Λ_{QCD} is introduced. Although the precise definition of Λ_{QCD} depends on the particular renormalization scheme chosen, it corresponds to the mass scale at which the coupling α blows up[9] (more on this phenomenon later), as can be seen by the following leading-order expression:

$$\alpha_S(\mu) = \frac{1}{b_0 \ln(\mu/\Lambda_{QCD})}, \tag{2.2}$$

where b_0 is a constant and the subscript "S" has been added to α to indicate that the discussion is now confined to the strong coupling of QCD. Λ_{QCD} is a parameter than can be determined experimentally; it is on the order of a few hundred MeV.[10] We can also express α_S in the alternative form

$$\begin{aligned} \alpha_S(\mu) &= \frac{\alpha_S(\mu_R)}{1 + b_0\, \alpha_S(\mu_R) \ln(\mu^2/\mu_R^2)} \\ &= \alpha_S(\mu_R) - b_0\, \alpha_S^2(\mu_R) \ln(\mu^2/\mu_R^2) + \ldots, \end{aligned} \tag{2.3}$$

which is more useful in evaluating the behavior of α_S in the neighborhood of our chosen "subtraction point" μ_R.

[8]The derivation of the renormalization group equation follows an equivalent line of argument.

[9]Actually, this characterization of Λ_{QCD} is misleading for two reasons. First, as α_S grows close to and beyond unity, the expression for its scale dependence, obtained from some finite order calculation in perturbation theory, becomes meaningless. Second, the scale dependence of α_S is impacted by threshold effects; as μ increases into a regime where heavy quarks of a new flavor contribute significantly to loop corrections, the values of b_0 and Λ_{QCD} change. This effective Λ_{QCD} is specified by replacing the generic subscript with the number of "active" flavors appropriate to a given physics process. For charm production, therefore, Λ_3 is the most relevant incarnation of the fundamental QCD scale.

[10]Taking Λ_{QCD} to represent the mass scale of QCD, we obtain a corresponding distance scale on the order of a fermi and time scale on the order of 10^{-21} seconds.

Up to this point, no physical interpretation has been given to the scale dependence of α_S. After all, the scale μ_R at which we choose to evaluate α_S is arbitrary; to a given order in perturbation theory, calculated predictions of measurable quantities are insensitive to our choice. In order that perturbation theory be useful, however, a value of μ_R must be chosen such that *both* the expansion parameter $\alpha_S(\mu_R)$ and the logarithmic dependencies on μ_R are small. Loosely speaking, this condition holds when μ_R is on the order of the mass scale relevant to the physical process in question.[11] It is therefore common to speak of $\alpha_S(\mu)$ as the *effective* strong coupling at the *physical* mass scale μ.

The scale dependence of α_S described above has one feature that distinguishes the strong interaction from the other forces of nature in a profound way: the effective coupling *decreases* monotonically as the mass (distance) scale increases (decreases). This behavior, known as *asymptotic freedom*, can be attributed to the presence of gluon-gluon coupling, or in other words to the fact that the vector bosons mediating the strong interaction are themselves carriers of color charge. Asymptotic freedom has the consequence that the properties of hadronic bound states cannot be treated perturbatively. On the basis of non-perturbative results,[12] however, it is widely believed that asymptotic freedom provides an explanation for the phenomenon of color confinement, i.e., the observation that all particles which are stable (with respect to the time scale of the strong interaction) are color-neutral. To zeroth order, this limits the possible hadronic states to baryons, mesons, and glueballs. For strong hard-scattering processes, however, perturbative QCD calculations become more reliable as the mass scale (e.g., Q^2) grows.

In their calculations of charm absolute (differential) cross-sections, NDE choose μ_R to be equal to m_c ($2\sqrt{m_c^2 + k_T^2}$); a central value of 1.5 GeV is assigned to m_c. (Mangano, Nason, and Ridolfi (MNR) modify this choice in calculating differential

[11]In general, a particular process is characterized by more than one mass scale. In the case of charm production, both the charm quark mass m_c and the 4-momentum transfer Q^2 define physical mass scales which are not necessarily similar in magnitude. Furthermore, if we are interested in the differential cross-section for charm quark production, the transverse momentum k_T of the charm quark also introduces a scale.

[12]For example, lattice QCD calculations.

cross-sections, in which case they let μ_R equal $\sqrt{m_c^2 + k_T^2}$.) At this scale, α_S is approximately $\frac{1}{3}$, too large to dismiss the possibility that higher-order terms comprise significant corrections to NLO results.

Although the NLO cross-section is independent of μ_R to order α_S^3, residual dependence of order α_S^4 remains.[13] NDE use the sensitivity of their results to factor-of-two variation of μ_R as an ansatz estimate of the error associated with truncation of the perturbative series at NLO. The justification for this estimate is that since the full calculation to order α_S^4 (NNLO) must be independent of μ_R, uncalculated NNLO terms must cancel the observed variation and are therefore similar in magnitude. But the cancellation terms thus gauged do not depend on the tree-level NNLO contributions (e.g., two gluon radiation) and indeed do not even include all of the NNLO μ_R-dependence (e.g., that arising from two-loop renormalization of leading-order (LO) tree-level diagrams). The upper limit allowed by this uncertainty actually corresponds to adding to the NLO result a NNLO contribution estimated to be equal to the NLO contribution but enhanced through multiplication by an artificially large factor (instead of the "small" $\alpha_S(m_c)$). Despite these caveats, cross-section uncertainties associated with variation of μ_R is quantified along with other theoretical uncertainties in Sections 2.6.1 and 2.6.2.

2.3 Hard-scattering processes

The relevant distance scale for charm production in hadronic collisions is at most a small fraction of a fermi, indicating that the underlying processes must be described as interactions between the constituent partons of the colliding hadrons. LO diagrams are of order α_S^2.[14] At LO, two processes contribute, namely gluon-gluon fusion and quark-antiquark annihilation; the relevant diagrams are shown in Fig. 2.1.

As mentioned previously, NDE have published full NLO calculations of total and

[13]This higher-order μ_R dependence arises in using the renormalized $\alpha_S(\mu_R)$ in evaluating NLO tree-level diagrams.

[14]Actually, the *square* of the amplitudes represented by the LO diagrams are proportional to α_S^2. We will stick to the usage in the text, however, in which we equate a diagram with a physical process, which we in turn equate with that process' effect on the charm cross-section.

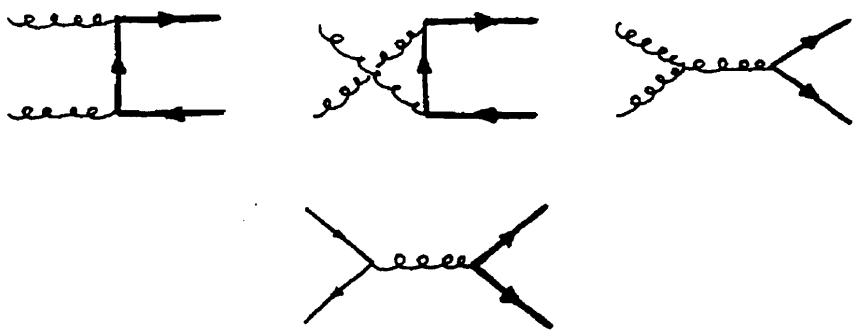

Figure 2.1: LO diagrams. Light (heavy) lines indicate light (charm) quarks.

differential cross-sections for the hadronic production of heavy quarks. At this order (α_S^3), gg fusion and $q\bar{q}$ annihilation continue to be the most important processes; the extra vertices in these NLO diagrams are due to gluon radiation. Appearing for the first time at NLO is quark-gluon fusion, the net effect of which is only a minor (negative) adjustment to the total cross-section. Also contributing are diagrams formally of order α_S^4; interference between these "virtual" diagrams and corresponding LO processes lead to NLO terms. A sampling of some NLO diagrams is shown in Fig. 2.2. At NLO, the first loop corrections to the vertices and particle propagators appear. As discussed in the previous section, the infinities associated with these Feynman integrals are absorbed into the renormalized, scale-dependent coupling $\alpha_S(\mu)$. Although these loops are not explicitly shown in any of the pictured diagrams, the vertices are understood to include them.

Let a generic parton-parton interaction resulting in $c\bar{c}$ production be represented by Fig. 2.3. The momenta of the partons from the beam and target hadrons are $\vec{q}_B$ and $\vec{q}_T$, respectively. Expressions for charm production cross-sections are simplest in the partonic center-of-mass frame, in which $q_B = q_T \equiv q$. Treating the partons as massless, we obtain a partonic center-of-mass energy $\sqrt{s}$ of $2q$. Note that in this frame, s is equal as well to the 4-momentum transfer Q^2. The threshold energy for production of a $c\bar{c}$ pair is $2m_c$; it is convenient to work with the dimensionless parameter $\rho \equiv 4m_c^2/s$, which has a value of 1 at threshold and decreases with increasing s. The

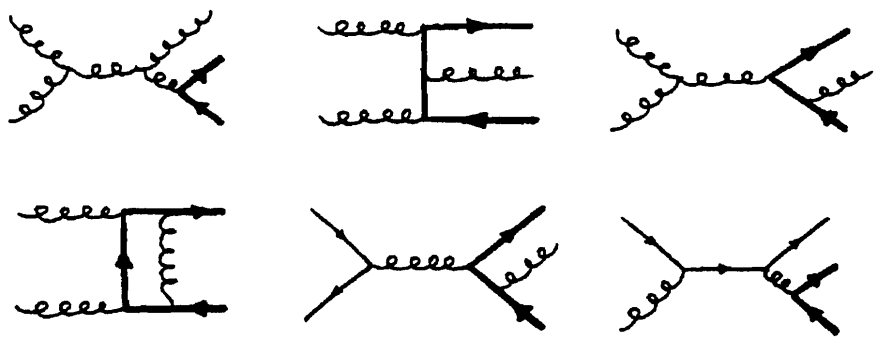

Figure 2.2: NLO diagrams. See Fig. 2.1 caption.

shaded oval in Fig. 2.3 represents the superposition of all diagrams contributing to a given order in perturbation theory. The observed charm quark (or antiquark) has a momentum $\vec{k}$; the unobserved charm (and possibly a radiated gluon) account for the rest of the final state (labelled x).

Total $c\bar{c}$ production cross-sections (integrated over all $\vec{k}$) depend only on ρ and m_c; single-particle inclusive differential cross-sections, on the other hand, depend additionally on the magnitude of $\vec{k}$ and its angle with respect to the axis formed by the colliding partons.

In their differential cross-section paper, NDE point out the presence of logarithmic terms which become large when $k_T \gg m_c$. In this limit, the heavy quark becomes effectively light, leading to final-state infrared divergences associated with gluon emission. In the kinematic range accessible to E769, however, charm quark k_T never greatly exceeds m_c.

2.4 Factorization

The hard-scattering amplitudes discussed in the previous section are alone not sufficient to obtain cross-section predictions for two reasons. First, in the laboratory, it is hadrons (e.g., π, K, p) that are accelerated into one another, not partons. Second, there is an additional class of NLO diagrams which must be accounted for in the

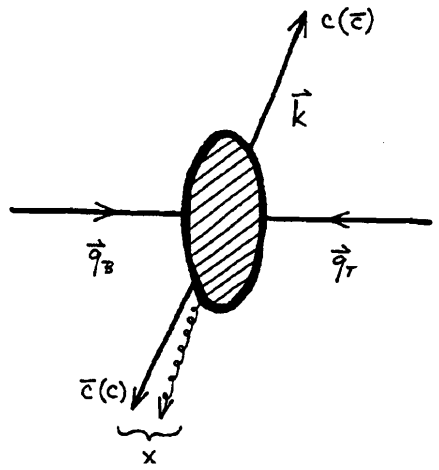

Figure 2.3: Schematic of hard-scattering kinematics.

full cross-section calculation: namely, diagrams in which one of the incoming partons radiates a gluon *before* the primary interaction occurs. These diagrams are infrared divergent, and must be regularized before a sensible result can be obtained.

Through a procedure known as factorization, both of these obstacles are removed. The hard-scattering amplitudes take as their "inputs" only the identity and momenta[15] of the initial state partons. Therefore, if, for each colliding hadron, the momentum distributions of each type of constituent parton are known, then the total $c\bar{c}$ cross-section can be written as a convolution of these parton distribution functions (PDFs) with the hard-scattering cross-sections obtained by direct evaluation of the Feynman integrals.

In a procedure analogous to renormalization, infrared divergences associated with soft gluon emission are absorbed into the definition of the PDFs, rendering the aforementioned convolution products finite. As with renormalization, this subtraction of infinities must be done at some mass scale, which we label the factorization scale μ_F. Logarithmic dependencies on μ_F are introduced into the PDFs, leading to concomitant uncertainties in the cross-section predictions.

[15]Other quantum numbers are averaged over.

In this formalism, all partons within a given hadron are treated as parallel streams, the sum of whose longitudinal momenta is simply the hadron momentum $\vec{p}_B$ or $\vec{p}_T$; transverse components of the parton momenta are treated as zero.[16] PDFs are therefore given as functions of x, the *fraction* of the hadron's momentum carried by the parton. More than one of each type of parton can be present in a given hadron; PDFs are therefore actually number densities, proportional at a given x value to the probability of finding a parton of momentum fraction x, where some scattering process provides the means of "finding". Measurement of the PDFs therefore entails measuring scattering cross-sections, characterized by a certain 4-momentum transfer $Q^2 = \mu_F^2$, and unfolding from the aforementioned convolution the formulae relevant to the scattering involved.

The crux of the factorization theorem is that the PDFs so obtained are *independent* of the process used to measure them. This allows us to test, for example, QCD predictions for charm production using PDFs obtained by a number of various means: deep inelastic scattering of leptons (charged or neutral) on hadrons or production in hadron-hadron collisions of prompt photons or Drell-Yan pairs. In practice, PDFs obtained by simultaneous fits to data from some or all of the above processes are used [28].

This independence of PDFs on the "fate" of the extracted parton means that their Q^2-dependence is purely a QCD phenomenon, in particular a consequence of the scale dependence of α_S. To illustrate this, consider the probability of extracting from a proton a d quark with momentum fraction x. In addition to the contribution of the valence d, we must account for the $d\bar{d}$ pairs produced by constituent gluons. Any gluon with momentum fraction $x' > x$ is a potential additional source of the desired d. Therefore, beginning at the one-loop level, the coupling strength α_S directly impacts PDF evolution.

Equation 2.4 gives the single-quark charm differential cross-section; the total $c\bar{c}$ cross-section is obtained by integrating the charm momentum $\vec{k}$ over the full solid angle as well as the range in magnitude allowed by the kinematics.

[16]See Section 2.5 for a discussion of the consequences of relaxing this assumption.

$$\frac{d^3\sigma}{d^3k} = \sum_{i,j} \int dx_B dx_T \left[\frac{d^3\hat{\sigma}_{ij}(x_B p_B, x_T p_{target}, \vec{k}, m_c, \mu_R, \mu_F)}{d^3k} \right] F_i^B(x_B, \mu_F) F_j^T(x_T, \mu_F) \tag{2.4}$$

In this equation, $\hat{\sigma}_{ij}$ is the hard-scattering cross-section for partons i and j (from which infrared singularities have been subtracted) and $F_i^{B(T)}$ is the beam (target) hadron PDF for constituent parton i. The summation runs over each two-parton combination contributing to charm production; the integrals are over the momentum fractions of each parton. The momentum of the beam (target) parton is $x_B p_B$ ($x_T p_{target}$), where p_B (p_{target}) is the momentum of the beam (target) hadron. Note that if the partons are treated as massless, the hadronic and partonic center-of-mass energies ($\sqrt{S}$ and $\sqrt{s}$, respectively) are related by

$$s = x_B \, x_T \, S. \tag{2.5}$$

The differential cross-section as written in Eq. 2.4 is not Lorentz invariant; all quantities are understood to be evaluated in the hadronic center-of-mass frame. The longitudinal momentum in this frame is converted to the dimensionless Feynman-x variable (x_F) by dividing it by $\sqrt{S}/2$, half the available energy, leading to the range $-1 \leq x_F \leq 1$.

Use of this factorized formula assumes that certain non-perturbative contributions to charm production, some of which will be discussed in the following section, are small with respect to production involving one parton from each hadron. Collins, Soper, and Sterman examined the effect of these competing processes in heavy-quark production; their conclusion was that these contributions are suppressed by powers of the ratio m/M, where m is a typical hadronic mass scale and M is the mass of the produced heavy quark [22]. Depending on how we interpret m, the charm quark mass ($m_c \simeq 1.5$ GeV) can lead to suppression factors not particularly far from unity; it therefore remains an open question whether m_c is large enough to justify use of the factorization formalism.

2.5 Non-perturbative effects

As mentioned previously, a charm quark, once produced, must hadronize to *something.* As long as the time scale over which this process occurs is much longer than the strong interaction time scale characterizing the production process itself, the total $c\bar{c}$ cross-section calculated ignoring the subsequent histories of the charm quarks should be valid, i.e., equal to one half the total charm plus anticharm particle cross-section. Interactions between a charm quark and other quarks in the event, however, will have a measurable impact on the momentum distribution of the corresponding charm hadron, leading to differences in the predicted differential cross-sections of charm quarks and, for example, charm mesons. In this section, we give only a qualitative discussion of these effects, which in general involve the exchange of soft gluons and therefore cannot be treated by perturbative methods. In addition, we mention some potential corrections to the factorized perturbative formula motivated in the previous section.

We begin with initial-state effects, some of which in principle can lead to additional mechanisms for charm production beyond those accounted for in the perturbative calculation. The first of these is flavor excitation. In this process, a $c\bar{c}$ pair intrinsic to one of the initial-state hadrons (i.e., "sea" as opposed to valence quarks) is excited by interactions with the other hadron (via gluon exchange), giving the virtual heavy quark pair enough energy to reach its mass shell. The results of an early theoretical study by Combridge suggested that the charm cross-section attributable to flavor excitation alone was potentially greater than that from LO "flavor creation" processes [23]. Subsequent investigations showed, however, that this process, whose diagram is topologically equivalent to standard gg fusion graphs, is thereby included at some level in the perturbative result [22]. NDE therefore calculate $c\bar{c}$ cross-sections using PDFs with no explicit charm sea component, including flavor excitation as a higher-order correction (i.e., as a component of gg fusion). More recently, Tung and collaborators have developed a method of fully incorporating both flavor creation and excitation by explicitly subtracting from the sum of the two processes the region of kinematic overlap. The net addition due to flavor excitation is found to grow large only for

production well above threshold (i.e., $k_T \gg m_c$);[17] we therefore do not expect the E769 results to be sensitive to this effect.

Related to the flavor excitation process is the concept of intrinsic charm, introduced by Brodsky and collaborators [21]. In this picture, hadronic wavefunctions contain Fock state components in which a $c\bar{c}$ pair carries most of the hadronic momenta. For example, a proton $|uud>$ would contain a $|uudc\bar{c}>$ component. Note that these charm components are *not* equivalent to the virtual charm sea generated by QCD evolution of the PDFs. Originally motivated by CERN-ISR measurements of anomalously high charm particle cross-sections at high x_F,[18] the intrinsic charm component of the proton was estimated to be on the order of 1-2%. Recent (null) measurements of diffractive charm production in 800 GeV p-Si interactions, however, have been interpreted as imposing an upper limit of 0.2% on the intrinsic charm component of the proton [31].

The longitudinal (x_F) and transverse (p_T) momentum distributions of charm particles should in principle differ from those predicted for charm quarks, due to the interaction of the latter with other quarks in the event, both spectator valence quarks and light $q\bar{q}$ pairs created from the vacuum. The process by which charm quarks coalesce with light quarks to form color-neutral bound states is known as hadronization or fragmentation. Even before this stage is reached, however, the factorized formula developed above may neglect an important input to predicting the charm *quark* distributions, namely the intrinsic p_T of constituent partons. On the basis of the transverse spatial confinement of the partons, we might expect transverse momenta on the order of Λ_{QCD} – a few hundred MeV. MNR, in a study based on a HERWIG Monte Carlo simulation, find that a LO calculation assuming an average intrinsic p_T of 1.5-1.7 GeV is sufficient to reproduce MC results for charm quark distributions (which they admit should not be taken as a universal benchmark) [32]. The effect of this intrinsic p_T is a "uniform smearing" of the transverse distributions; for a cross-section exponentially

[17]Actually, this method was first developed to describe heavy quark *lepto*production [5]. An analogous treatment of hadroproduction is in progress; preliminary results were presented at DPF96 [39].

[18]For an extensive review of early charm hadroproduction measurements, see the two review articles given in [42].

falling with p_T, the net effect of such smearing is a hardening of the distribution.

In treating the effect of hadronization on charm distributions, the assumption of universal fragmentation is sometimes made. In this picture, the ratio of the charm hadron momentum to that of its "parent" charm quark is given by a probability distribution (the fragmentation function) which is independent of the process by which the charm quark is produced, for example through e^+e^- collisions. The charm quark is essentially seen as the progenitor of an isolated jet; its momentum is degraded by the energy lost in the creation of light $q\bar{q}$ pairs. In hadronic collisions, however, the environment is sufficiently different to call this procedure into question.[19] For example, coupling between low-k_T charm quarks and co-moving spectator quarks can lead to charm hadrons whose momenta are enhanced with respect to that of their charm parents; this effect is known as "color-dragging" and is related to another consequence of charm-spectator coalescence, namely the "leading-particle" effect.

A leading charm particle is defined, for $x_F > 0$, as one which shares at least one light valence quark or antiquark flavor with the beam particle. An example of a leading particle in π^--induced production is D^-. At high x_F especially, we expect the proximity of the charm quark to the forward spray of beam fragments to lead to an enhanced cross-section for charm species which result from hadronization with these co-moving spectators. This effect has been measured to be significant and to increase at high x_F.[20] In this thesis we will make a distinction between non-leading and neutral-leading particles. A non-leading particle is defined as the charge conjugate of a leading particle (e.g., π^--induced D^+ mesons).[21] A neutral-leading particle, on the other hand, is defined as any particle for which both particle *and* antiparticle are *not* leading (e.g., K^+-induced D^0 mesons). For species which are otherwise similar, a leading particle will be more likely to have undergone color-dragging than non-leading or neutral-leading particles; therefore, we expect leading particles to exhibit harder

[19]MNR have also pointed out that application of fragmentation functions to longitudinal distributions is not boost-invariant and can lead to significantly different results in different frames [32].

[20]See Section 8.3.4 and references quoted therein.

[21]In the case of a *neutral* beam particle, this definition must be modified, as both particle and antiparticle can be leading (e.g., π^0-induced D^+ and D^- mesons). We state this only for completeness, as E769 uses only charged beams.

x_F distributions.

2.6 Predictions and uncertainties

MNR have made available the program HVQMNR, which they used to generate the NLO QCD heavy-quark cross-section predictions (absolute and differential) presented in [32].[22] This program allows for variation of beam energy (E_B), the identities of the initial-state hadrons (constrained by the availability of the appropriate PDFs), Λ_{QCD}, μ_R, μ_F, and the mass of the produced heavy quark. In this section we employ this program, using the default parameters listed below (those of MNR), to obtain predictions with which to compare our measured forward and differential cross-sections.[23]

$$
\begin{aligned}
&E_B = 250 \text{ GeV} \\
&\text{beam particle (PDF)} = \pi^- \text{ (SMRS2)}, p \text{ (HMRSB)} \\
&\text{target particle (PDF)} = N \text{ (HMRSB)} \\
&\mu_R = \mu_0 \\
&\mu_F = 2\mu_0 \\
&\mu_0 = \begin{cases} m_c & \text{absolute} \\ \sqrt{m_c^2 + k_T^2} & \text{differential} \end{cases} \\
&m_c = 1.5 \text{ GeV} \\
&\Lambda_5{}^a = 122 \text{ MeV}
\end{aligned}
$$

[a] Λ_5 is connected to the more relevant Λ_3 through the NDE renormalization scheme.

PDFs are available for the pion and proton, but not for the kaon; predictions are therefore made only for charm production induced by π^- and p.[24] MNR use SMRS2 (HMRSB) parametrizations of π^- (p) PDFs; these PDF sets are defined and discussed in [28] and are plotted in Fig. 2.4 at $Q^2 = 4$ GeV^2.

[22] The NLO QCD results published by MNR differ from those of NDE due to the former's use of more modern PDFs.

[23] We verified our correct use of HVQMNR by reproducing numerical results for absolute and differential cross-sections presented by MNR in [32] and in their follow-up paper [26], for which they were joined by Frixione (FMNR).

[24] Although π^+ PDFs should be completely determined by those for π^-, HVQMNR as written does not differentiate between the two; therefore, only predictions for π^--induced production are

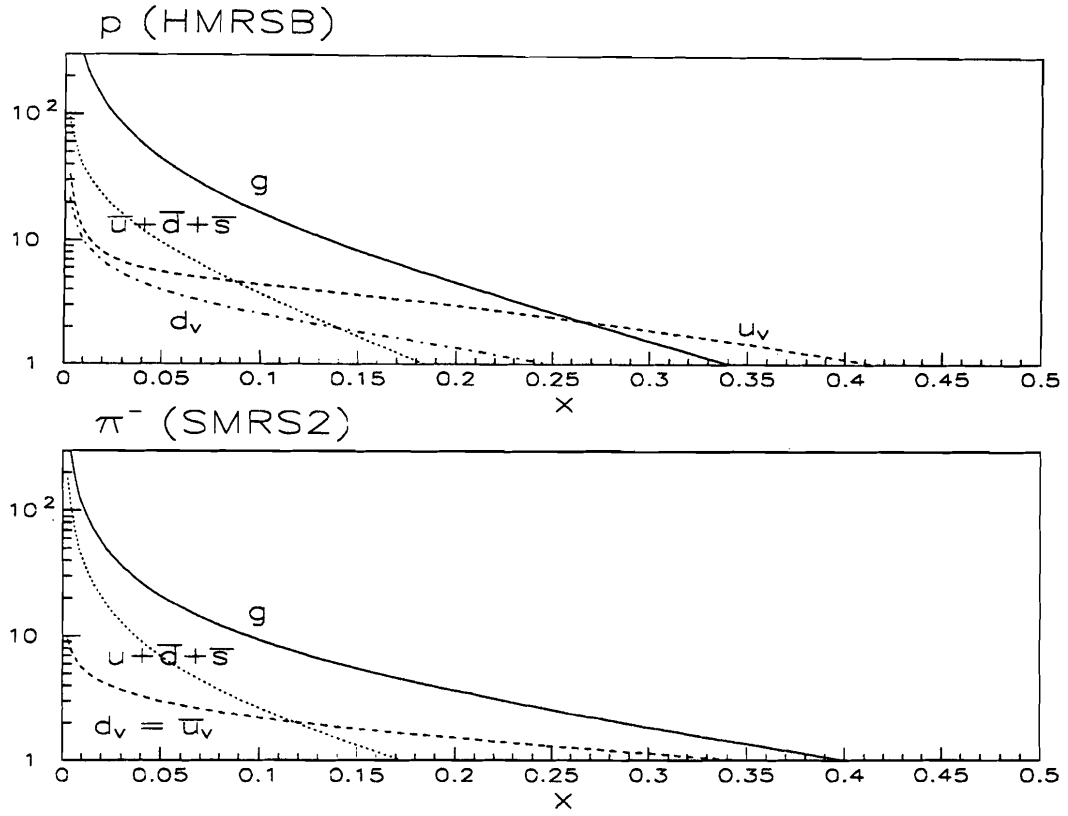

Figure 2.4: Parton distribution functions at $Q^2 = 4$ GeV^2.

Precise comparison of the contributions different processes make to charm production is not possible until the hard-scattering cross-sections are convolved with the appropriate PDFs. Assuming for the moment that amplitudes for all processes are equal and independent of ρ (in the production region $\rho < 1$), we can estimate the relative importance of gg fusion and $q\bar{q}$ annihilation by direct inspection of Fig. 2.4. For E769, $\sqrt{S} = 21.7$ GeV, leading to the relation

$$x_B x_T \geq \frac{4m_c^2}{S} = \left(\frac{2 \times 1.5\,\mathrm{GeV}}{21.7\,\mathrm{GeV}}\right)^2 = 0.019 < \rho. \tag{2.6}$$

A general feature of PDFs is that they fall very rapidly with rising x; therefore,

available.

given our aforementioned assumption, charm production should be dominated by those regions in the x_B-x_T plane close to the hyperbola defined by $x_B x_T = 0.019$. If we further assume that in this neighborhood the PDFs are falling exponentially, we find that most production occurs at the point on the hyperbola where $x_B = x_T = \sqrt{0.019} = 0.14$. Comparing $g(x)$ and $\overline{q}(x)$ distributions at $x_B = 0.14$, we expect gg fusion to dominate over $q\overline{q}$ annihilation, especially in pN collisions, where the only source of antiquarks is the sea.

This conclusion is borne out by the complete HVQMNR calculation, which indicates that gg fusion constitutes 80% (89%) of charm production in $\pi^- N$ (pN) collisions at E769's center-of-mass frame energy.[25] The balance of the cross-section is attributable to $q\overline{q}$ annihilation, qg processes providing at NLO only an insignificant correction. The *shapes* predicted for charm quark differential distributions are not affected greatly by the inclusion of NLO terms in the perturbative calculation [32]. In an absolute sense, however, the NLO contribution is very important, approximately *doubling* the $c\overline{c}$ cross-section prediction.

In Sections 2.6.1 and 2.6.2, we present NLO QCD predictions for absolute $c\overline{c}$ and differential c quark production cross-sections, respectively; these predictions are given for $\pi^- N$ and pN interactions. In addition, the uncertainties in these results will be discussed and estimated, based on MNR and FMNR results. Direct comparisons of these predictions with E769 and previous measurements will be made in Sections 8.3.1 and 9.3.1.

2.6.1 Absolute cross-sections

The predicted $c\overline{c}$ cross-sections for 250 GeV π^- and p collisions on a nucleonic target are similar: 5.2 and 4.5 μb/nucleon, respectively.[26] For pN production, we could

[25] In the remainder of this chapter, statements concerning NLO QCD predictions for charm production should be understood as applying at E769's energy, i.e., $\sqrt{S} = 21.7$ GeV.

[26] The dominant gg fusion component of the cross-section depends rather simply on the distribution of gluons in the beam particle:

$$\sigma_{gg} \propto < xg >_{thr} - x_{thr} < g >_{thr},$$

where $< g >_{thr}$ and $< xg >_{thr}$ are the first two moments of the gluon distribution above an effective charm threshold $x_{thr} \sim 0.04$. The cross-section essentially increases linearly with the fraction of

compare this number directly to the measured total charm plus anticharm *particle* cross-section in the forward hemisphere, if this latter result were available.[27] In the case of π^--induced production, however, the relative hardness of the gluons in the pion leads to asymmetric production in the hadronic center-of-mass frame, resulting in more charm particles with $x_F > 0$. MNR have determined the ratio $\frac{\sigma_{c\bar{c}}(x_F>0)}{\sigma_{c\bar{c}}}$ to be about 5/8 over a wide range in E_B, where $\sigma_{c\bar{c}}(x_F > 0)$ is defined as the $c\bar{c}$ pair production cross-section with a cut of $x_F > 0$ placed on the charm quark. In this case, therefore, we must multiply the QCD prediction by a factor $\frac{5}{8} \times 2 = 1.25$ before an analogous comparison can be made.[28]

As detailed in the previous sections, potentially significant theoretical uncertainties in $\sigma_{c\bar{c}}$ are associated with each of the important input parameters of the calculation: m_c, μ_R, μ_F, Λ_{QCD} (through which we obtain the uncertainty in α_S), and the PDFs. We report here on those which are likely to be most significant.

MNR find that decreasing m_c by 100 MeV leads to a 50% increase in the prediction for $\sigma_{c\bar{c}}$. If we assume an uncertainty of ± 300 MeV in m_c about the central value of 1.5 GeV, we find that the resulting error band in the prediction spans a full order of magnitude! Decreasing μ_R also leads to an increased cross-section prediction; multiplying (dividing) the default value of μ_R (in this case, m_c) by a factor of two decreases (increases) $\sigma_{c\bar{c}}$ to about 40% (200%) of its central value. Due to difficulties associated with varying μ_F below scales for which PDF parametrizations are available, MNR do not attempt to quantify the analogous uncertainty associated with this scale; they do note, however, that it could be as large as that for μ_R. Clearly, the errors already cited show that the precision of current theoretical predictions for $\sigma_{c\bar{c}}$ (even assuming the validity of factorized perturbative QCD formulae at NLO) lag far behind that achieved experimentally (on the order of 10-20%, in some cases).

---

momentum carried by the gluons above this threshold, adjusted by a small negative correction which increases with the number of gluons among which this momentum must be divided.

[27] In practice, we obtain cross-section measurements only for a portion (albeit the expected bulk) of the charm hadrons; in Section 8.3.1, the issues surrounding this comparison of data and theory are discussed.

[28] This factor would be slightly more complicated if the signs of x_F for the produced c and $\bar{c}$ quarks exhibited dependence on one another; MNR find that they are approximately uncorrelated.

2.6.2 Differential cross-sections

In this section, we present NLO QCD differential cross-section predictions for charm *quarks*. The HVQMNR program is used to obtain shape predictions and to study their sensitivity to variations of theoretical parameters over ranges deemed reasonable by MNR. No attempt is made to model or calculate the various non-perturbative effects described in Section 2.5; as stated previously, however, their impact on charm *particle* distributions is potentially significant. With this said, we drop the notational distinction between charm quark k_T and charm particle p_T; the symbol "p_T" is hereafter used to represent transverse momentum in both cases.

The predicted $d\sigma/dx_F$ and $d\sigma/dp_T^2$ shapes, for both $\pi^- N$ and pN interactions, are plotted in Figs. 2.5 and 2.6. Empirical fits to these distributions, described below, are also shown.

The $d\sigma/dx_F$ shapes are well-fit by the following function in the experimentally-accessible range $-0.1 < x_F < 0.8$:

$$d\sigma/dx_F = \begin{cases} N' \exp -\frac{1}{2}(\frac{x_F - x_c}{\sigma})^2, & |x_F - x_c| < x_b \\ N\,(1 - |x_F - x_c|)^n, & |x_F - x_c| > x_b. \end{cases} \tag{2.7}$$

At the boundaries between the central and tail regions ($x_c \pm x_b$), the function and its derivative are forced to be continuous through the following constraints:

$$\sigma = \sqrt{\frac{x_b(1 - x_b)}{n}} \tag{2.8}$$

$$\ln \frac{N'}{N} = n\,(\frac{x_b}{2(1 - x_b)} + \ln(1 - x_b)). \tag{2.9}$$

Thus the shape of $d\sigma/dx_F$ can be described over this range with three free parameters: x_c, x_b, and n. As detailed in Section 9.3.1, our measured x_F distribution shapes, given the precision with which they are determined, require only a 1-parameter function (Equation 9.9) be used for fitting. In comparing theory and data, therefore, we will follow the procedure of fitting data distributions to theoretical shapes directly rather than comparing parameters. For the sake of completeness, the theoretical fit parameters are given in Table 2.1. As expected from the relative average hardness of

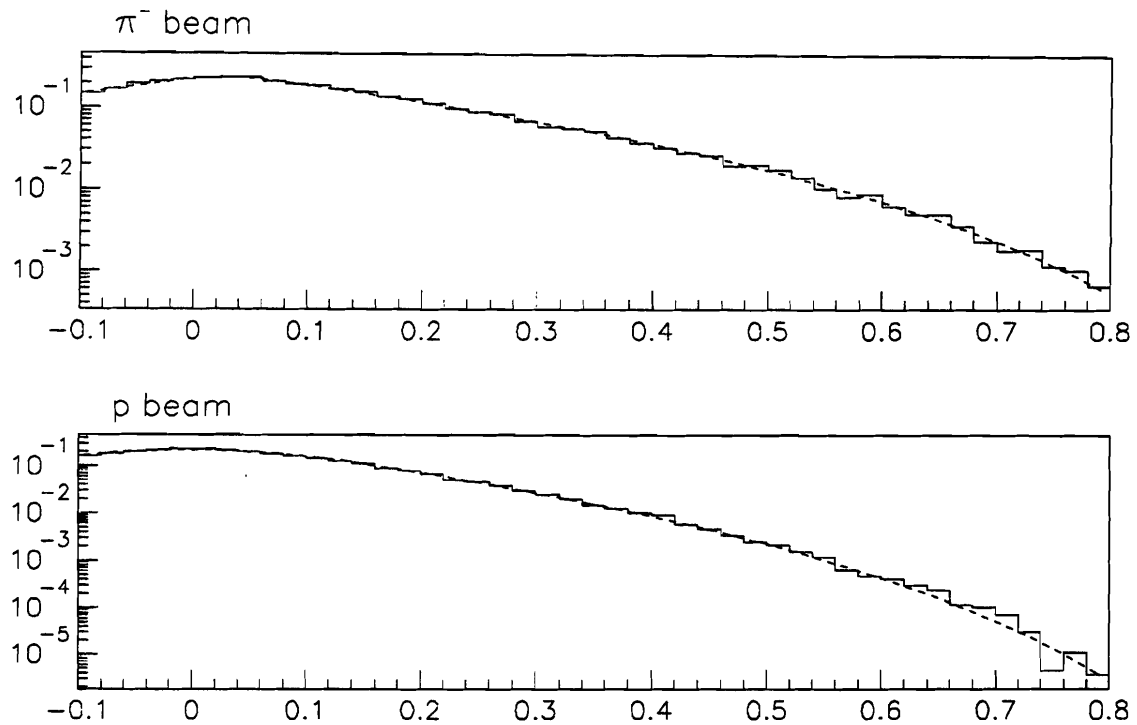

Figure 2.5: QCD NLO c quark $d\sigma/dx_F$ vs. x_F. The distributions are integrated over the full p_T range. Normalization is arbitrary.

the gluons in pions with respect to those in protons,[29] the predicted $d\sigma/dx_F$ distribution in $\pi^- N$ production falls less rapidly with x_F (i.e., has a lower n value) and is centered in the forward hemisphere (i.e., $x_c > 0$).

The theoretical predictions for $d\sigma/dp_T^2$ are well-parametrized over the entire p_T^2 range by the following function, introduced by FMNR:

$$d\sigma/dp_T^2 = N\ (\alpha\, m_c^2 + p_T^2)^{-\beta}, \tag{2.10}$$

where m_c is the mass of the charm quark. Results of these fits (with m_c set to 1.5

[29]On average, gluons carry a larger fraction of momentum in the proton (47%) than in the pion (~38%). But since the average number of gluons in the proton (19) is more than twice that in the pion (9), the average momentum *per gluon* is significantly higher in the pion.

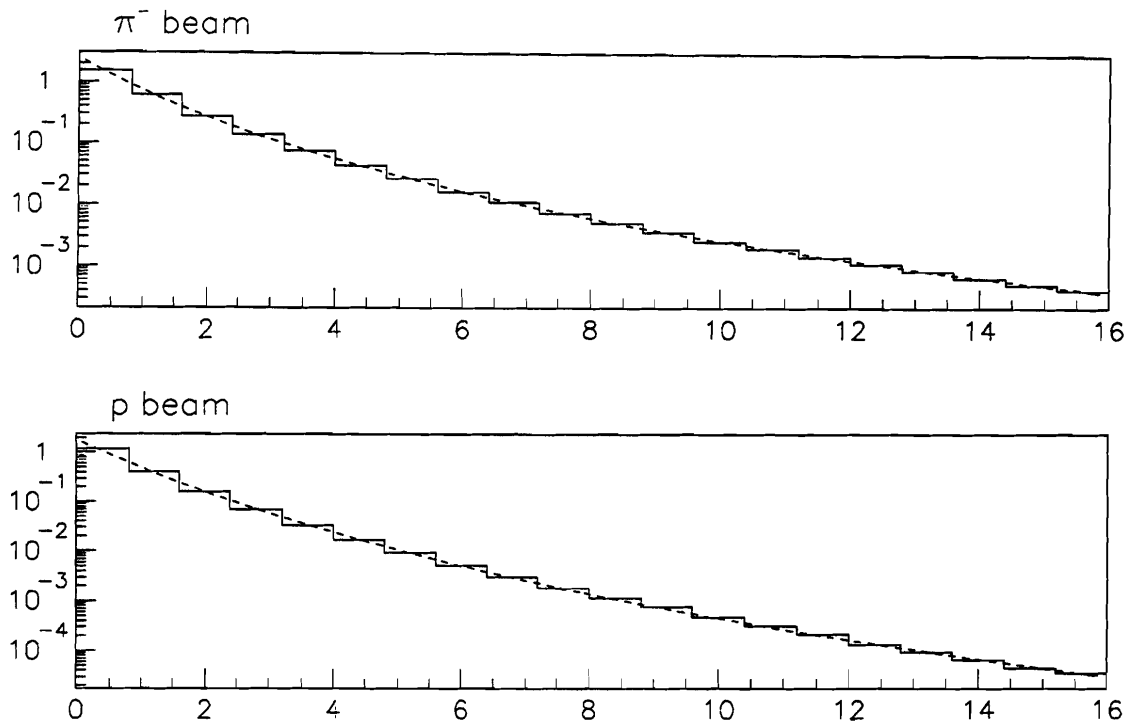

Figure 2.6: QCD NLO c quark $d\sigma/dp_T^2$ (GeV^{-2}) vs. p_T^2 (GeV^2). The distributions are integrated over the forward hemisphere ($x_F > 0$). Normalization is arbitrary.

GeV) are given in Table 2.2. Although the predicted fall-off in p_T^2 is more rapid in p-induced production, the beam-particle dependence here is less pronounced than in the x_F distributions (and therefore more easily compromised by non-perturbative effects).

In Figs. 2.7 and 2.8, changes in the predicted π-induced distributions due to variation of some of the theoretical input parameters are shown; p-induced distributions are also given as a reference by which to judge these theoretical uncertainties. The different π^- PDFs referred to in the caption of Fig. 2.8 correspond to varying the fraction of pion momentum carried by gluons by $\pm 5\%$ from the default amount used in SMRS2.

In general, the sensitivity of the shapes to these variations is small compared to

Beam	x_c	x_b	n
π^-	0.028	0.040	4.19
p	0.000	0.145	7.39

Table 2.1: $d\sigma/dx_F$ theory shape parameters.

Beam	α	β
π^-	1.76	5.45
p	2.66	8.46

Table 2.2: $d\sigma/dp_T^2$ theory shape parameters.

the difference in the shapes expected in πN and pN production. The only exception is the effect of variation of m_c (by $\pm$ 300 MeV) on the $d\sigma/dp_T^2$ distributions; the π and p beam predictions tend to change similarly with these variations, however, leaving the difference in their shape parameters fairly stable. On the right-hand side of Fig. 2.8, the effects of m_c variations on π and p-induced p_T^2 distribution shapes are shown simultaneously.

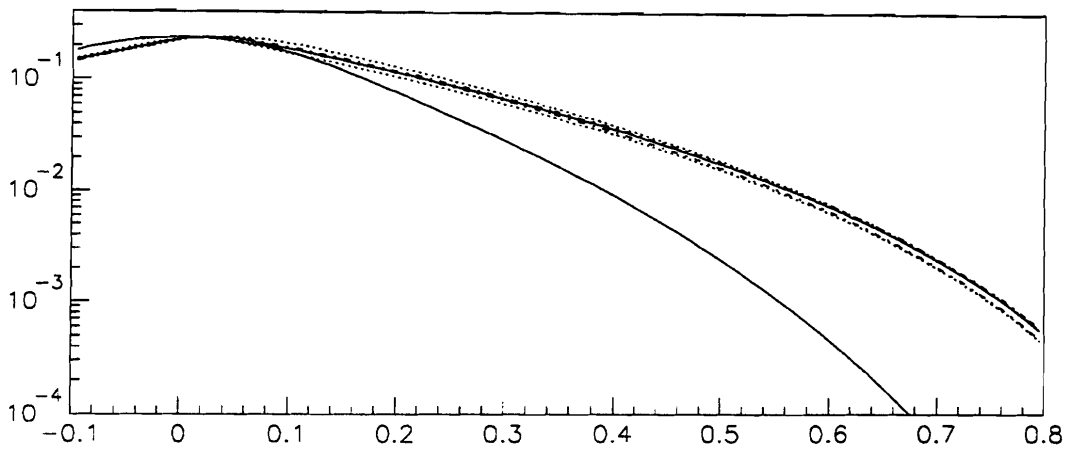

Figure 2.7: QCD NLO c quark $d\sigma/dx_F$ vs. x_F, default (solid, upper = π, lower = p), variation of μ_R by factor of 2 (dashed), variation of m_c by 300 MeV (dotted). Normalization is arbitrary.

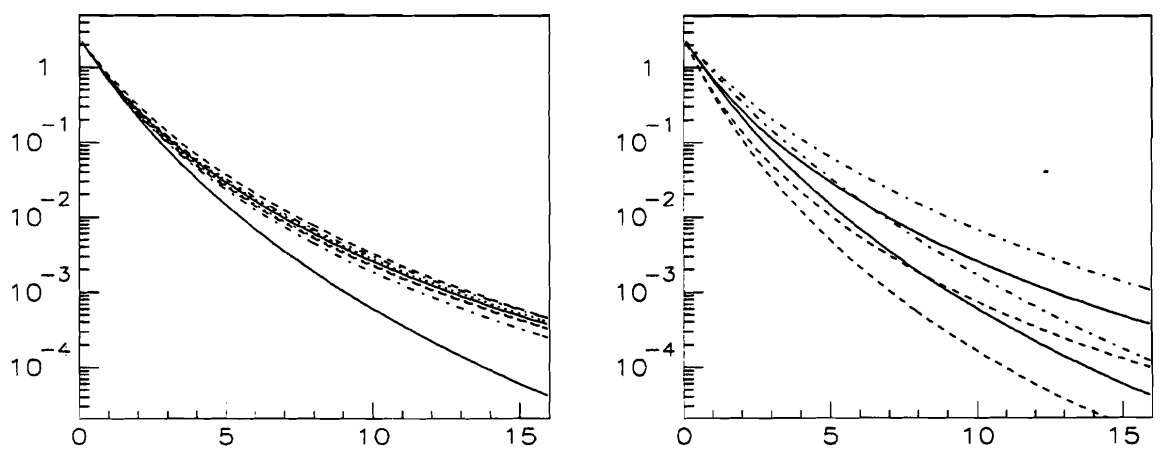

Figure 2.8: QCD NLO c quark $d\sigma/dp_T^2$ (GeV^{-2}) vs. p_T^2 (GeV^2); default (solid, upper = π, lower = p); Left: variation of μ_R (dashed) and μ_F (dash-dotted) by factor of 2, different π^- PDF sets (dotted); Right: m_c = 1.2 GeV (dash-dotted), m_c = 1.8 GeV (dashed). Normalization is arbitrary.

Chapter 3

Fermilab E769

During the 1986-87 fixed target run at Fermi National Accelerator Laboratory (Fermilab), approximately 400 million events were written to tape by the collaborators of Experiment #769 (E769). E769, an experiment designed to study the hadroproduction of charm (with a variety of beams and target materials), inherited the Tagged Photon Lab (TPL) spectrometer from its predecessor E691, whose purpose had been to study charm photoproduction. After the completion of E769 data taking, the TPL spectrometer was again put to use, this time by E791, a successor hadroproduction experiment which used a π^- beam to obtain an extremely large data set well-suited to high-statistics studies of charm production and decay. The TPL spectrometer, located at the end of the Proton East secondary beam line, underwent various changes and modifications through the years. In Fig. 3.1, a diagram of the detector as used by E769 is given. In this chapter we describe E769's mixed hadron beams, multifoil target, and various components of the TPL spectrometer, emphasizing those which are used in this analysis. Detailed descriptions of the experiment components can be found in the references cited in [6] and in references cited below for specific spectrometer components.

My personal involvement with E769 began in the spring of 1992, when I joined the collaboration with Prof. Paul Karchin as my thesis advisor. By that time, the experimental running and off-line event reconstruction had been completed. My contribution to the research effort therefore consisted of data analysis; one of my first

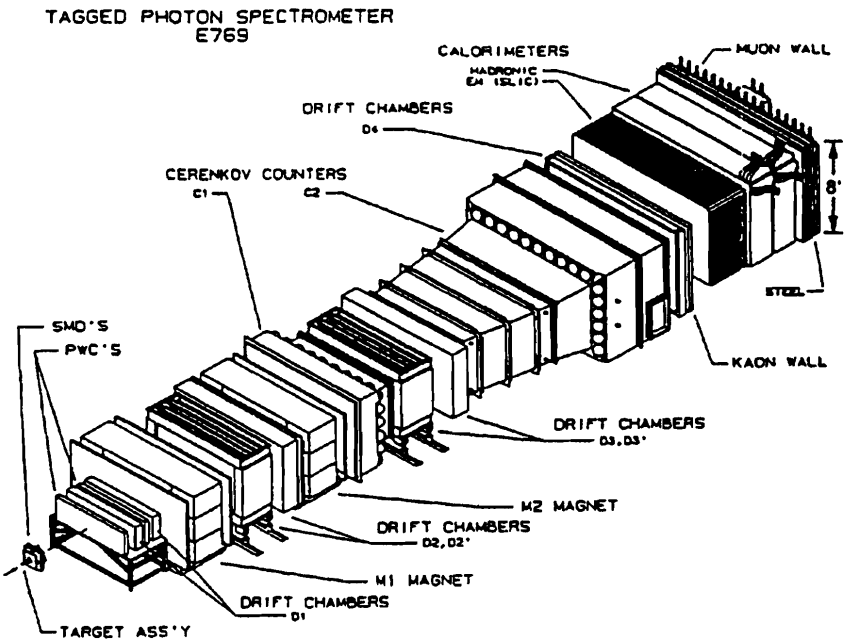

Figure 3.1: Tagged Photon Lab spectrometer.

tasks was to modify the program used to recontruct Monte Carlo events (Chapter 4) to include a simulation of the two-stage reconstruction used for the data.[1] The remainder of my time at Yale was spent executing the various stages of analysis (beginning at the substrip level) described in this thesis, the product of which are the measurements presented herein.

3.1 Beams

E769 uses secondary mixed hadron (π, K, $p\,(\overline{p})$) beams obtained by extracting protons from the Tevatron's 800 GeV beam, directing them into a Be target, and intercepting the products of the ensuing inelastic collisions. A dipole magnet is used to select the desired charge sign and momentum of the secondary beam; these particles are

[1]The second stage was necessary due to errors in the first attempt at event reconstruction (see Section 5.1).

collimated, focussed, and sent down the various fixed-target beam lines. Time scales characterizing the beam are determined by the acceleration and extraction processes. The radio-frequency electromagnetic field used to accelerate protons in the Tevatron confines beam particles in "buckets" of 1 ns duration coming every 19 ns. Extraction of protons from the Tevatron takes place in "spills" of 22 second duration every 60 seconds. Secondary beam particles reaching TPL are relatively isolated in time; on average only about one in 50 buckets is occupied.

In the first half of the experiment, the sign of the beam particles' charge was selected to be negative; this polarity was reversed to positive for the remainder of the running. Except for a period during which roughly 15% of the negative beam data was taken at 210 GeV, the beam momentum was kept at 250 GeV, corresponding to a hadronic center-of-mass energy of 21.7 GeV. The negative beam consists on average of 93% π^-, 5% K^-, and 1.5% $\bar{p}$, the positive of 61% π^+, 4.4% K^+, and 34% p; these percentages are known as *a priori* beam particle probabilities.[2]

Upstream of the target, eight proportional wire chamber (PWC) planes and two silicon microstrip detector (SMD) planes[3] allow for beam tracking, a capability which is not used in this analysis. As mentioned in Section 3.2, however, beam PWC hit information is used to facilitate beam particle identification in the positive running.

3.2 Beam particle identification

For purposes of this analysis, a beam particle is defined as positively identified if the calculated probability that its tag is correct is at least 90%. Two pieces of E769 apparatus are dedicated to the event-by-event identification of the three hadronic species in the beam: a differential isochronous self-focussing Čerenkov counter (DISC) and a transition radiation detector (TRD).[4]

The DISC operates through the detection of Čerenkov light emitted at a fixed

[2]These *a priori* probabilities are measured using DISC information (see Section 3.2).

[3]See Sections 3.4.2 and 3.4.1 for a description of PWC and SMD operation, respectively.

[4]The DISC and TRD are situated in the beam line upstream of the target assembly and are therefore not depicted in Fig. 3.1. Detailed descriptions of the DISC and TRD can be found in [20] and [25], respectively.

angle (24.5 mrad) with respect to the beam axis. Čerenkov radiation occurs when the speed of a charged particle in a medium exceeds the speed of light in that medium; the angle $\theta_{\check{C}}(B)$ at which beam particle B emits Čerenkov light is given by

$$\theta_{\check{C}}(B) = \frac{1}{n\,\beta(B)} = \frac{1}{n\sqrt{1+(m(B)/P_{beam})^2}}, \tag{3.1}$$

where $\beta(B)$ is B's speed normalized to the speed of light (in vacuum) and n is the index of refraction of the medium through which the particle passes, which in the case of the DISC is He gas. The velocities of the three hadron species are determined by the common momentum P_{beam} and their masses $m(B)$. The DISC is "set" to identify one of the three by tuning n, which for a gas increases with density. By adjusting the pressure of the He gas (given the current ambient temperature), a value of n is achieved such that $\theta_{\check{C}}(B)$ equals the angle at which reflected and focussed Čerenkov light passes through an annular slit and onto an array of eight photomultiplier tubes (PMTs), two in each quadrant of the transverse plane. Identification of a beam particle to which the DISC is set requires four or more coincident PMT hits, at least one in each transverse quadrant.[5]

The TRD is made up of 24 identical modules sitting in the beam line, each consisting of a transition radiator (TR) followed by a pair of PWC planes. Each TR is a set of eight polypropylene foils separated by gaps filled with He gas. Relativistic charged particles, upon traversing these alternating media, induce local time-dependent polarizations which radiate in a forward cone; the intensity of this radiation is proportional to $\gamma(B)$, where

$$\gamma(B) \equiv \frac{1}{\sqrt{1-\beta^2(B)}} = \sqrt{1+(P_{beam}/m(B))^2}, \tag{3.2}$$

thus enabling discrimation of beam particle species on the basis of mass. The PWCs are filled with a gas mixture (90% Xe, 10% methylal) which renders them more

[5]By plotting the number of positive DISC hits per unit beam flux as a function of He pressure, we obtain a "pressure curve", in which π, K, and p peaks are evident. Pressure curves were taken periodically during the experimental running; the relative areas of the three peaks provide a measure of the *a priori* beam particle probabilities.

sensitive to X-ray photons than to relativistic bremsstrahlung. The modules are designed so that, at E769's beam momentum of 250 GeV, detection of a photon in a given PWC plane is probable only for pions. Combining the outputs of the 48 PWCs allows for good separation in the response of the TRD to pions and non-pions. Identification of a beam particle as a pion requires that the number of TRD plane hits exceed a minimum cutoff ($\sim$12), which is calibrated periodically as running conditions change.

The $\overline{p}$ component of the negative beam is negligible. During the negative running, therefore, information from the DISC (set to tag kaons) alone is used in beam particle identification. In the positive running, where discrimination between three species is required, a two-step process using both the DISC and TRD is implemented. First, the output of the DISC (set to either kaons or protons) is examined. If positive identification results, the process ends. Otherwise, TRD output is used to separate pions from non-pions.[6] If the DISC is set to tag kaons, the absence of a DISC tag leads to positive identification of non-pions as protons.

The average efficiency of beam particle identification depends upon the species, the means by which it is identified, and the level of contamination tolerated in a B sample considered positively identified. Identification by DISC has an efficiency of roughly 40%, independent of B. TRD identification is even more efficient (80-90%, not including the PWC cluster cut efficiency). In all cases, the performance of E769's beam particle identification system exceeded the 90% correct-tagging standard used to define B samples; beam contaminations significantly lower than 10% are realized, as listed in Table 3.1.

In the vicinity of the TRD are two scintillators used in the event logic (see Sections 3.5 and 3.6) to signal the presence of incident beam particles.

[6]Accurate interpretation of the number of TRD plane hits relies upon the presence of only one beam particle per bucket; this is insured by requiring that the number of hit clusters found in the beam PWCs not exceed the number of planes. The average efficiency of this cut is measured to be 81%.

Beam	π	K	$p, \overline{p}$
π^-	–	3.8%	1.5%
K^-	1.0%	–	0.0%
π^+	–	0.0%	0.6%
K^+	0.1%	–	0.0%
p	0.3%	4.8%	–

Table 3.1: Beam contaminations.

3.3 Target

The E769 multifoil target is designed to allow study of the dependence of charm production on the atomic mass A of the nuclear target. A total of 26 foils (14 Be, 5 Al, 3 Cu, and 4 W), comprising approximately 2% of a nuclear interaction length, provide data points ranging over an order-of-magnitude in A. As discussed in Section 5.4, the widths of the foils ($\sim$100 μ for W, $\sim$250 μ for Be, Al, and Cu) enable more precise determination (in z) of charm production point positions than allowed by the vertex resolution achieved through SMD tracking (see Section 3.4.1).

Immediately upstream of the target foils are two scintillators, the beam spot and halo counters; downstream of the target foils is the interaction scintillator. The output of these three scintillators is used in the trigger logic (see Section 3.5) to signal the occurrence of interactions within the target. In addition, the interaction scintillator is considered in this analysis an additional target component, for a total target thickness of 2.5% nuclear interaction lengths. In Table 3.2, characteristics of these components relevant to cross-section or beam attenuation calculations are compiled.

In this analysis, linear dependence of charm production on A is assumed;[7] we therefore need only characterize the target in terms of its total "nucleonic thickness" (i.e., nucleons per unit cross-sectional area). In order to calculate attenuation of the beam upstream of and within the target, the thicknesses of each material must be

[7]See discussion in Section 8.1.

Material	total thickness (cm)	total nuclear interaction lengths (%)	density (g/cm^3)
Be	0.3629	0.892	1.848
Al	0.1261	0.320	2.70
Cu	0.0761	0.504	8.96
W	0.0383	0.399	19.3
int. scint.[a]	0.3175	0.395	1.02

[a]The interaction scintillator is made of polyvinyltoluene, characterized by a H/C ratio of ~1.1.

Table 3.2: Target component characteristics.

expressed in terms of nuclear interaction lengths, which are derived from nuclear inelastic cross-sections (σ_I); these cross-sections, in addition to depending on the beam particle species,[8] exhibit A-dependence of the form $A^{0.71}$. As defined in Section 8.1, the formula for effective beam particle flux (as "seen" by a process linear in A) must therefore incorporate the attenuation factors χ_{att}, equal to 98.2% (98.8%) for proton (meson) beam(s).

The (right-handed) coordinate system with which we define the spectrometer has its origin on the beam line immediately downstream of the interaction scintillator. The z-axis is the beam line; z is positive downstream of the origin. The y-axis points upward (towards the roof of TPL). The active target region lies within the range $-5.5 < z < 0.$ cm.

3.4 Charged particle analysis

Analysis of secondary charged particles, which for the most part are produced within the target, consists of three correlated tasks: tracking, momentum measurement, and identification. The detector components described in this section are designed to

[8]At E769's center-of-mass energy, $\sigma_I(pp) \simeq \sigma_I(pn) \simeq 33$ mb, while $\sigma_I(\pi N) \simeq \sigma_I(KN) \simeq 20$ mb.

provide the information used in the reconstruction of charged particle 4-momenta, a process described in Chapter 5.

3.4.1 Silicon microstrip detector

High-resolution tracking of charged particles, allowing for separation of production and decay vertices for charm meson species, is made possible through the use of a silicon microstrip detector (SMD), located immediately downstream of the interaction scintillator ($0.2 < z < 23.9$ cm). The SMD consists of eleven 300 μ thick silicon planes, each of whose upstream (downstream) surfaces have been imbedded with B (As) atoms to form a p(n)-type semiconductor layer. The diffusion of holes (electrons) from the p(n)-type surfaces into the Si inner region creates an electric field directed toward the upstream surface; this field is strengthened by the application of an external voltage (70-90 V). When a charged particle passes through the plane, the resulting ionization creates electron-hole pairs; the electric field sweeps the electrons (holes) to the n(p)-type surface. This voltage signal is picked up by the nearest member of a parallel array of instrumented Al electrodes deposited onto the upstream surface at a pitch of 50 μ (25 μ for the two most upstream planes). Each SMD plane therefore measures the transverse location of the charged particle in the direction perpendicular to the orientation of the Al microstrips. Of the eleven planes, 4 are x-view, 4 are y-view, and the remaining 3 are v-view, where the v-axis is formed by a right-handed rotation of the x-axis by 20.5° in the transverse plane. The number of instrumented channels on each plane ranges from 300 to 1000.

The 25 (50) μ planes have typical efficiencies of 70% (92%) and resolutions of 16 (21) μ; these resolutions can be compared with the RMS deviation of a flat distribution with the appropriate pitch width: 7 (14) μ. As a whole, the SMD system provides vertex resolution of $\sim$15 μ in the transverse plane; vertex resolution in z is on the order of hundreds of microns. The charged track multiplicity of a typical event is 10-15, resulting in SMD channel occupancies on order of a few percent.

3.4.2 Drift chambers

Downstream of the SMD system, four sets (D1-D4) of drift chambers (DC), interspersed among two analysis magnets (M1 and M2), are used for momentum and charge sign measurement of charged particles. Each of the sets consist of 1-4 assemblies; each assembly contains a set of 3-4 sense wire planes bathed in a 1:1 Ar-ethane gas mixture. Alternating with the sense wire planes are HV cathode planes formed by parallel wires held at a voltage of -2400 V. Each sense wire plane is made up of alternating sense and field-shaping wires; the former are grounded while the latter are held at -2000 V. The resulting field configuration is designed so that free electrons drift with uniform speed towards the nearest sense wire. When a charged particle passes through the DC gas, ionization occurs. Acceleration of these liberated electrons into other gas molecules causes secondary ionization, increasing the voltage signal received when the electrons reach the sense wire. The constant drift velocity allows the use of timing information in improving the spatial resolution beyond that obtainable on the basis of sense wire pitch alone; a two-fold degeneracy in this measurement results, however, from not knowing the direction from which the electrons drifted.

DC set	number of assemblies	pitch (cm)	active area (m^2)	average z position (m)	views per assembly
D1	2	0.5	0.91	1.75	$uvxx'$
D2	4	0.9	3.9	4.43	uxv
D3	4	1.5	4.6	9.89	uxv
D4	1	3.0	13.3	17.45	uxv

Table 3.3: DC parameters.

Each plane measures a transverse coordinate in one of four views: x, x', u, or v. The sense wires of x and x'-view planes are in alternating positions, thereby alleviating the measurement degeneracy in that dimension; the u and v views measure positions along axes obtained by a 20.5° right(left)-handed rotation of the x-axis. Important DC parameters for the four sets are given in Table 3.3. As shown in Fig. 3.1, the

DC sets are located (D1) between the SMD and M1, (D2) between M1 and the first Čerenkov counter (C1), (D3) between M2 and the second Čerenkov counter (C2), and (D4) between C2 and the calorimeters.[9] DC tracking is supplemented by two y-view PWC planes of 0.2 cm pitch, which are interspersed with the D1 assemblies. The operating principle behind a PWC is similar to that of a DC; for the former, however, timing information is not used to improve the spatial resolution beyond that determined by wire pitch.

Plane efficiencies for the DC system range from 68-92%; resolutions on the order of a few hundred microns are typical. Each DC plane has a central region of reduced efficiency due to the high passage rate of particles near the beam line; the shapes of these "holes" are measured and parametrized for each assembly so that this effect may be incorporated into the MC simulation of the spectrometer (see Section 4.2).

3.4.3 Magnets

Momentum analysis of charged particles consists of tracking their trajectories into and out of a known magnetic field (and correctly matching the two track segments). The angular deflection of the track (as measured by DC tracking) and the p_T "kick" given to a relativistic charged particle passing through the magnet determine the particle's momentum. Parameters for E769's two analysis magnets (M1 and M2) are given in Table 3.4. The fields of these magnets are oriented along the y-axis.

For charged tracks passing through M1 and M2, the fractional momentum resolution is given by

$$\frac{\delta p}{p} = \sqrt{(0.1\%/\mathrm{GeV} \times p)^2 + (0.5\%)^2}, \tag{3.3}$$

where the second term arises from multiple scattering.

[9]Tracks are conceptually divided into four categories, depending on which DC sets they traverse. These categories are labelled by the variable JCATSG, which takes on values 1, 3, 7, or 15 for tracks which penetrate past D1, D2, D3, and D4, respectively. This analysis uses only JCATSG $\geq$ 3 tracks, i.e., tracks which have passed at least through M1.

Magnet	M1	M2
entrance aperture (cm^2)	154×73	154×69
exit aperture (cm^2)	183×91	183×86
geometrical acceptance ($mrad^2$)	$\pm 240 \times \pm 120$	$\pm 120 \times \pm 60$
z length (m)	1.65	2.08
current (kA)	2.5	1.8
p_T kick (GeV)	0.21	0.32

Table 3.4: Magnet parameters.

3.4.4 Čerenkov counters

E769's two threshold Čerenkov counters (C1 and C2) are located just downstream of D2 and D3, respectively. Unlike the DISC, which identifies a beam particle of known trajectory by detecting Čerenkov light emitted at a fixed angle, the downstream detectors are designed to identify multiple charged tracks passing through their respective gaseous medium at various angles and at the same time. As discussed in Section 3.2, Čerenkov light is emitted when the speed of a charged particle in a medium exceeds the speed of light in that medium, given by c/n, where c is the speed of light in vacuum and n is the index of refraction of the medium. This threshold for Čerenkov radiation can be rewritten in terms of the mass and momentum of the particle:

$$\frac{p}{m} > \sqrt{n^2 - 1}. \tag{3.4}$$

From this relation it is clear that, for a given n, charged particles emit Čerenkov light above a momentum threshold proportional to their mass. By correlating the responses of two detectors filled with gases of different n to a given particle of known momentum, discrimination between π, K, and p is possible in a momentum range bounded by the lower π and higher p thresholds. C1 (C2) is filled with N_2 (80% N_2, 20% He) gas, which at operating density has an n value of 1.000350 (1.000088). The logical states of the two detectors are given in Table 3.5.

Momentum range (GeV)	π	K	p
0 - 6	(0,0)	(0,0)	(0,0)
6 - 9	(1,0)	(0,0)	(0,0)
9 - 20	(1,1)	(0,0)	(0,0)
20 - 36	(1,1)	(1,0)	(0,0)
36 - 38	(1,1)	(1,1)	(0,0)
38 - 69	(1,1)	(1,1)	(1,0)
> 69	(1,1)	(1,1)	(1,1)

Table 3.5: (C1,C2) logical states. 1 = on, 0 = off.

At the downstream end of each counter, a segmented mirror, designed to minimize the overlap in a single mirror of Čerenkov photons from separate particles, allows for simultaneous identification of multiple particles. The reflected light from each mirror is focussed by a conical light guide for collection by a particular PMT. In this analysis, C1 and C2 information is used only to exclude identified pions as candidate kaons. See Section 7.2.2 for a discussion of the kaon identification efficiency achieved by the Čerenkov counter pair.

3.5 Triggers

During the E769 running, beam particles impinged upon the target at a rate of ~1 MHz. Given the 2.5% interaction length target, physics events of some kind are expected to occur at a rate on the order of 25 kHz. The E769 data acquisition (DA) system[10] can only write events to tape at 450 Hz, thus requiring a rejection factor of roughly 50 be applied to interaction events; this is the job of the E769 triggers. Fast on-line electronics convert various experimental analog signals into binary logical signals (bits); event triggering is implemented by inputting these as well as other user-defined bits (e.g., prescalers) into a programmable logic unit (PLU), which outputs

[10]Detailed descriptions of the E769 DA system can be found in the references listed in [40].

for each trigger type a binary signal defined as a logical operation on some number of input bits. One PLU input bit which is included in the logical definitions of all trigger types is the strobe signal; this indicates that the DA system is not currently busy with another event. Output of a PLU trigger bit signals the DA system to write the current event to tape; the logical states of all PLU input and output bits are included as data words in the event, allowing for off-line identification of the trigger type(s) under which it was written to tape.

The most basic trigger type is the interaction trigger, which indicates that a beam particle has entered the target and that an inelastic interaction has occurred. Specifically, coincident signals[11] are required from the two TRD beam scintillators, the beam counter, and the interaction scintillator. This last signal must exceed a threshold corresponding to the passage of more than five minimum-ionizing charged particles. In addition, a signal from the beam halo counter acts as a veto. In and of themselves, interaction trigger events are not particularly interesting for purposes of studying charm; as described in Section 7.2.1, however, the efficiency of each combination of trigger types used in this analysis is measured with respect to that of the (unprescaled) interaction trigger. Therefore, this trigger is written to tape, but is prescaled by a factor ranging from 100-600; interaction triggers make up about 5% of the data set. Note that the input bit combination defining the interaction trigger (excepting its prescaler) is required in the logical definitions of all other trigger types as well.

By comparing the cross-section predicted for $c\bar{c}$ production with that measured for all inelastic collisions, we see that less than 0.1% of interaction trigger events are expected to contain charm. E769 makes use of transverse energy (E_T) triggers to enhance the charm content of the data set written to tape. Although calorimeter information is not directly used in this analysis, it provides the means of triggering on events with E_T above a desired threshold. We therefore give a brief description of the calorimeters before proceeding to define the different trigger types.

E769's calorimeters are located downstream of D4. Electromagnetic calorimetry

[11]Logical simultaneity is achieved by delaying signals by amounts given by their relative positions and proximities to the electronics.

is provided by the segmented liquid ionization calorimeter (SLIC), which consists of 60 alternating layers of lead absorbers and liquid scintillator, comprising 20 radiation lengths. The scintillating liquid is confined to corrugations of a teflon-coated aluminum sheet bent into a square wave; these corrugations form light guides leading to PMT channels. Each scintillator layer therefore allows characterization of an electromagnetic shower in the u, v, or y-view, as previously defined. The pitch of the detector is given by the half wavelength of the Al square wave, 3.17 cm. Behind the SLIC is the hadrometer, a 6-absorption-length hadronic calorimeter made up of 36 alternating layers of steel absorbers and plastic scintillator. The plastic scintillator is apportioned into 14.5 cm wide strips, leading to PMT channels and providing energy deposition measurements in the x and y-views.

The quantity E_T is a weighted sum of energy deposited in the calorimeter channels, where the weighting factor is the distance from a given channel to the beam line. This summation takes place over a 200 ns window, corresponding to about 10 buckets. Events whose E_T exceeds a threshold of about 5.5 GeV turn on the ETin bit; a higher threshold ($\sim$8 GeV) defines the EThigh bit.[12] Additional physical PLU input bits include the occurrence of a DISC signal (satisfying the requirements detailed in Section 3.2) and the measurement of an energy deposit of $E_T > 0.5$ GeV in a single SLIC y-view channel (ELEC), signaling the presence of a high-p_T electron. During most of the positive running, the $\overline{\text{KB}}$ bit is used to disallow events followed closely (within 150 ns) by another beam particle; this lessens the contamination of E_T by energy from neighboring "out-of-time" events. The logical definitions of the trigger types used in this analysis are given in Table 3.6. Note that prescaler settings varied during the running, ranging from 5-60 (1.5-100) for ETπ (ETB).

As detailed in Section 6.2, various combinations of these trigger types characterize events making up the data subsets used in this analysis. The efficiencies of these trigger combinations are given in Section 7.2.1. The efficacy of E_T triggering for charm is evidenced by difference in the typical ETin bit efficiency for charm and generic interaction events: 80% and 25%, respectively. In the negative (positive) running, ETK triggers are used to enhance the fraction of events caused by interactions of

[12]These thresholds were subject to some variation during the E769 running.

Trigger type	PLU input bits
ETπ	ETin $\cdot$ PS_1 $\cdot$ $\overline{KB}$ [a]
ETB	EThigh $\cdot$ PS_2 $\cdot$ $\overline{KB}$ [a]
ETK	ETin $\cdot$ DISC
ETe	EThigh $\cdot$ ELEC $\cdot$ $\overline{KB}$ [a]

[a]The $\overline{KB}$ bit was operative only during the positive running.

Table 3.6: Logical definitions of trigger types.

kaon (kaon or proton) beam particles with the target.

3.6 Scalers

In order to provide an absolute normalization for the forward cross-section calculations, the number of beam particles incident on the target must be counted. In addition, running tallies of various experimental quantities provide valuable diagnostic information during both the running (as witnessed by the name "counting room") and analysis phases[13] of the experiment. For these purposes, E769 implemented a multitude of scalers into the electronic logic of the DA system. In this section, we discuss only those used in this analysis.

The "good beam" scaler N_{BEAM} takes as its input the same signals as the interaction trigger, with the exception of that from the interaction scintillator. In other words, N_{BEAM} counts the number of beam particles impinging of the target; the veto provided by the beam halo counter insures that the beam particle actually hits the target. Another important beam scaler is N_{DISC}, which counts the number of four-fold coincidences in the DISC (with at least one hit in each quadrant). The role of each of these scalers in the forward cross-section calculations is detailed in Section 8.1.

The average fraction of time that the DA system is available for event writing

[13]For example, nonsensical values of certain scaler ratios recorded in a particular spill are used to throw out that spill as "bad" in the off-line event weeding process, discussed in Section 6.1.

is known as the detector livetime ϵ_{live}; this quantity figures directly in the cross-section formula. The livetime is calculated as a ratio of scalers, specifically the ratio of the scaler downstream of the PLU counting prescaled interaction triggers to the corresponding upstream scaler. Since the PLU is disabled while the DA system is busy with an event, this ratio provides a direct measure of ϵ_{live}. Values of $\sim$75% for ϵ_{live} are typical.

Chapter 4

Monte Carlo

The response of an individual spectrometer component (e.g., SMD plane or Čerenkov counter) upon passage of an energetic charged particle through its volume is in general well understood through first principles, direct measurement, or some combination of the two. Tracing the life history of a particle through multiple detector components, from its birth in, say, the target until its decay or escape further downstream, is considerably more complicated. Multiple scattering and energy loss due to interactions with the detector material must be considered. In addition, the effective efficiencies of the detector components are typically impacted by the presence of other particles in the event.

In this analysis, charm particle signals are extracted from raw data by reconstructing their charged decay products (see Chapter 5 for a description of this process). Absolute normalization of cross-sections requires that the correlated detector responses from each particle in the event (charm decay products as well as particles from the "underlying" event) be linked to yield an overall average detection efficiency or "acceptance" (see Section 7.1 for a precise definition). The final acceptance is an average over several distributions that can only be defined probabilistically; in addition to the variable detector responses alluded to above, we must average over the momentum and lifetime distributions of the produced charm particle, the Dalitz distribution of its decay products, and relevant distributions characterizing the underlying event. This last aspect of the problem is especially difficult: final-state

particles and intermediate-state partons are connected by hadronization, a process which cannot be treated perturbatively.

Acceptance is essentially given by a tremendously complicated n-dimensional integral, one for which an expression cannot even be written down, much less evaluated. The standard solution to this dilemma is to create a computer model of the complex interaction between an event containing a given charm decay and the spectrometer. By generating[1] N events and determining what fraction of them make it into the final invariant mass plot (Monte Carlo integration), the acceptance is calculable to a precision which depends on N.

This Monte Carlo (MC) simulation can be divided into two parts: event generation and digitization. In the first, the complete history of an event containing a specified charm decay is spelled out step-by-step, leading to a "truth table" representation of the event: a list of the 4-momenta and positions of all produced particles. In the digitizer, the characteristics of the individual detector components allow conversion of the truth table into the raw data format used in the actual E769 data set. From this point forward, this "fake" data is analyzed like real data, except that MC events are weighted to incorporate effects that are not simulated with sufficient accuracy (or at all) in the MC program itself. These weighting procedures are detailed in Section 7.2. Event generation and digitization are described more fully in Sections 4.1 and 4.2, respectively.

4.1 Event generation

The first task of the E769 event generator is to create a $c\bar{c}$ pair. Although the program is set up to simulate collisions of different beam hadrons (at 250 GeV momentum) on the nuclear target, in practice only π^- is used. For target protons and neutrons (beam pions), momentum distributions of the constituent partons are given by the PDFs of Duke and Owens (Owens) [24]. LO QCD amplitudes for gg fusion and $q\bar{q}$ annihilation are used to generate the momentum distribution of the produced

[1] At each "decision point" in the event, a random number generator is used to pick a value from the relevant probability distribution.

charm pair. To LO, charm correlations are trivial: the c and $\bar{c}$ quarks are created back-to-back in the partonic center-of-mass frame. The underlying partonic event is modelled using the Lund software package FRITIOF 1.3 [14]. FRITIOF is designed to simulate hadron-nucleus collisions; it allows multiple soft interactions to occur between spectator quarks, taking into account the effects of the nuclear environment.

Hadronization of the quarks into particles is modelled using the Lund program JETSET 6.3, which implements a string fragmentation model [13]. Those particles which are unstable are decayed assuming 1990 Particle Data Group (PDG) average lifetime values and branching fractions.[2] At this point, it is not crucial that the MC simulation return charm particle momentum distributions; as detailed in Section 7.2.3, MC events are weighted in x_F and p_T in order to bring in line generated and measured distributions in these variables.[3] Lifetime weighting (Section 7.2.4) is also used to update assumed charm lifetimes to 1994 PDG[4] values.

The final phase of event generation is simulation of the interactions of the particles with the detector itself. In addition to propagating charged particles through the magnetic fields of M1 and M2, the MC program generates Čerenkov photons in C1 and C2 and electromagnetic and hadronic showers in the calorimeters. The effects of multiple scattering and secondary interactions on particle trajectories are also modelled. The resulting truth table list of particle momenta and locations (birth and death) is input to the digitization stage of the MC program.

A separate set of MC events must be generated for each charm decay mode of interest. For each of the decay modes $D^+ \to K\pi\pi$, $D^0 \to K\pi$, and $D_s \to \phi\pi$, 150K MC events were generated; 200K $D_s \to K^*K$ MC events were generated. The two D_s decays, however, were not specified completely; the secondary decays $\phi \to K^+K^-$ and $K^* \to K^-\pi^+$ were not forced during event generation. As a result, the numbers of useful MC events for the D_s modes are reduced to the number of generated events

[2]The mode to which the charm particle decays is fixed by the user.

[3]In nonresonant three-body decays, the Dalitz distributions of charm decay products depend on the decay model used by the MC generator. In studying D^+ and D_s decays to three pions, however, the E691 collaboration determined that, for these modes, acceptance of the TPL spectrometer is "uniform" over the 3π Dalitz plot [15].

[4]Full citations for the 1990 and 1994 editions of the PDG Review of Particle Properties are given in [34] and [35], respectively.

multiplied by the Lund branching fractions of their secondary decays, 49.5% and 66.7% respectively. No separate D^* MC was generated; that fraction of the generated D^0's produced from D^* decays (about 30%) is used.

4.2 Digitization

In the digitization phase of the MC, the fully-specified event of the truth table is translated into the language of the experiment itself: responses in thousands of SMD, DC, PWC, and PMT channels. The presence or absence of a "hit" in a particular channel is a function not only of the track geometry but also of the efficiency of the relevant detector component. In order to simulate a real raw data event accurately, detector contingencies such as hot or dead channels and the presence of random noise hits must also be taken into account. After measuring each of the aforementioned aspects of spectrometer performance, the corresponding parameters in the digitizer program are tuned to bring about the same result. However, in two important experimental areas (Čerenkov counters and transverse-energy triggers), the MC simulation is not sufficient to return reliable estimates of average efficiency. In these cases, therefore, MC event weighting is implemented, as described in Sections 7.2.2 and 7.2.1, respectively.

Experimental conditions did not remain constant over the entire period of data collection. The most important changes were to the average SMD and DC plane efficiencies; as the average beam flux increased in the second half of the experimental running (i.e., positive beam polarity), these efficiencies decreased. Therefore, average efficiencies measured in these separate time periods are each used to create a corresponding version of the digitizer code. These are called the "negative" and "positive" digitizers; the difference in the overall efficiencies returned by these two versions is significant, as seen in the geometric acceptances compiled in Table 7.5.

Due to the problematic history of two DC planes, specifically the u and v views of assembly 2 of D1 (D12u and D12v), the positive "default" digitizer as originally written had to be modified. About halfway through the positive running (by flux), these two planes became inoperative, reducing their average efficiencies from 85-90%

down to zero. This condition persisted for some period thereafter (corresponding to roughly 15% of the positive flux); then the v view plane was fixed, returning it to its previous efficiency. The u view plane remained down for the rest of the experiment. These three operating conditions are labelled "on/on", "off/off", and "on/off", respectively.

The default digitizer did not use correct average efficiencies for these two planes. It was determined, however, that even upon correction of these average efficiencies, the "modified" digitizer does not return accurate values for acceptance (the $D^+ \to K\pi\pi$ mode was used in these studies); the dependence of the acceptance on these plane efficiencies is sufficiently non-linear to require separate digitizers be used for each operating period. In other words, the flux-weighted average of "on/on", "off/off", and "on/off" acceptances is found *not* to equal (within statistics) the acceptance returned by the modified digitizer, which used flux-weighted average D12u and D12v plane efficiencies. Moreover, these three operating regions overlap quite differently with the two positive run regions used in the analysis (see Chapter 6 for the definitions of the four E769 run regions). Threefold digitization of positive beam events for all decay modes in this analysis would have been prohibitive. The results obtained with the $D^+ \to K\pi\pi$ mode are therefore used to calculate correction factors for the acceptances returned by the positive digitizer for the other modes; these factors are described and given in Section 7.2.5.

Generated events for all decay modes undergo both negative and positive digitization. In the case of the $D^+ \to K\pi\pi$ and $D^0 \to K\pi$, the modified positive digitizer is used; MC events for the D_s modes, however, are digitized using the default positive digitizer. As described above, the positive running $D^+ \to K\pi\pi$ acceptances are calculated using three separate digitizers; the acceptance returned by the modified digitizer is used only to obtain correction factors for the other decay modes.

Chapter 5

Analysis

In this chapter, we detail the analysis, beginning in event reconstruction and ending in the application of optimal analysis cuts, carried out on raw data – both the ~400 million *real* events written to 6250 bpi tapes during the course of the experiment and the *fake* events obtained by digitizing the output of the MC generator.

5.1 Event reconstruction

Reconstruction proceeds in three stages: PASS0, PASS1, and PASS2. In PASS0, the first 2000 events from each tape are used to collect miscellaneous statistics useful in troubleshooting, beam particle identification, and calibration. These include hot SMD channels, pion and proton peaks in the TRD distributions, and ADC pedestals. During PASS1 and PASS2, various other bookkeeping activities coming under the PASS0 umbrella are carried out on an event-by-event basis.

In PASS1, charged particle trajectories in the four regions of the spectrometer are found by fitting SMD and/or DC hits into straight-line segments called "tracks". Tracks found in the SMD system, with its high resolution and efficiency and low noise, (with corroboration provided by D1 and downstream PWC hits) are linked to tracks downstream of M1 (provided by D2-D4). Assuming a single bend point, linking begins in the y-z plane (on track projections which are straight lines in this appromixation) and continues in the x-z view. The resulting track candidates are

then refit using the full magnetic field mapping, and momenta are determined.

In PASS2, the tracks found in PASS1 are projected through the electromagnetic and hadronic calorimeters. This allows for measured showers (energy depositions above threshold in contiguous channels) in the calorimeter to be associated with charged tracks or, if this is not possible, identified with neutral particles. In the former case, the shape and penetration of the shower is used to distinguish electrons and muons from hadrons.

If the charged track is more consistent with being a hadron than a lepton, Čerenkov information is used to distinguish between pions, kaons, and (anti)protons. The track in question is projected through C1 and C2; in each counter, the number of photoelectrons produced in the relevant phototube channel is counted and used to calculate the probabilities that the track in question can be identified with π, K, or p. The final set of particle-ID probabilities is the normalized product of the C1 and C2 probabilities and the *a priori* probabilities[1] for charged secondaries in E769 events.

The final phase of PASS2 is the compilation of a vertex list. Fits are performed on groupings of SMD tracks, to which tracks are iteratively added one by one until the vertices with the largest number of tracks that are consistent with a quality cut of χ^2/dof less than 2 are obtained. The process continues among the leftover tracks. Except for the vertex with the highest number of tracks (which is identified with the primary vertex), none of the vertices in this list are used in subsequent analysis; secondary vertex fits are attempted for *all* track combinations consistent with a particular decay mode hypothesis.

Upon completion of PASS2, nonessential information is discarded and the remaining portion of each event is written in a compressed Data Summary Tape (DST) format onto an 8 mm 2.3 Gbyte exabyte tape. Several hundred tapes comprise the reconstructed data set.

An error was discovered in E769's reconstruction code after the data had been processed. In the software specification of the detector elements, the z positions of two adjacent SMD planes (x and y-views) had been transposed. This mistake obviously impacted the quality of the track fits and increased background by introducing an

[1]These *a priori* probabilities are as follows: 2% e, 1% μ, 81% π, 12% K, and 4% p.

additional source of spurious (by their misplacement) hits. Rather than re-reconstruct the entire data set, the collaboration decided to correct the reconstruction program and run it only on a subset of the data that had been filtered to enhance charm content. This filter, known as the pair strip, selects events containing two-track vertices well separated in z from the primary vertex; it is described in Section 5.3. This procedure (reconstruction $\rightarrow$ pair strip $\rightarrow$ corrected reconstruction) is carried out on both the data and the MC events used in this analysis.

5.2 Cut variables

For purposes of this analysis, each event after reconstruction consists of a set of charged particles whose trajectories, momenta, and charge sign are measured. Assigned probabilities for the possible identities of each charged particle differ from *a priori* values when additional information is available. Each event also contains a vertex list representing plausible groupings of particles based on their proximities at birth. In addition to this "final-state" portion of the event, information relevant to normalization (e.g., spill number and trigger type) and beam particle identification (e.g., DISC and TRD output) is also needed for cross-section measurements. In this chapter, however, we are concerned only with characterization of events in terms of their charm content.

Although three of the four D mesons which we attempt to reconstruct are charged, they are much too short-lived[2] for any attempt to be made to track their paths from production to decay directly. Rather we obtain the 4-momentum of the D by summing the 4-momenta of its charged decay products.

Even after the imposition of a transverse energy trigger, we expect only a minority of the remaining events to contain charm particles; the challenge of isolating these events remains. In addition, E769 events typically contain more than a dozen

[2]See Table 7.2 for a list of average lifetimes τ of the pseudoscalar D mesons. (Vector D's decay to pseudoscalar D's "instantaneously".) Take, for example, the relatively long-lived D^+ ($c\tau = 317\mu$). Boosting from the rest frame of D^+'s produced at some fixed value of x_F, we obtain an exponentially-falling distribution of lab-frame birth-to-death z-spans (Δz) already greatly diminished at a distance of one centimeter. In other words, the vast majority of produced D's decay while still in the target region.

charged tracks. Therefore, even for a *pure* sample of charm events (realizable in MC), we expect invariant mass plots generated from all track triplets[3] to be plagued by an unacceptably high level of combinatoric background. In order to do reduce this background, selection criteria or "cuts" are applied to each triplet; these cuts are designed to favor the passage of real charm decays over randomly-associated tracks (which we'll call "fake decays"). Both the topology of particle production and decay in general and the kinematics of charm decays in particular are exploited in defining quantities whose distributions for real and fake decays differ significantly. If for a particular cut variable this difference is great enough, a cutoff value (above or below which triplets are thrown away) can be found which leads to a high rejection of fake decays while retaining a reasonable fraction of the actual charm signal. In this section, we define the cut variables used in this analysis.

E769's vertex resolution in z is on the order of hundreds of microns. Given that D lab-frame z-spans of millimeters are typical, it is clear that we should be able to make significant measurements of D lifetimes. Moreover, since most tracks in a minimum bias event emanate from the primary interaction point, we expect the separation in z of the primary and secondary vertices to be useful as a cut variable. Rather than cutting on Δz directly, however, the effect of variable z resolution is diminished by measuring Δz in units of $\sigma_{\Delta z}$, where

$$\sigma_{\Delta z} = \sqrt{\sigma^2_{z\,primary} + \sigma^2_{z\,secondary}}. \tag{5.1}$$

The σ's for each vertex ("primary" indicates production, "secondary" indicates decay) are the expected standard deviations in z (based on the number of tracks making up a vertex, their quality, and the effect of multiple scattering) returned by the least-squares vertex fitting algorithm. We call the resulting ratio SDZ (which stands for "significance of Δz"); it is given explicitly by

$$\mathrm{SDZ} = \frac{\Delta z}{\sigma_{\Delta z}} = \frac{z_{secondary} - z_{primary}}{\sigma_{\Delta z}}. \tag{5.2}$$

[3]In this analysis, D^0 decay products form only a pair. Nevertheless, the term "triplet" is used to designate any set of secondary charged tracks nominated as a candidate for a particular charm decay.

From now on we will abbreviate "*primary*" and "*secondary*" to "*pri*" and "*sec*", respectively.

At this point, we should define exactly what is meant by z_{pri}. The vertex in the standard vertex list made up of the most tracks is designated the primary vertex.[4] If a given triplet, however, contains one or more tracks from this vertex, they are removed and the primary vertex is *refit* using only the remaining tracks. Variables such as z_{pri} and $\sigma_{z\,pri}$ are the results of these adjusted fits.

Another property which distinguishes charm decays is the large amount of kinetic energy available to the decay products. The pseudoscalar decays reconstructed in this analysis have Q values on the order of a GeV, leading to decay pions and kaons which are relativistic in the charm parent's rest frame. By summing the squares of p'_T for each decay product, where p'_T is the momentum transverse to the lab-frame composite momentum ($\vec{P} \equiv \sum_i \vec{p}_i$), we obtain a measure (called PT2DK) of the energy of the secondaries:

$$\text{PT2DK} = \sum_i (p'_T)_i^2, \tag{5.3}$$

where i runs over the decay products. Momenta are evaluated in the lab frame.

The hypothesis that a given secondary vertex is a real decay is strengthened if the composite momentum points back to the most probable point of production, the primary interaction vertex. The cut variable DIP is defined as the transverse impact parameter (b_T) of the candidate D with respect to the primary vertex:

$$\text{DIP} = (b_T^{pri})_D. \tag{5.4}$$

The x and y coordinates of the D at z_{pri} are obtained by using the measured slopes dP_x/dP_z and dP_y/dP_z to work backward from the measured position of the secondary vertex.

For a given triplet, we'd also like to have confidence that on average the tracks are more consistent with originating from the secondary vertex than from the primary

[4] Alternative methods for picking the primary vertex, such as using the most upstream vertex in the target region, were compared in MC studies with the procedure actually used; the latter was found to be the best predictor of the true primary interaction point.

vertex. For each decay product, the ratio of the transverse impact parameters with respect to the secondary and primary vertices are calculated. The product of these ratios is called RAT:

$$\text{RAT} = \prod_i \left(\frac{b_T^{sec}}{b_T^{pri}}\right)_i. \tag{5.5}$$

In grouping charged tracks into triplets, we don't want to confuse the correct decay vertex with one which is formed using only an incomplete subset of the tracks actually emanating from the vertex (e.g., selecting a $K\pi\pi$ triplet from a $K\pi\pi\pi$ decay). Therefore, an upper requirement is placed on the smallest $(b_T^{sec})_j$, where j runs over all tracks which are *not* members of the triplet. This minimum transverse impact parameter is called ISO:

$$\text{ISO} = \min((b_T^{sec})_{j,j\neq i}). \tag{5.6}$$

All of these cut variables have been defined without making any assumptions about the identities of either the charged particles associated into a triplet or their putative parent. In addition to these ID-neutral cut variables, we have at our disposal the standard measures of track and vertex quality, χ^2 per degree of freedom (χ^2/dof). These dimensionless quantities are obtained from the least-squares fitting algorithms used to construct tracks from SMD and DC hits or to construct vertices out of groups of said tracks. For each track determined using information from the SMD (the only class of tracks used in this analysis), separate χ^2/dof measures are available corresponding to whether DC and SMD hits or SMD hits alone are used; these are labelled χ^2/dof_{global} and $\chi^2/dof_{silicon}$, respectively. As described below, the cuts that are placed on these quantities in this analysis are too loose to have much impact.

5.3 Pair strip

Following reconstruction, a high-rejection event filter is implemented whose purpose is to produce a data set of manageable size with a fractional charm content greatly

enhanced with respect to the generic high-E_T events written to tape. This filter is known as the "pair strip".

Every two-track combination among the set of silicon tracks which pass through the first magnet (and thus have measured momenta) is used to generate a secondary vertex. This vertex is required to have $\chi^2/dof < 5$ and $\sigma_{z\,sec} < 1.8$ mm. With the primary and secondary vertices established, two-track analogues of SDZ, PT2DK, and RAT are calculated. These variables are required to be greater than 6, greater than 0.1 GeV^2, and less than 0.06, respectively. Any event containing at least one pair passing all of these cuts passes the pair strip.

The pair strip, with a rejection factor of about 15, reduces the data set to 43 (partially-filled) tapes, corresponding to 29.9 million events.

5.4 Substrip

The pair strip data set is subjected to a further "substrip" filter. The substrip is comprised of three sets of cuts, each corresponding to a particular pseudoscalar D decay mode. Any event containing a triple which passes through one of these three gauntlets thereby passes the substrip.

In all that follows, triplets are formed from a set of tracks determined by the requirement that they have both silicon and drift chamber hits and pass through at least the first magnet. z_{pri} is constrained to be within the region containing the target foils and interaction scintillator ($-5.5 < z < 0.$ cm). In the target region, the z thickness of the foils ($\sim$100 μ for W, $\sim$250 μ for Be, Al, and Cu) is exploited to obtain a more precise (on average) determination of z_{pri}; the center of the target foil nearest the primary vertex as previously defined is taken to be z_{pri}. The error on z_{pri} is taken to be the RMS deviation of a flat distribution over the foil width, i.e., $\sigma_{RMS} = (z\,\text{width})/\sqrt{12}$. For cut variables that are calculated using z_{pri} (SDZ, DIP, and RAT), a "2" is added to the name of the variable if the modified z_{pri} (or its error) is used (e.g. SDZ2). Note that in the interaction scintillator region, no change is made to z_{pri}.

Decay mode dependent substrip cuts are listed in Table 5.1. In addition to these

cuts, any kaons within a given triplet are required to have a Čerenkov probability greater than 13%, higher than the *a priori* value of 12%; this essentially eliminates identified pions as candidate kaons. The relative charge signs of the kaons and pions within the triplet must be consistent with the decay being sought. Very loose quality cuts are placed on the vertices: $\chi^2/dof_{pri} < 3$ and $\chi^2/dof_{sec} < 5$. For each track in the triplet, $\chi^2/dof_{silicon}$ and χ^2/dof_{global} are required to be less than 10.

Cut variable	$D^+ \to K\pi\pi$	$D^0 \to K\pi$	$D_s \to KK\pi$
SDZ2	7	5	7
PT2DK (GeV^2)	—	0.3	—
DIP2 (μ)	100	150	100
RAT2	0.1	0.2	0.1

Table 5.1: Decay mode dependent substrip cuts. See text for a description of generic cuts.

About 3% of data events pass the substrip, coming in under the three decay modes in roughly equal amounts. The purpose of the substrip is simply to facilitate further analysis by obtaining a working data set which can fit on two or three tapes. The cuts are loose,[5] and the set of decay mode cuts under which a particular event passes is not "remembered" in subsequent analysis.

5.5 Cut optimization

For each decay mode studied, a set of optimal cuts is sought which maximizes signal significance.[6] When, for a particular analysis variable, the cut point is not narrowly indicated by significance, both cut efficiency and straight signal-over-background are weighed in deciding where to set the cut. Two measures of significance are examined:

[5]Despite the supposed looseness of the cuts, subsequent cut optimization (see Section 5.5) indicated that some cuts be kept at their substrip values.

[6]Significance is just the ratio of the number of signal events over the uncertainty in this number, given by the square root of the *total* number of events in the signal range, both signal and background.

the first uses MC signal and data background (where the former has been normalized to the latter), the second uses data signal and background. While the first measure does not suffer from statistical fluctuations in the data signal, it loses reliability when the MC and data distributions for a particular variable differ significantly in that variable's natural cut range. In such cases, the second measure is given precedence as long as it is smoothly-varying (i.e., statistical fluctuations are avoided).

As an example, in Fig. 5.1, the following variations versus the DIP2 cut value are shown for the $D^+ \to K\pi\pi$ mode:

(1) Significance #1: Ratio of normalized MC signal to square root of normalized MC signal plus data background

(2) Significance #2: Ratio of data signal to error on data signal (as returned by the fitter)

(3) "Cross-section": Ratio of data signal to MC signal, normalized to average around 1.0

(4) Signal-over-background: Ratio of normalized MC signal to data background

(5) Data signal

It should be noted that the errors indicated at each cut point are correlated.

For differential cross-sections, absolute normalization is not a concern, therefore making the choice of cuts less crucial than it is for the absolute cross-sections. In the latter analysis, however, it is important that the data/MC signal ratio remain stable (within statistics) over the appropriate range (i.e., from no cut to the optimal cut); this is an indication that the MC is modelling the distribution of a given variable in real data reliably. If this is not the case, the acceptance (see Section 7.1) returned by the MC cannot be trusted. As described in the following section, the DIP2 cut is set at different values in the forward and differential cross-section analyses for the $D^+ \to K\pi\pi$ and $D^0 \to K\pi$ modes. In these two cases, the ratio of data to MC signal (proportional to the cross-section) is rather sensitive to the value of the DIP2 cut, requiring that this cut be loosened to a value where this ratio more or less plateaus. For all other cut variables, the data/MC signal ratio is reasonably flat.

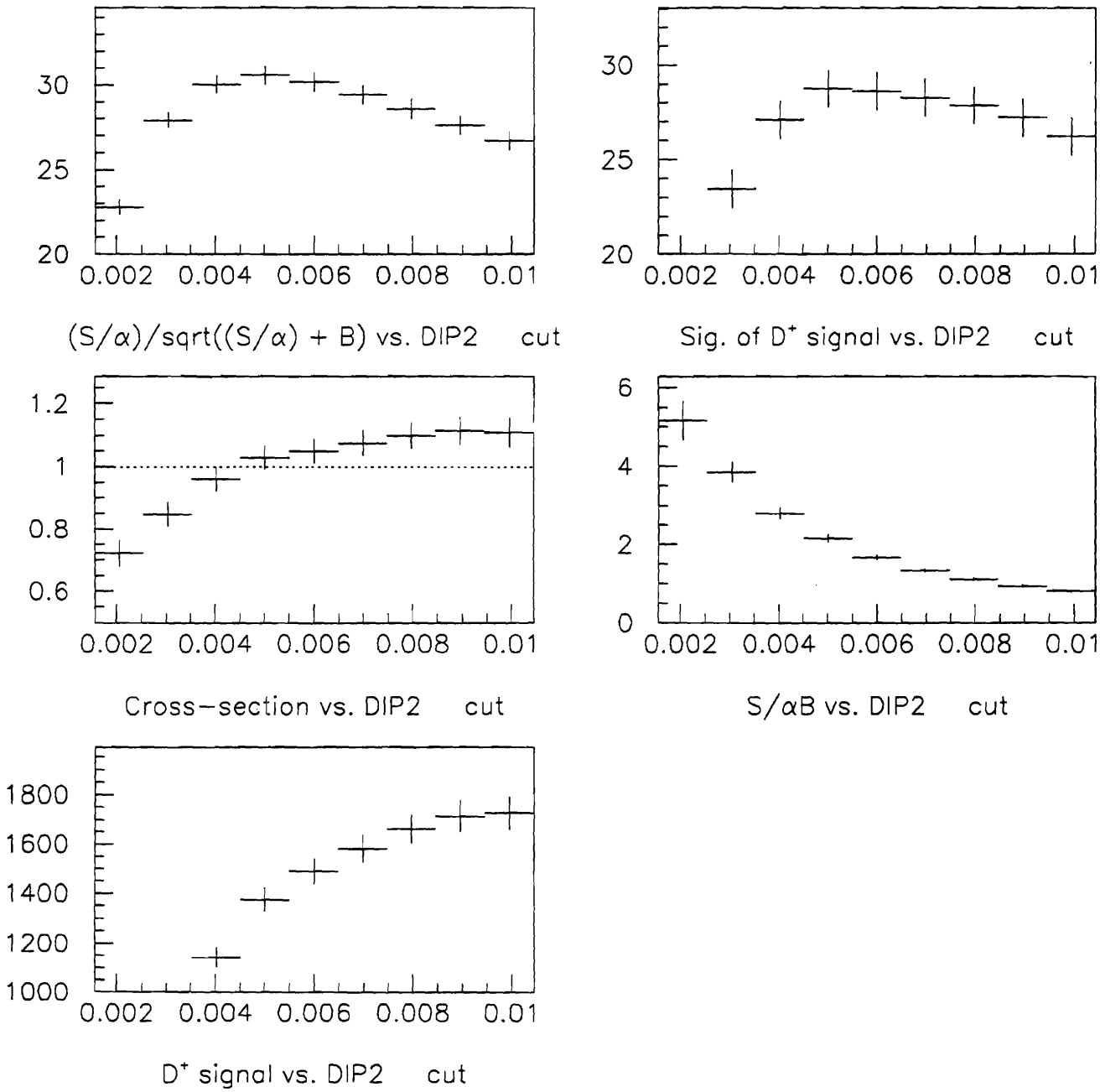

Figure 5.1: $D^+ \rightarrow K\pi\pi$ cut optimization: DIP2 (defined in Section 5.2. For all plots, DIP2 is measured in centimeters.

5.6 Final cuts

In selecting triplets as candidate decays, the same requirements specified in the substrip are placed on track and vertex quality, relative charge sign, Čerenkov probabilities for the kaon(s), and z location of the primary vertex. In Table 5.2, optimal cuts for the standard cut variables are listed for each decay mode. Recall that the $D^0 \to K\pi$ mode is used in the D^* analysis; these cuts are defined for the daughter D^0 in this case.

Cut variable	$D^+ \to K\pi\pi$	$D^0 \to K\pi$	$D^* \to D^0\pi$	$D_s \to \phi\pi$	$D_s \to K^*K$
SDZ2	13	10	9	10	13
PT2DK (GeV^2)	0.3	0.4	0.3	0.3	0.3
DIP2 (μ)	60[a]	60[a]	60	70	60
RAT2	.003	0.1	0.06	0.01	0.01
ISO (μ)	40	—	—	30	30

[a]Loosened to 100 μ in the forward cross-section analysis.

Table 5.2: Decay mode dependent final analysis cuts. See text for a description of cuts which are either generic or used specifically for a particular decay mode.

In addition to these cuts, certain cuts are applied to specific decay modes. For $D^+ \to K\pi\pi$, the product of SDZ2 and PT2DK is required to be greater than 15 GeV^2. For $D_s \to K^*K$, the absolute value of the cosine of the angle between the D_s and decay pion momenta (measured in the K^* center-of-mass frame) is required to be greater than 0.2.[7] For D_s decays to $\phi\,\pi$ (K^*K), the invariant mass[8] of the KK

[7]In the decay chain $D_s \to K^*K$, $K^* \to K\pi$, all particles are pseudoscalars (P), except for the K^*, which is a vector (V). In a P $\to$ VP decay, the V is longitudinally polarized. Therefore, if we boost from the rest frame of the parent P to that of the V, the products of a subsequent V $\to$ PP decay will have a $\cos^2\theta$ distribution, where θ is measured with respect to the boost direction.

[8]Invariant masses are calculated by assigning triplet members kaon or pion masses. Given the fact that only loose identification requirements are imposed, one triplet can be consistent with more than one scheme for assigning particle IDs; in these cases, such a triplet can account for more than one entry in an invariant mass plot. (All but the correct entry presumably contribute only to the background continuum.)

(relevant $K\pi$) pair is required to be within 10 (50) MeV of the ϕ (K^*) mass. In the D^* analysis, the invariant mass *difference* between the $K\pi$ pair and the triplet formed by adding the soft D^* decay pion is required to be within 10 MeV of the D^*-D^0 mass difference.

Once the set of all triplets passing the cuts for a given decay mode are found, the invariant masses of these triplets are histogrammed. Fits to these invariant mass distributions allow for the estimation of the number of decays observed in the E769 data set. The results of these fits are given in Chapter 6.

Chapter 6

Data

The E769 data set, comprised of approximately 400 million events written to tape at TPL during the 1987-88 Fermilab fixed target run, can be subdivided in a number of ways. First, the periodic structure of the secondary beams extracted from the primary 800 GeV p beam (i.e., spills of 22 second duration coming once every 60 seconds) provides the smallest unit into which events are grouped. Some variable number of spills (typically several hundred) are grouped into a larger unit called a "run", corresponding to a period of continuous data-taking under relatively uniform running conditions. About 2000 runs of data were taken during the experiment. Runs conducted under grossly similar running conditions are further grouped into "run regions", of which there are four (hereafter called "Regions 1-4").

During the first (second) half of E769, the mixed hadron beam was negatively (positively) charged. Regions 1 and 2 comprise the first half, 3 and 4 the second. During Region 1, the experiment ran at a beam energy of 210 GeV; in the subsequent three run regions, the beam was at 250 GeV. Within the positive running, the two run regions distinguish between the most characteristic DISC settings used during these periods. In Region 3, the DISC was typically set to identify kaons (also the case for the negative running); the DISC was set to identify protons in Region 4. Now that the run regions have been defined "historically", we will from now on refer to experimental conditions characterizing a particular spill, run, or run region in the present tense.

Once the data set has been broken down on the basis of running conditions, we further divide it into subsets on the basis of the identity of the beam particle[1] and the trigger type(s) under which the events were written to tape. These two criteria are interrelated through the inclusion of the DISC in the trigger logic. For the forward cross-section analysis, we require isolation of event subsets for each beam particle/beam energy combination present in the data. The trigger type(s) included in these subsets must be specified in order that absolute normalizations can be determined. These data subsets are defined in Section 6.2. For the differential cross-section analysis, the data sets used are largely the same, the main difference being that 210 and 250 GeV beam energy subsets are combined.

The analysis described in Chapter 5 is performed on these subsets for each D meson decay mode, resulting in the further subdivision of each subset into smaller event subsets, which in this case however are not disjoint. In some cases, subsets are then recombined when the resulting "composite" cross-sections retain some fundamental character (e.g., combining π^- and π^+ beam subsets). Signals for different D modes are also combined in the differential cross-section analysis. Motivations and justifications for such combinations of "initial-state" and "final-state" subsets are given in relevant sections of Chapters 8 and 9.

6.1 Event weeding

The data subsets used in both the forward and differential cross-section analyses undergo a "weeding" process whereby events are thrown out. In both analyses duplicate events are removed; this is "simple-weeding". For the forward cross-section calculations, absolutely normalized beam particle fluxes are obtained using scaler events. About 5% of events, however, are in spills for which the corresponding scaler event is missing, therefore rendering them unnormalizable. Another 3-5% of events are from spills or runs that are pathological in some way which makes their use suspect. For example, certain spills have incorrect NSPILL numbers which make them impossible

[1]As detailed in Section 3.2, a beam particle is considered positively identified if the probability that the tag is correct is at least 90%.

to associate with the correct scaler event. Some spills are thrown out for reasons other than pure bookkeeping; nonsensical average track multiplicities or DC efficiencies are examples of grounds for such disposal. Removal of events for the above reasons is called "full-weeding".

A small fraction of the time, scaler events indicate zero recorded flux for spills for which there are data events. Rather than throw out these events from anomalously-empty spills, flux correction factors χ_{empty} (see Section 8.1) are calculated by the following procedure: the ratio of the number of data events passing loose analysis cuts before and after removal of these "empty-spill" events is taken to be the ratio of the corresponding beam particle fluxes. The resulting factors are given in Table 6.1.

Data subset(s)	χ_{empty}
π^-,K^-; 210 GeV	0.982
π^-,K^-; 250 GeV	0.972
π^+,K^+	0.997
p	0.998

Table 6.1: "Empty-spill" flux correction factors.

6.2 Data subsets

The initial-state data subsets used in the forward cross-section analysis are tabulated in Table 6.2. For each beam energy/beam particle combination, the corresponding run region(s), trigger combination, and identified live beam particle flux (defined in Section 8.1) are given. Individual trigger types are defined in Section 3.5. Note that the proton beam subset consists of both the run region 3 and 4 components listed. Systematic errors associated with the flux totals are discussed in Section 8.2.3.

Beam particle	Beam energy (GeV)	Run region(s)	Trigger(s)	Identified live flux
π^-	210	1	ETπ+ETB	1.35×10^{10}
	250	2	ETπ+ETB	6.52×10^{10}
K^-	210	1	ETK	5.50×10^{8}
	250	2	ETK	1.67×10^{9}
π^+	250	3	ETπ+ETB+ETe	1.17×10^{11}
K^+	250	3	ETK	5.42×10^{9}
p	250	3	ETπ+ETB+ETe	5.99×10^{10}
		4	ETK	2.50×10^{9}

Table 6.2: E769 initial-state data subsets (absolute cross-section analysis).

6.3 Data signals

In general, the procedure for determining data signals is to perform (using FORTRAN-driven MINUIT) a log-likelihood fit, where the fit function is a bin-wise (10 MeV bin width) integration of a Gaussian over a background which is either flat or, in cases where a flat background does not provide a reasonable fit, linear. Masses are fixed at 94 PDG values. The width is fixed to the value returned by a fit of the total simply-weeded data signal, typically 1.5-2.5 MeV greater than that of the corresponding MC signal. These widths and masses are compiled in Table 6.3. In fitting relatively low-statistics signals (i.e., signals binned in x_F and p_T^2), the aforementioned procedure is modified, as described in Sections 6.3.1 and 6.3.2.

In Figs. 6.1 through 6.6, fitted invariant mass plots for each D mode are shown, including both the total signal (before any beam identification cuts are imposed) and its components broken down by beam particle; the resulting signal estimates, used in the forward cross-section calculations, are also given. Once events for which positive beam particle identification is impossible (~25%) are discarded, the data subsets for each D mode are made up of the following approximate beam particle fractions: 49% π^-, 17% π^+, 5% K^-, 13% K^+, and 16% p. The final event totals used in the forward

Decay mode	width (MeV)	mass (MeV)
$D^+ \to K\pi\pi$	11.0 ± 0.5	1869.4 ± 0.4
$D^0 \to K\pi$	12.9 ± 0.7	1864.6 ± 0.5
$D^* \to D^0\pi$	12.4 ± 1.1	2010.0 ± 0.5
$D_s \to KK\pi$	10.8 ± 1.1	1968.5 ± 0.7
Combined D	11.5 ± 0.4	—

Table 6.3: Data signal widths and (94 PDG) masses.

cross-section analysis are 994 ± 47 D^+, 847 ± 55 D^0, 100 ± 15 D_s, and 209 ± 19 D^*. As indicated above, the event totals used in the differential cross-section analysis are about 8% larger.

Note that in one case ($D^0 \to K\pi$, p beam), a linear background is not sufficient to give a reasonable fit to the invariant mass plot. Using a quadratic background goes too far the other way, resulting in a signal estimate which is unreasonably small. The compromise solution used is to fit the signal using a linear background over a more limited range (1.77-1.97 GeV); this fit (the one shown in Fig. 6.4) results in a signal estimate close to the average of those of the two aforementioned fits.

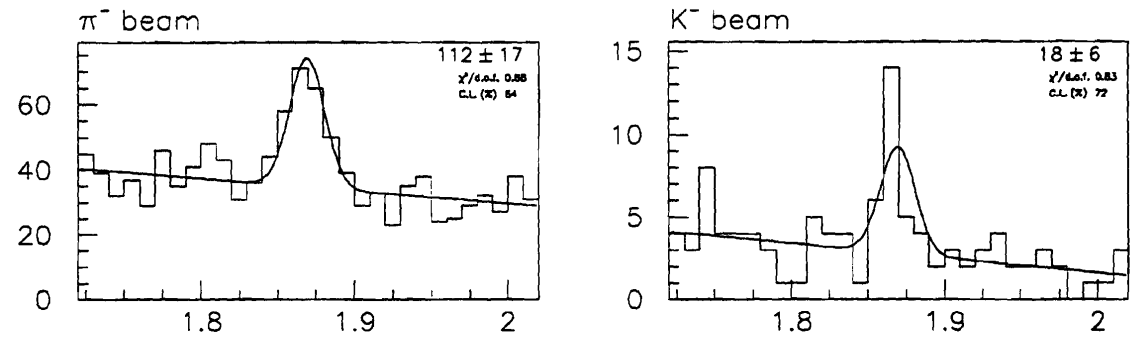

Figure 6.1: $D^+ \rightarrow K\pi\pi$ events vs. invariant mass (GeV), full-weeding, $x_F > 0$, 210 GeV beam.

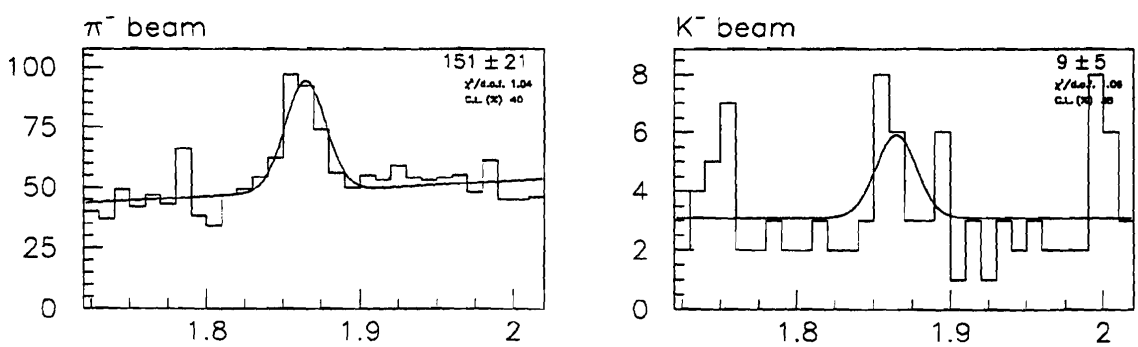

Figure 6.2: $D^0 \rightarrow K\pi$ events vs. invariant mass (GeV), full-weeding, $x_F > 0$, 210 GeV beam.

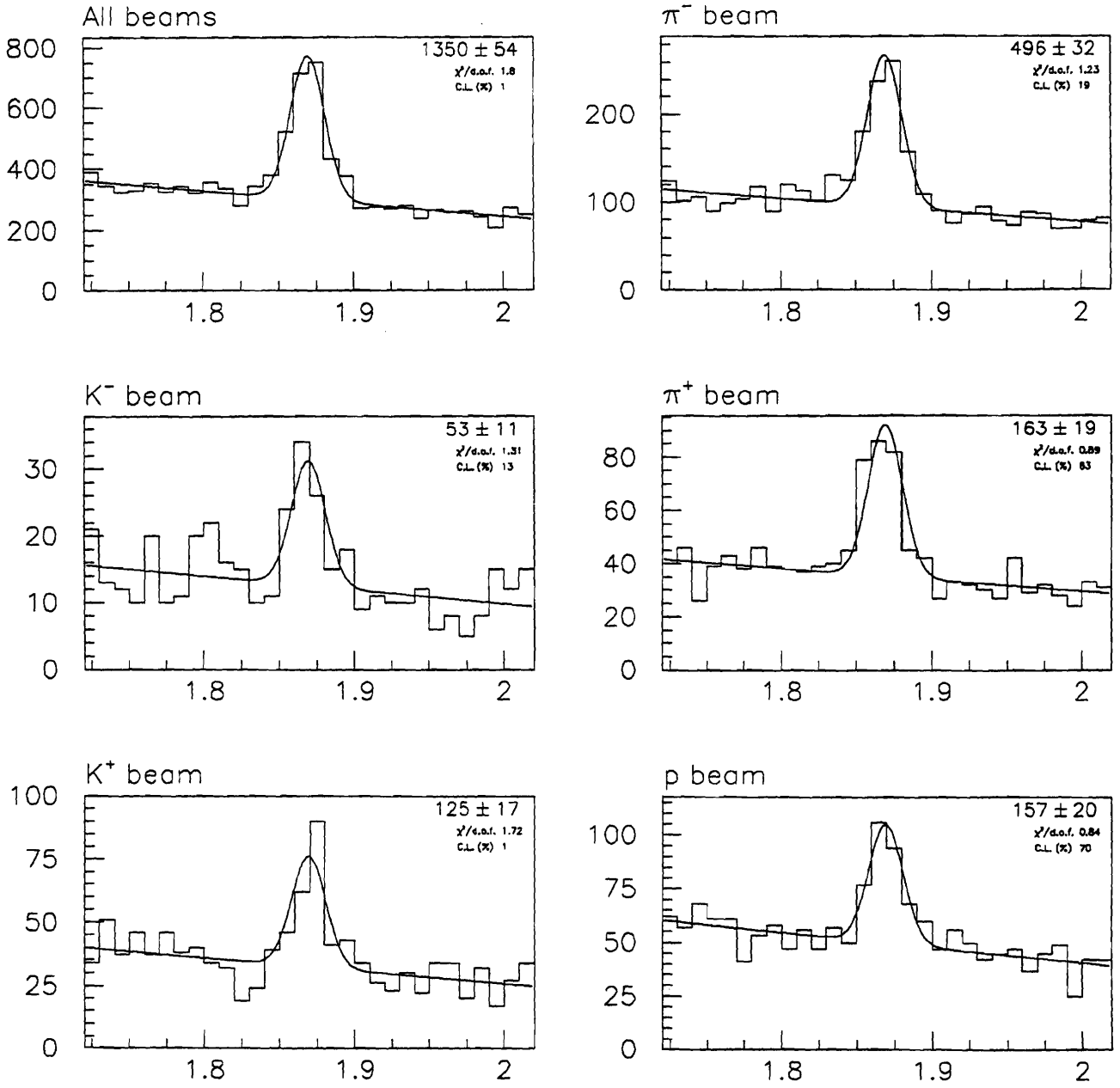

Figure 6.3: $D^+ \to K\pi\pi$ events vs. invariant mass (GeV), full-weeding, $x_F > 0$, 250 GeV beam.

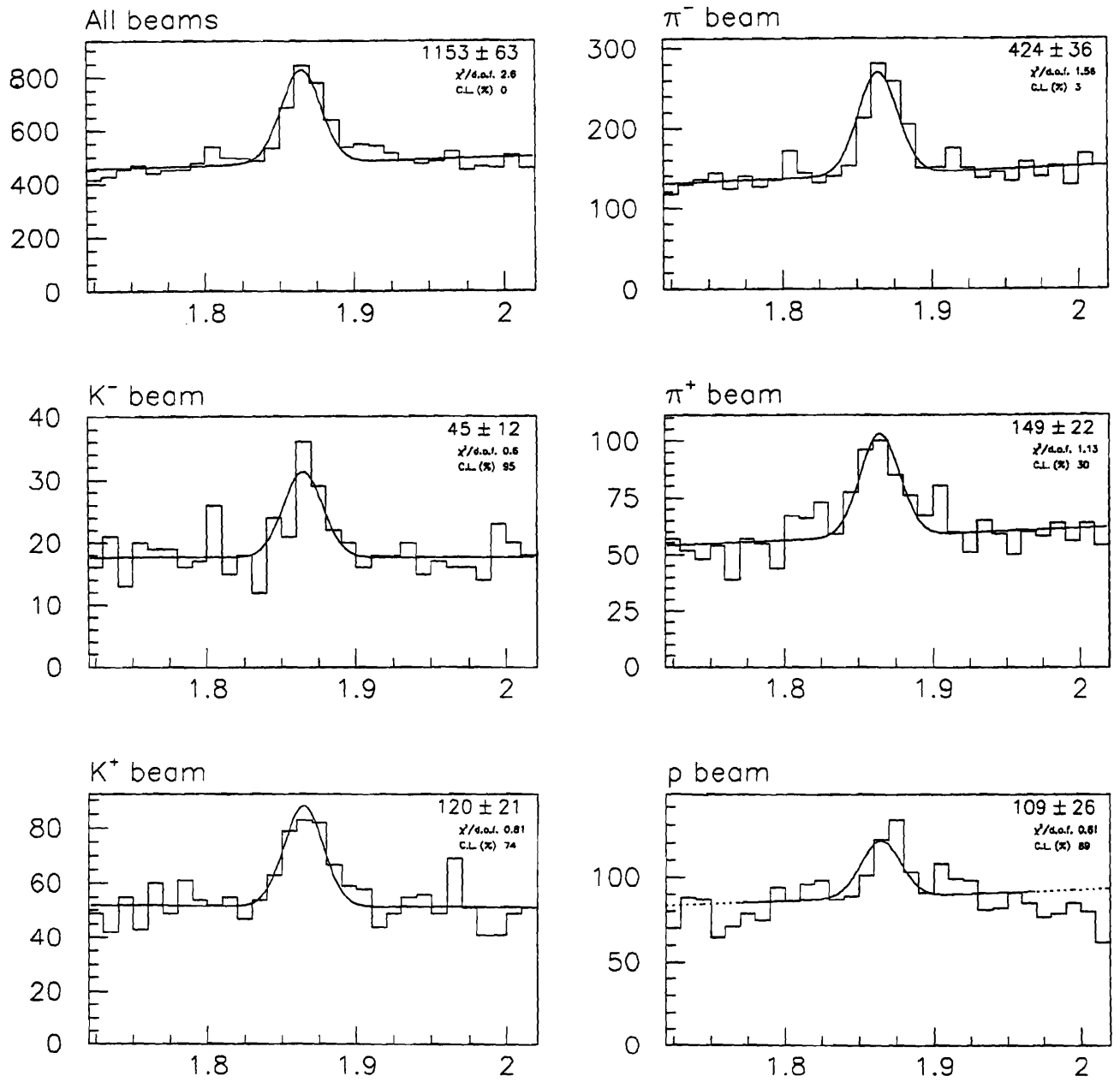

Figure 6.4: $D^0 \rightarrow K\pi$ events vs. invariant mass (GeV), full-weeding, $x_F > 0$, 250 GeV beam.

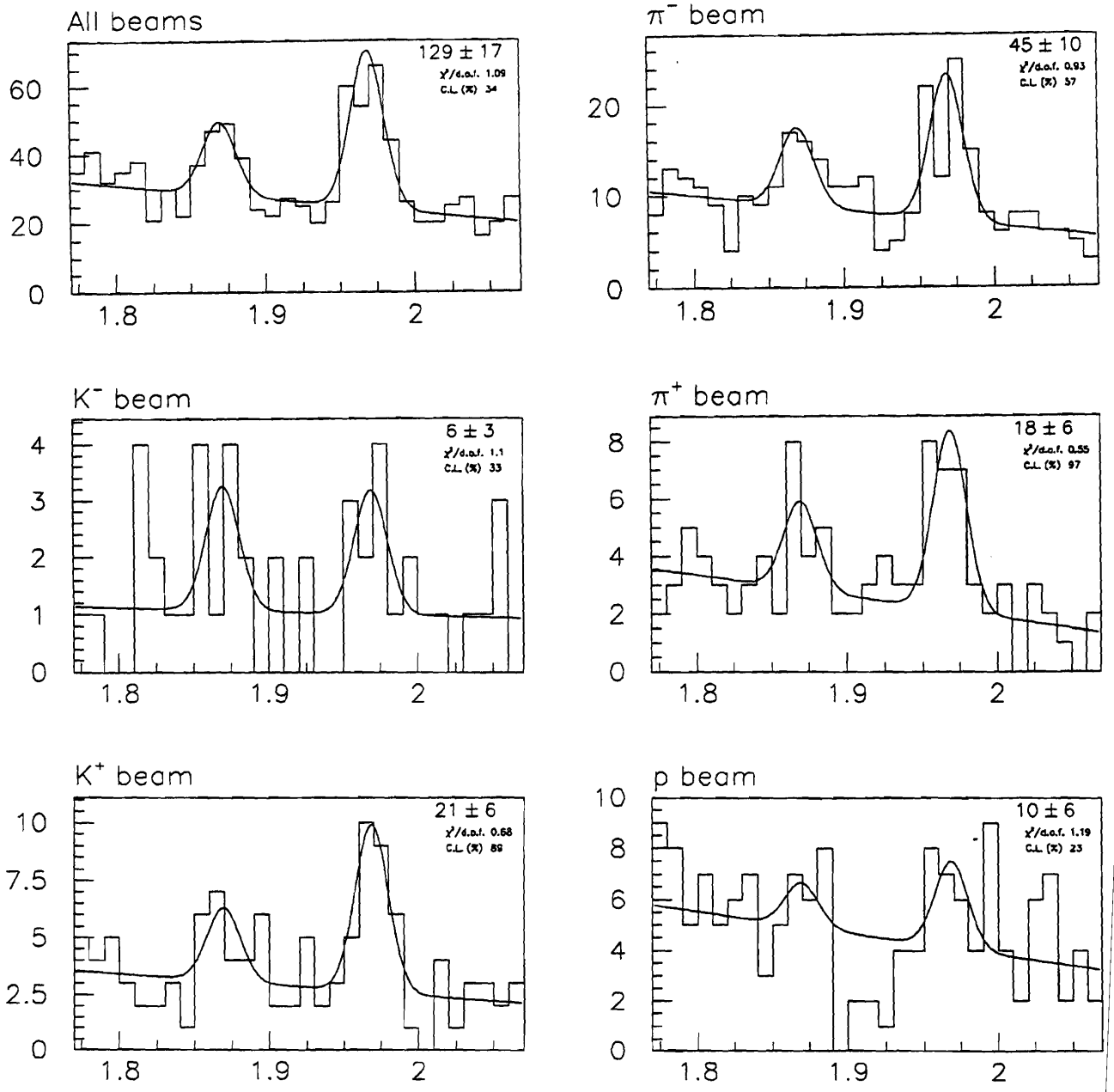

Figure 6.5: D^+ (left peak), D_s (right peak) $\rightarrow KK\pi$ events vs. invariant mass (GeV), full-weeding, $x_F > 0$, 250 GeV beam. The D^+ mode is Cabibbo suppressed.

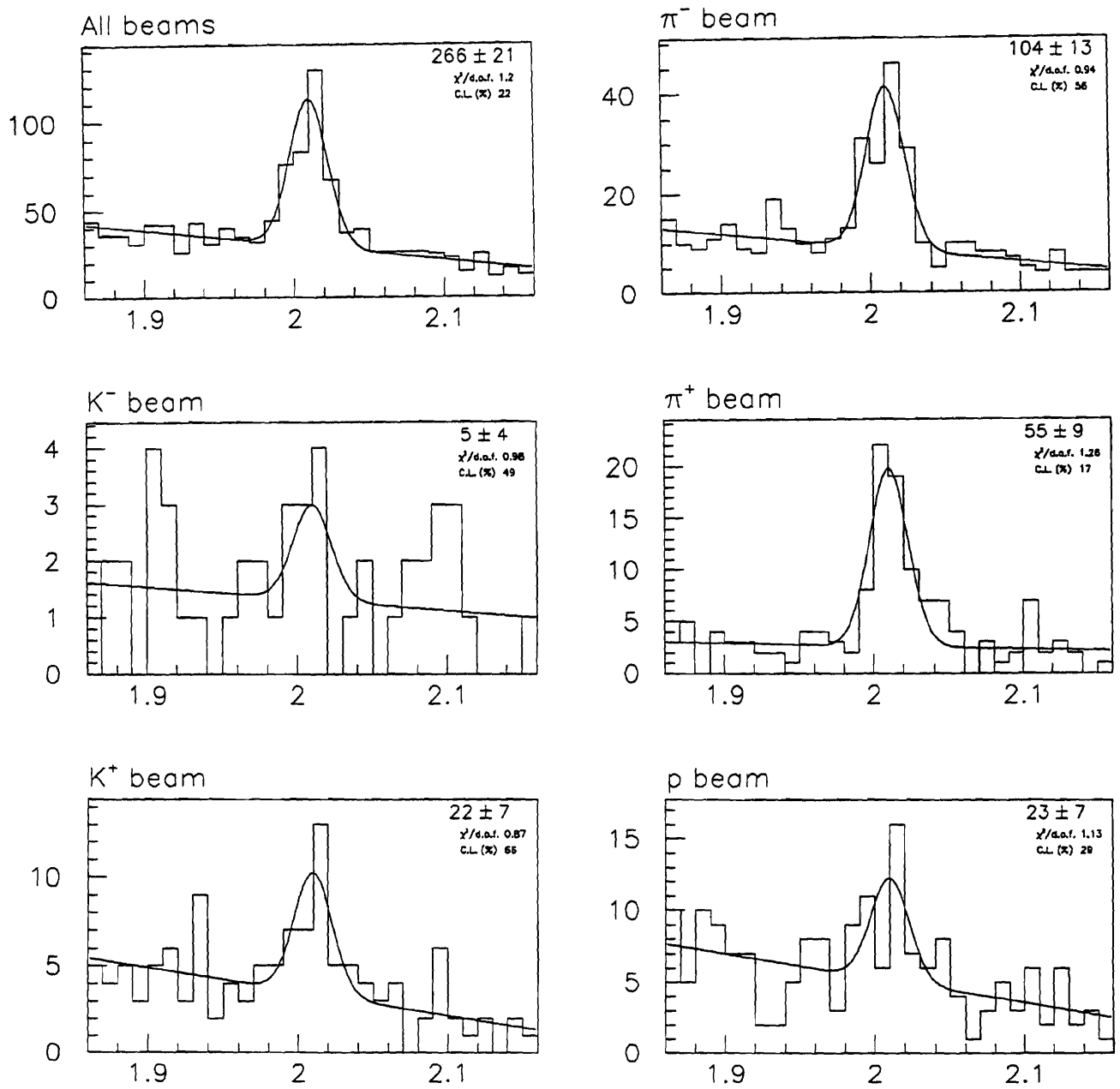

Figure 6.6: $D^* \to D^0\pi$ events vs. invariant mass (GeV), full-weeding, $x_F > 0$, 250 GeV beam.

6.3.1 Data signals vs. x_F

In fitting data signals, the x_F dependence of the signal widths is taken from the MC (see Section 7.3.1). An offset corresponding to the difference in the data and MC signal widths is added to the width versus x_F function, which is then used to obtain the values to which the widths are fixed during fitting. The constancy of signal mass versus x_F was checked in the D^+ and D^0 data; no indication of any x_F dependence is found (see Fig. 6.7).

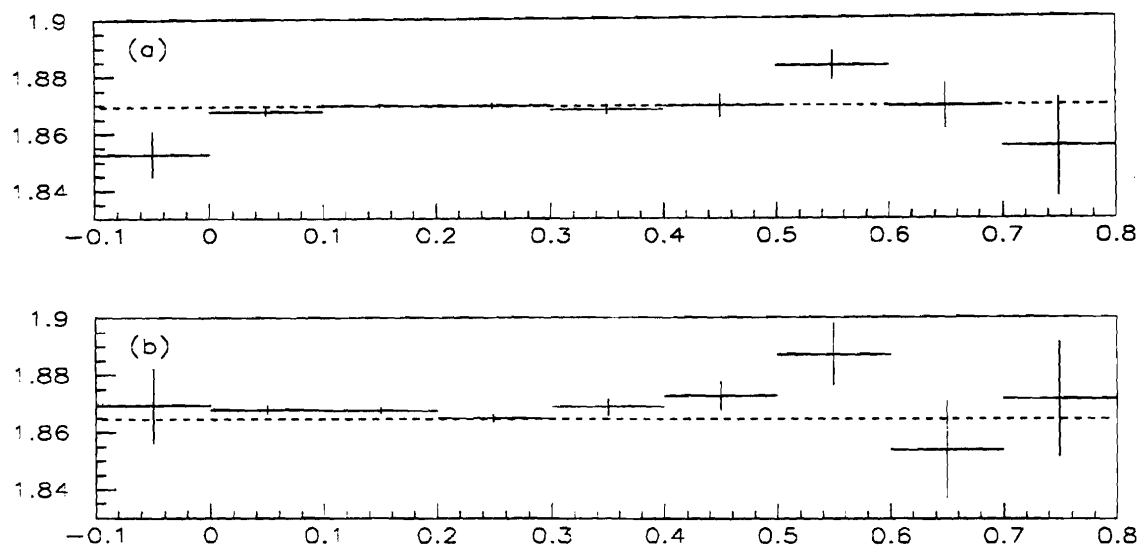

Figure 6.7: Data signal mass (GeV) vs. x_F for (a) $D^+ \to K\pi\pi$, π beam, and (b) $D^0 \to K\pi$, π beam. The dotted lines indicate the 94 PDG mass values.

As described in Chapter 9, differential cross-section results are obtained for a "combined D" sample comprised of the three pseudoscalar mesons D^+, D^0, and D_s; these species make up approximately 50%, 40-45%, and 5-10% of the combined D signals, respectively. Fits to the π^- beam combined D signals versus x_F, the highest-statistics representative of data signals thus broken down, are presented in Fig. 6.8.

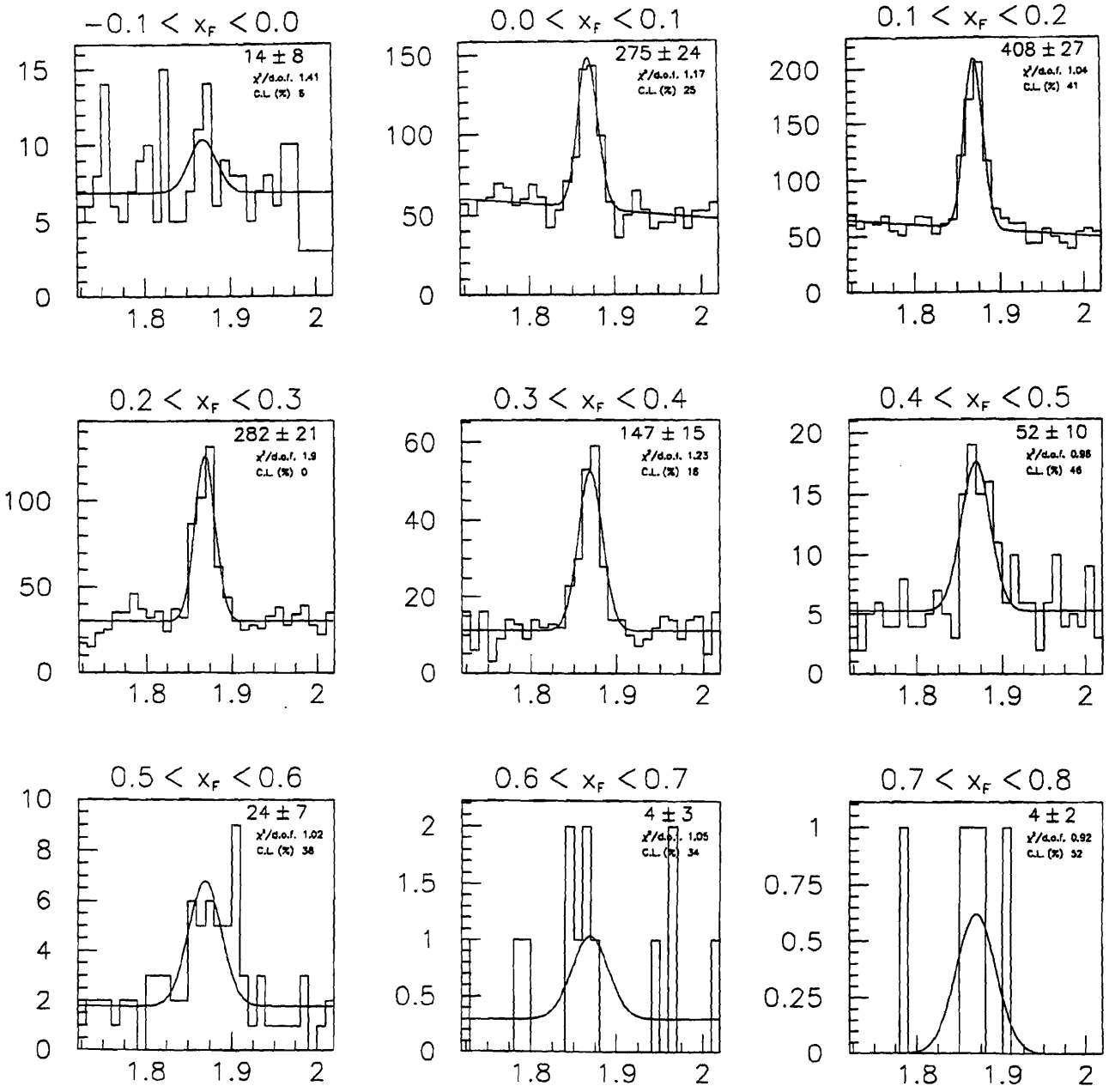

Figure 6.8: Combined D events vs. invariant mass (GeV), simple-weeding, π^- beam.

6.3.2 Data signals vs. p_T^2

In binning the data signals in p_T^2, it was found, owing to the exponential decrease in cross-section with rising p_T^2, that use of a single binwidth was incompatible with maintaining both sampling granularity and signal significance over the entire range for which data was available. Therefore, two binwidths, 1 and 2 GeV^2, are used for low and high p_T^2 respectively, the boundary between the two regions being determined on a case-by-case basis according to where the signals drop below the threshold of significance (2σ) used in fitting the differential distributions. This boundary ranges from 4 to 8 GeV^2. Once the binning for a particular mode/beam is chosen, it is used in all phases of the p_T^2 analysis. Fits to combined D signals versus p_T^2 are shown in Fig. 6.9.

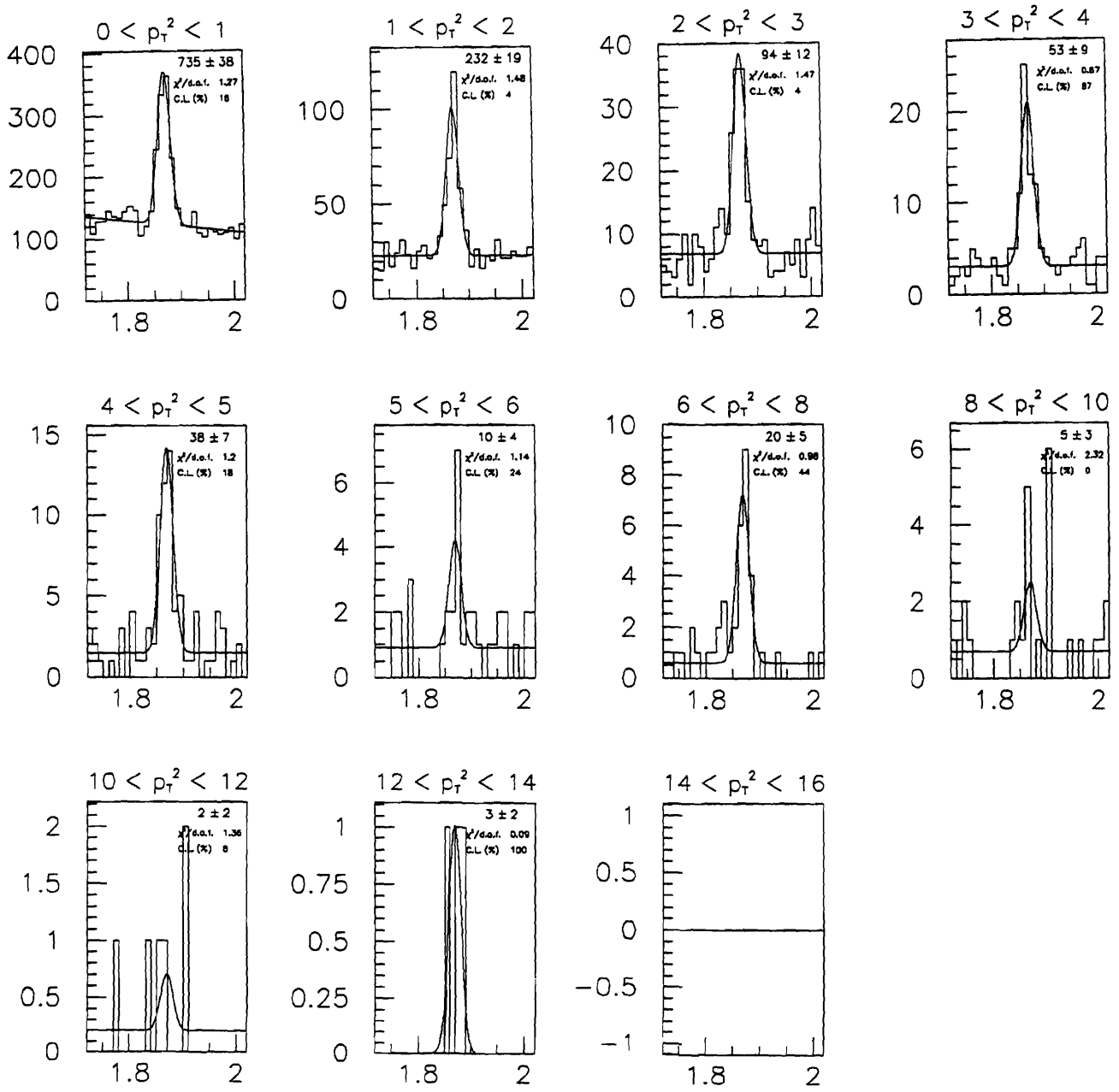

Figure 6.9: Combined D events vs. invariant mass (GeV), simple-weeding, $x_F > 0$, π^- beam.

Chapter 7

Acceptance

7.1 Definition and calculation

Acceptance is a ratio of decays detected to decays present; it is an efficiency or probability for a physical state to satisfy requirements (some of them purely stochastic) that allow for a positive measurement to be made. In the context of this analysis, this physical event is a charm meson decay $D \rightarrow xyz$ ($x_F > 0$), where the two to three charged decay products are comprised of pions and at least one kaon. A "positive measurement" of such an event has many components.

First, the event must have been written to tape. This requirement entails two efficiencies, ϵ_{live} and ϵ_{trig}, the first being the detector livetime and the second being the efficiency for the event to pass a particular set of trigger requirements (labelled T). As detailed in Section 8.1, ϵ_{live} is included in the "live flux" component of the absolute cross-section calculation and therefore does not concern us here.[1]

Once an event is written to tape, detection depends on a multitude of interrelated factors: track reconstruction in the SMD and drift chambers; track matching between different regions of the spectrometer, allowing for momentum determination; Čerenkov identification of the kaon(s); and association of the tracks into primary and secondary vertices. Unlike the inherently binary selection criteria mentioned in

[1] Another factor which does not come into our definition of acceptance is beam-tagging efficiency. As shown in the calculation of Section 8.1, this efficiency either cancels out or is included in the flux calculation.

the previous paragraph, success in any of these processes is typically quantified in terms of one or more continuous variables.[2] For example, a track returned by the track-reconstruction algorithm (which takes as its inputs SMD and DC hits) will be associated with a value of the statistical measure χ^2. Whether or not this track is deemed "good" (i.e., determines with sufficient precision the direction and location of a physical particle trajectory) will depend on whether its χ^2 falls above or below some cutoff. This and similar cutoffs (the so-called "analysis cuts") are chosen to optimize particle detection, not by maximixing the overall efficiency but by maximizing the expected statistical significance of the measured physical parameters. This process is described in Section 5.5.

The average efficiency for a decay $D \to xyz$ to pass all analysis cuts will be called ϵ_{geom}, where the subscript gives the somewhat misleading impression that this efficiency is simply a function of the interrelated geometries of the particle decay and spectrometer. In fact, ϵ_{geom} is a complex convolution of these geometrical dependencies with the efficiencies of each component of the detector, the details of the tracking and vertexing algorithms, and the values of the final analysis cuts. An analytic calculation of ϵ_{geom} would be exceedingly difficult to perform, so we rely upon numerical methods, namely the Monte Carlo simulation of the experiment detailed in Chapter 4.

Acceptance is given by the following expression:

$$Acc(T, D \to xyz) = \epsilon_{geom}(D \to xyz)\ \epsilon_{trig}(T, D \to xyz) = \frac{\hat{N}^{MC}_{obs}(T, D \to xyz)}{N^{MC}_{gen}(D \to xyz)}, \tag{7.1}$$

where

$\hat{N}^{MC}_{obs}(T, D \to xyz)$ = number of *weighted* MC D's ($x_F > 0$) observed through invariant mass reconstruction of decay $D \to xyz$, and

$N^{MC}_{gen}(D \to xyz)$ = number of generated MC D's ($x_F > 0$) decaying to xyz.

By weighting Monte Carlo events, we're able to include efficiencies or corrections to the simulation without changing the code. The above definition of acceptance is also

[2] Ultimately, these continuous variables are derived statistically from sets of binary physical events, such as whether an SMD strip registered a hit or whether a phototube fired.

valid for the differential analysis, except that both $\hat{N}_{obs}^{MC}$ and N_{gen}^{MC} are binned in x_F or p_T^2 in order to determine acceptance as a function of these variables. In both differential and absolute cross-section analyses, the trigger efficiency is added through a weighting function. In the differential analysis, a Čerenkov efficiency correction is implemented. In the absolute analysis, corrections to the differential and lifetime distributions and drift chamber efficiencies are used. These weighting functions and factors are described in the following section.

7.2 Monte Carlo weighting

7.2.1 Trigger efficiency

As detailed in Section 6.2, different trigger combinations make up the data signals for each of E769's five beam particle types. The efficiency of each of these triggers has a transverse energy (E_T) dependence which must be modelled in the MC in order to obtain the trigger efficiency ϵ_{trig} for events containing a particular charm decay. This E_T dependence changes with run number, as both the trigger thresholds and trigger prescalers (which affect the relative fractions of each trigger in a given signal) were adjusted from time to time as the experiment progressed.

The E_T dependence of the efficiency of a particular combination of triggers over a certain run region is determined by measuring it directly using a set of about 1.2 million interaction triggers. The interaction trigger, once the effect of its (changing) prescaler has been removed, is taken to have an efficiency of 100% for charm. Rather than looking at calorimeter output directly (which would have to be modelled well in the MC), a measure of E_T called $p_T(7,15)$ is used. For a given event, $p_T(7,15)$ is the summed transverse momenta of all JCATSG[3] 7 and 15 charged tracks which pass a few loose cuts on track quality.

It has been determined that the $p_T(7,15)$ dependence of all E769 trigger efficiencies is well-parametrized by the following function:

[3]The variable JCATSG is defined in the footnote on pg. 36.

$$\epsilon_{trig}(p_T(7,15)) = P_1 - \frac{P_2}{1+\exp(\frac{p_T(7,15)-P_3}{P_4})} \tag{7.2}$$

P_1-P_4 are parameters determined by a fit of efficiency versus $p_T(7,15)$. For the trigger combinations/run regions used in this analysis, these parameters are listed in Table 7.1. The parameter P_1 is the value to which the trigger efficiency function plateaus at high $p_T(7,15)$; we expect this to be 100% in the absence of prescaling.[4] For charm events, if the efficiency due to prescaling is removed, the remaining efficiencies due to the low and high-E_T thresholds are approximately 75% (90%) and 10% (20%), respectively, during the negative (positive) running.

In Fig. 7.1, a fit to interaction trigger data is shown; the shape of the ϵ_{trig} dependence on $p_T(7,15)$ seen here is typical. Since this dependence is non-linear, these parametrization functions are used to weight the MC on an event-by-event basis rather than to obtain trigger efficiencies from average values of $p_T(7,15)$.

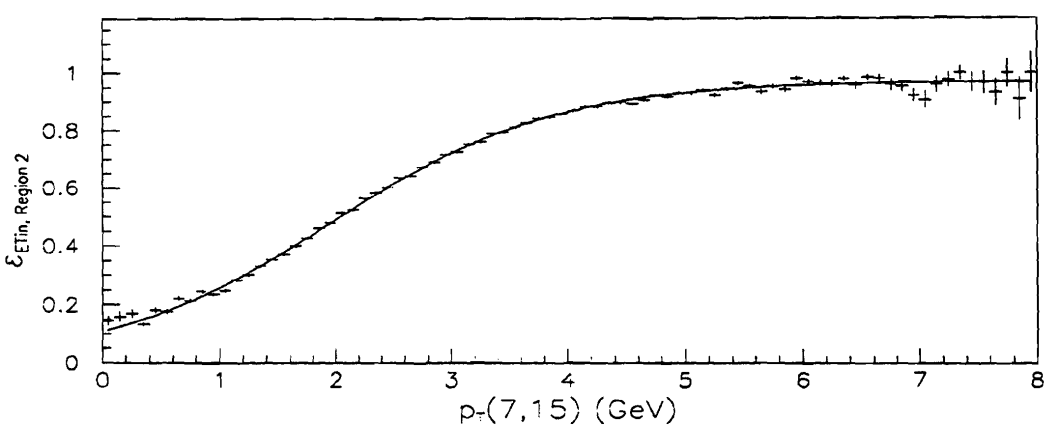

Figure 7.1: Trigger efficiency $\epsilon_{\mathrm{ETin,Region2}}$ vs. $p_T(7,15)$ (GeV).

Note that to model the average trigger efficiency in p beam data, a flux-weighted

[4]Trigger efficiency function parameters are determined from fits over the $p_T(7,15)$ range 0-8 GeV. The high-E_T threshold was set above this range; therefore, for trigger combinations which include this requirement in their logic, ϵ_{trig} does not turn over and reach a plateau value in a $p_T(7,15)$ range with a significant amount of data. In these cases, P_1 should not be taken as a reliable estimate of the average inverse prescale setting.

Trigger(s)	Run region	P_1[a]	P_2	P_3 (GeV)	P_4 (GeV)
ETπ+ETB	1	.519 ± .017	.50 ± .04	2.28 ± .07	1.08 ± .10
	2	.324 ± .013	.37 ± .02	2.90 ± .08	1.83 ± .12
ETin[b]	1	.954 ± .007	.88 ± .03	1.92 ± .05	.95 ± .04
	2	.973 ± .002	.976 ± .012	1.98 ± .02	.965 ± .014
ETπ+ETB+ETe	3	.160 ± .014	.163 ± .016	4.3 ± .2	1.52 ± .13
ETin	3	.9996 ± .0010	.770 ± .011	1.73 ± .03	.824 ± .011
ETin	4	.999 ± .005	.78 ± .05	1.71 ± .10	.83 ± .05

[a]In the differential cross-section analysis, weighting functions are multiplied by factors which lift their plateau values P_1 up to 100% (if they're not there already). The normalization is corrected at the end of the analysis using results from the absolute cross-section analysis.

[b]The efficiency of the ETin requirement (defined in Section 3.5) is used to model the efficiency of ETK triggers, thereby eliminating the contribution of the DISC efficiency to the latter. This efficiency cancels out in the cross-section calculation, as described in Section 8.1.

Table 7.1: Trigger efficiency weighting function parameters.

sum of trigger efficiency functions, corresponding to the two independent trigger sets in this sample (ETπ+ETB+ETe in Region 3 and ETK in Region 4), is used. In the differential cross-section analysis, 210 and 250 GeV data is combined in the π^- and K^- samples; combined Region 1 and 2 trigger efficiency functions are therefore used to weight the MC.

7.2.2 Čerenkov efficiency

This analysis relies on identification of charged secondary kaons by the two threshold Čerenkov detectors in the E769 spectrometer. The efficiency for this identification $\epsilon_{\check{C}(K)}$ is dependent upon the kaon momentum p_K. There is reason to doubt (on first principles), however, that the MC simulation of the Čerenkov counters is sophisticated enough to return a value for this efficiency accurate to within the precision afforded by MC statistics. A previous E769 graduate student therefore measured the dependence of $\epsilon_{\check{C}(K)}$ on p_K directly using $D^+ \to K\pi\pi$ data. In bins of p_K, D^+ signals were

obtained with and without a cut on the Čerenkov probability of the kaon. The ratio of these signals gives an average value of $\epsilon_{\check{C}(K)}$ over a given range of p_K. The ratios of these data-determined efficiencies to their MC-determined counterparts provide a weighting function with which to correct the MC. A comparison of data and MC values of $\epsilon_{\check{C}(K)}$ is shown in Fig. 7.2.

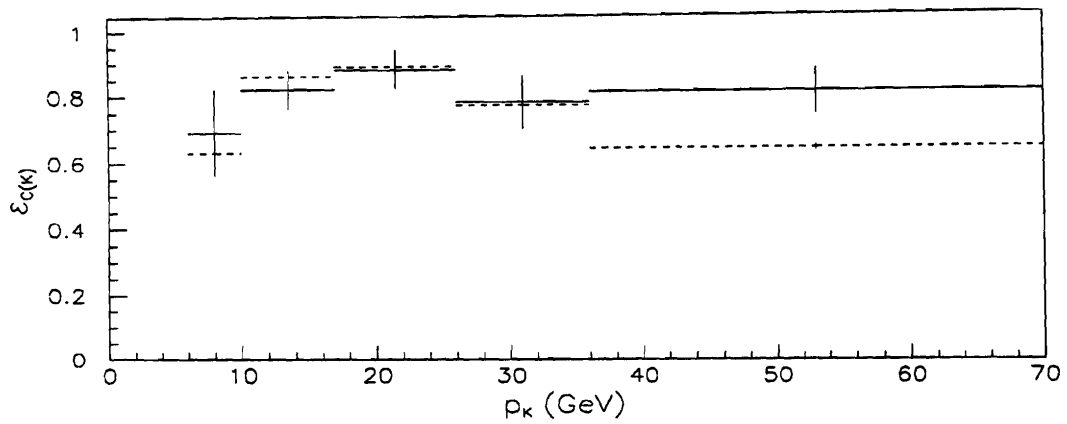

Figure 7.2: Čerenkov efficiency for K identification vs. p_K (GeV) from $D^+ \to K\pi\pi$ data (solid) and MC (dashed).

As can be seen from the plot, on the basis of this data alone (which is statistics-limited), there is no compelling evidence that any correction is indicated. It was decided, therefore, that *no* Čerenkov correction to the MC would be made in the absolute cross-section analysis.[5] Due to the lingering uncertainty in $\epsilon_{\check{C}(K)}$, however, the precision of the aforementioned determination from data (which is the best information we have) is used as the measure of this contribution to the systematic uncertainty in the acceptance (see Section 8.2).

[5]At the time of this decision, the differential cross-section analysis had already been completed using the Čerenkov correction to weight the MC (once for each kaon among the decay products of a given mode) on an event-by-event basis. The effect of this weighting on the differential acceptances, however, is not significant.

7.2.3 Differential distributions

The acceptance for a particle D is a function of its momentum; due to the effective azimuthal symmetry of the spectrometer about the beam axis, it is reasonable to split this dependence into uncorrelated x_F and p_T^2 parts. We rely upon the MC simulation of the D event in determining acceptance, both in the absolute and differential cross-section analyses. In the latter, however, data and MC signals are binned in x_F and p_T^2 with sufficient fineness (given the observed variation of acceptance with the production variables) to ensure that results are insensitive to the x_F and p_T^2 distributions generated for the D in the MC. This allows us to obtain differential cross-section results without making any assumptions about the distributions we expect (except perhaps that the real and MC-generated production distributions are qualitatively similar). These results in turn are used in the absolute cross-section analysis; MC events are weighted in both x_F and p_T^2 in order to force the MC distributions in these variables to conform to measured results.

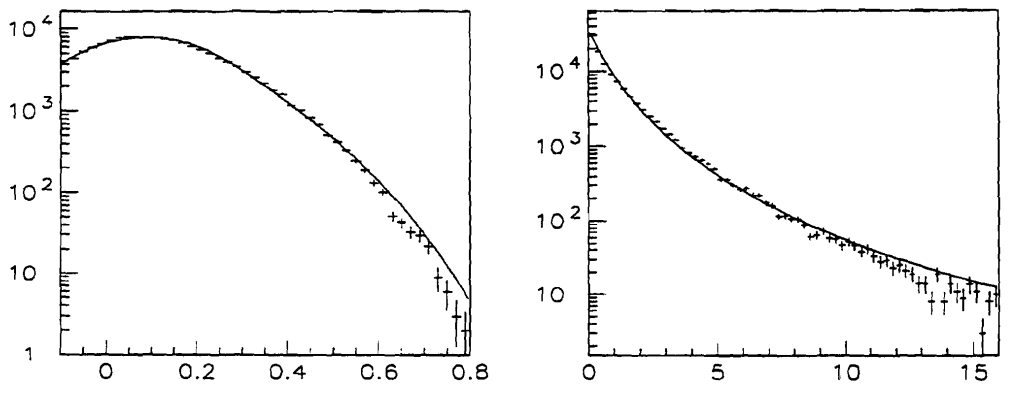

Figure 7.3: Number of generated D^+ events vs. x_F (left) and p_T^2 (GeV^2) (right).

As described in detail in Section 9.3.3, for a given beam, combined D differential cross-sections are found to be consistent[6] with each of the distributions for D^+, D^0, and D_s taken separately. In addition, positive and negative-beam components of

[6]See Section 9.3.2 for a precise definition of "consistency" as it relates to two measured distributions.

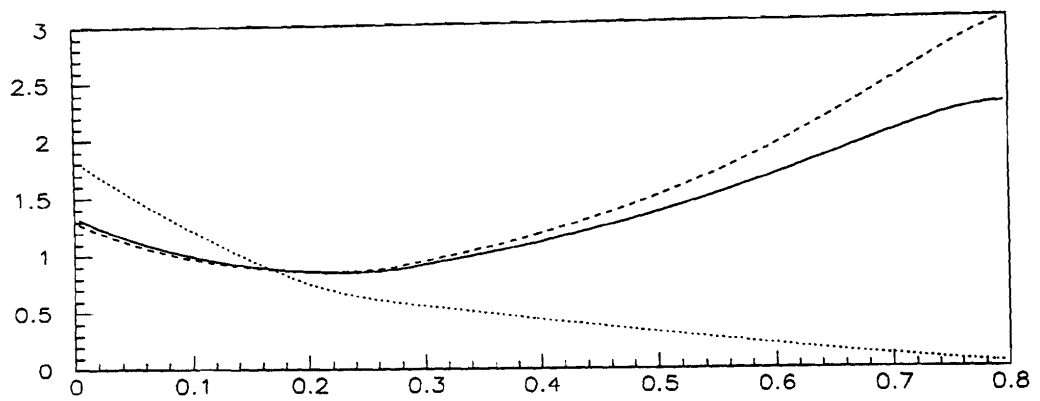

Figure 7.4: D^+ production distribution correction vs. x_F, for π (solid), K (dashed), and p (dotted) beams.

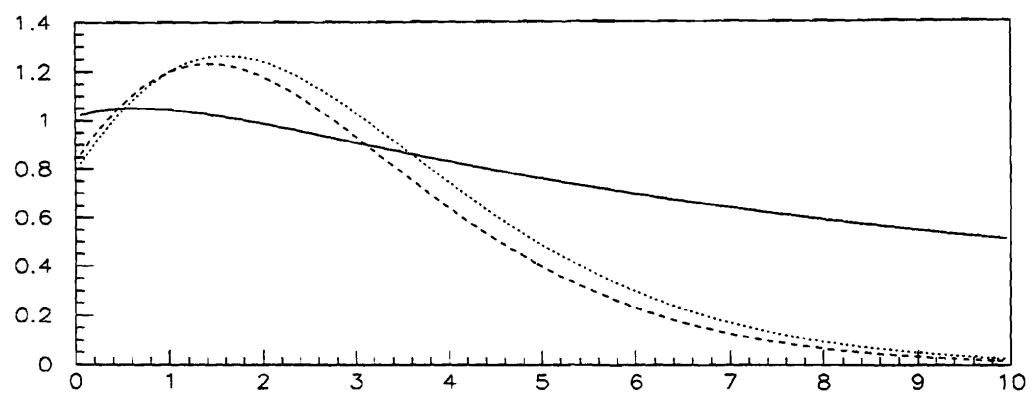

Figure 7.5: D^+ production distribution correction vs. p_T^2 (GeV^2), for π (solid), K (dashed), and p (dotted) beams.

combined π and K beam distributions are found to be consistent with one another. Therefore, in order to minimize systematic errors due to uncertainty in the measured x_F and p_T^2 distributions (see Section 8.2 for the sizes of these errors), combined D cross-sections (for combined π, combined K, or p beams) are used to weight all pseudoscalar D MC events. D^{*+} measured distributions for combined π and p beams are used to weight this species' MC.[7]

[7]For D^{*+}, the combined K beam measurements are not measured with enough precision to justify

MC events are weighted by the following functions:

$$F_{prod.dist.}(x_F, p_T^2) = \frac{N_{meas}(x_F)}{N_{gen}(x_F)} \frac{M_{meas}(p_T^2)}{M_{gen}(p_T^2)}, \tag{7.3}$$

where the subscript "*meas*" denotes a function proportional to the relevant differential cross-section and "*gen*" denotes a functional fit to the number of MC-generated events as a function of the relevant production variable. So that no weighting of generated events is necessary, the numerator functions are normalized so that their areas ($x_F > 0$) are equal to the areas of the denominator functions (i.e., equal to the total number of MC events generated in the forward hemisphere).

Typical MC-generated distributions are shown in Fig. 7.3. For all species, the generated distributions in x_F were fit by the form given in Equation 2.7, in p_T^2 by that given in Equation 2.10. Data distributions in x_F are fit using the same composite function used for the MC. Versus p_T^2, however, combined K and p beam distributions are fit to a simple exponential (see Equation 9.11), while the combined π beam distribution is fit with the two-component FMNR form used for the MC.

As described in Section 4.1, the MC event generator uses π-nucleon collisions as the starting point for every simulated event. We therefore expect the weighting correction described in this section to be largest for p beam, especially versus x_F. In Figs. 7.4 and 7.5, the weighting correction functions used for D^+ MC are shown. In regions where significant fractions of the events reside, the weighting is fairly slight. In order to judge the effect of the weighting on the acceptance, however, we must also convolve these weightings with the variation of the differential acceptances in the important x_F and p_T^2 ranges (see Section 7.4). Not surprisingly, the impact on acceptance of these corrections to the MC production distributions is small; for example, the largest of the D^+ acceptance relative shifts (p beam) is only about 4%.

using them to weight the MC; all meson beam-induced distributions are taken to be consistent with the π beam result.

7.2.4 Lifetime distributions

The proper lifetime t of a charm particle is strongly correlated to the significance of z-separation between primary and secondary (i.e., production and decay) vertices. Since a cut on SDZ is an essential component of event selection for each charm decay mode in this analysis, we expect the acceptance to depend significantly on the lifetime distributions of the various charm species. Therefore, it is crucial that the average lifetimes assumed by the MC generator agree with the best measurements available. As can be seen from Table 7.2, this agreement is quite good for the pseudoscalar mesons in question.

Particle	lifetime τ (ps)	
	Lund	1994 PDG
D^+	1.069	1.057 ± 0.015
D^0	0.428	0.415 ± 0.004
D_s	0.436	0.467 ± 0.017

Table 7.2: MC and world average lifetime values.

In the absolute cross-section analysis, MC events are weighted as a function of their proper lifetime in order to correct for the small discrepancies between the 94 PDG and Lund truth table lifetimes. The weighting function takes the following form:

$$F_{\tau dist.}(t) = \frac{\tau_{Lund}}{\tau_{PDG}} \frac{\exp -t/\tau_{PDG}}{\exp -t/\tau_{Lund}}, \tag{7.4}$$

where the normalization factor gives the two exponential distributions the same area, making weighting of generated events unnecessary, as with the production distribution correction. The relative shifts in the acceptances due to this lifetime distribution weighting are on the order of (but less than) the relative shifts in the lifetimes themselves; this correction brings about relative shifts in the acceptances from $\sim 1\%$ for D^+ to $\sim 3\%$ for D_s.

7.2.5 Drift chamber efficiency

As described in Section 4.2, the average efficiencies of two drift chamber planes (D12, u and v views) were not adequately matched by the input efficiencies used in the positive digitizer. A corrected version of the digitizer, using modified average efficiencies for these two drift chambers, was implemented for D^+ and D^0 modes; D_s MC events, however, were digitized using the old default plane efficiencies.

Run region	beam	χ_{DC}
3	π^+	1.038
	K^+	1.046
	p	1.030
4	p	0.884

Table 7.3: Positive running DC correction factors.

The new D12u and D12v input efficiencies were chosen to match output efficiencies (as returned by the reconstruction code) equaling flux-weighted averages of the measured efficiencies of these two planes (obtained as a function of run number from a sample of PASS0 tapes). These planes were inoperative for significant portions of the positive running (see Section 4.2 for a detailed history). Due to the large fluctuations in these efficiencies, acceptances obtained using positive-digitized MC do not reflect the average efficiencies of the two DC planes in question for run regions corresponding to data subsets (i.e., Regions 3 and 4). Therefore, correction factors were calculated for Regions 3 and 4 using the appropriate flux-weighted averages of acceptances obtained with D^+ MC events digitized to model *separately* the three important regions characterizing D12u and D12v performance (the so-called "on/on", "off/off", and "on/off" regions). These multiplication factors χ_{DC} are calculated as follows:

$$\chi_{DC}(\text{Region } x) = \frac{\sum_i f_i^x \; Acc_i}{Acc_{def}}, \tag{7.5}$$

where the summation runs over the three DC performance regions, the weighting

factors f_i^x give region i's flux fraction in Region x, Acc_i is the D^+ acceptance in region i, and Acc_{def} is the D^+ acceptance averaged over the positive running.

Since differential distribution and trigger efficiency weightings are dependent upon the data subset being simulated, χ_{DC} is calculated separately for each beam particle appropriate to a particular run region; these values are given in Table 7.3. The systematic errors associated with these correction factors are discussed in Section 8.2.

7.2.6 Data subset combination

In the differential analysis, acceptance distributions versus x_F and p_T^2 are needed for combinations of two or more data samples (e.g., two particles or two beams) when the signal estimates for these joint samples are obtained by a fit to a single histogram. In these cases, the corresponding MC signals are combined into a joint histogram as well. As with the data (see Section 6.3), an explicit mass shift is introduced so that different particles can be fit under a single Gaussian. The MC is weighted, however, so that the relative amounts of each constituent event type within the MC signal will mirror the data. Depending on the data sets that are being combined, this weighting can be a function of relative cross-section, branching fraction (B)[8], prescaler value, flux, or number of MC events generated. In combining D^+, D^0, and D_s mesons into combined D signals, the ratios of the cross-sections are assumed to be 2:4:1. Below are given calculations of the various weighting factors $w(x)$, where x indicates the type of MC events actually weighted in a particular combination scenario:

Combining beam particles:

$$\begin{aligned} w(\pi^+\text{beam}) &= (\frac{\pi^+}{\pi^-})_{data} \\ &= (\frac{1.0481 \times 10^{11}}{7.0086 \times 10^{10}})_{flux} \times (\frac{.18081}{.30794})_{prescaler} = 0.879 \qquad (7.6) \\ w(K^-\text{beam}) &= (\frac{K^-}{K^+})_{data} \\ &= (\frac{2.2570 \times 10^9}{5.5848 \times 10^9})_{flux} = 0.404 \qquad (7.7) \end{aligned}$$

[8]We label branching fractions of charm species and their unstable decay products $B_{primary}$ and $B_{secondary}$, respectively.

Combining decay modes:

$$
\begin{aligned}
(\frac{D_s \to K^*K}{D_s \to \phi\pi})_{data} &= (\frac{3.3\%}{3.5\%})_{Bprimary} \times (\frac{66.7\%}{49.1\%})_{Bsecondary} = 1.281 \\
(\frac{D_s \to K^*K}{D_s \to \phi\pi})_{MC} &= (\frac{66.7\%}{49.5\%})_{Bsecondary} \times (\frac{200K}{150K})_{\#generated} = 1.796 \\
w(D_s \to K^*K) &= (\frac{D_s \to K^*K}{D_s \to \phi\pi})_{data} \times (\frac{D_s \to \phi\pi}{D_s \to K^*K})_{MC} \\
&= \frac{1.281}{1.796} = 0.713 \qquad (7.8)
\end{aligned}
$$

Combining particles:

$$
\begin{aligned}
w(D_0 \to K\pi) &= (\frac{D^0 \to K\pi}{D^+ \to K\pi\pi})_{data} \\
&= (\frac{2}{1})_{cross-section} \times (\frac{4.01\%}{9.1\%})_B = 0.881 \qquad (7.9) \\
(\frac{D_s \to \phi\pi}{D^+ \to K\pi\pi})_{data} &= (\frac{1}{2})_{cross-section} \times (\frac{3.5\% \times 49.1\%}{9.1\%})_B = 0.094 \\
(\frac{D_s \to \phi\pi}{D^+ \to K\pi\pi})_{MC} &= (\frac{49.1\%}{100\%})_{Bsecondary} = 0.491 \\
w(D_s \to \phi\pi) &= (\frac{D_s \to \phi\pi}{D^+ \to K\pi\pi})_{data} \times (\frac{D^+ \to K\pi\pi}{D_s \to \phi\pi})_{MC} \\
&= \frac{0.094}{0.491} = 0.191 \qquad (7.10)
\end{aligned}
$$

7.3 MC signals

MC signals are fit (also using log-likelihood) with the same function used to fit the data, except that only flat backgrounds are used. Mass and width are allowed to float. Incidentally, the quality of these fits (as indicated by χ^2/dof and confidence level[9]) is quite low for high-statistics signals. The returned signal estimates, nevertheless, are accurate (deviations on the order of 1σ) estimators of the number of MC signal events.

As in the data signal fits, the fitting procedure is modified for signals binned in x_F and p_T^2), as described in Sections 7.3.1 and 7.3.2. The widths and masses returned

[9]When the term "confidence level" is used with regard to fit quality, it refers to the χ^2 upper-tail probability.

by fits of the total negative (see later comments) MC signals are listed in Table 7.4.

Decay mode	width (MeV)	mass (MeV)
$D^+ \to K\pi\pi$	9.38 ± 0.10	1870.5 ± 0.1
$D^0 \to K\pi$	10.41 ± 0.12	1866.4 ± 0.1
$D^* \to D^0\pi$	11.1 ± 0.2	2012.1 ± 0.2
$D_s \to KK\pi$	8.18 ± 0.13	1970.6 ± 0.1
Combined D	9.74 ± 0.07	1870.7 ± 0.1

Table 7.4: MC signal widths and masses.

For $D^+ \to K\pi\pi$, the negative and positive MC signals are found to have the same width and mass within statistics; for $D^0 \to K\pi$, the differences in width and mass are marginally significant but less than 1 MeV. Therefore, for purposes of this analysis, negative and positive MC are assumed to have the same width and mass. (This becomes relevant soon.) A sampling of fitted MC signals are shown in Fig. 7.6.

7.3.1 MC signals vs. x_F

Signal width is known to be a function of x_F; this dependence is obtained from the MC by fitting signals in 0.1 bins of x_F. In order to minimize the effects of low statistics, the mass of the MC signals is fixed to the mass obtained from the fit of the total MC signal (typically about 1 MeV higher than the 94 PDG mass value). The significance of the x_F-binned MC signals begins to peter out rapidly after the 0.5-0.6 bin; as a result, the widths obtained in the higher-x_F fits fluctuate wildly, both high and low. Therefore, the widths obtained in the x_F range -0.1-0.6 are fitted with a third-order polynomial in order to obtain a smooth function of signal width versus x_F. Widths beyond x_F of 0.6 are determined by projecting this function linearly, using the width and slope at x_F of 0.5. These functions are displayed along with MC signal widths versus x_F in Fig. 7.7. Due to limited statistics, the MC signal widths for the modes $D^* \to D^0\pi$ and $D_s \to KK\pi$ are fixed using the width functions obtained

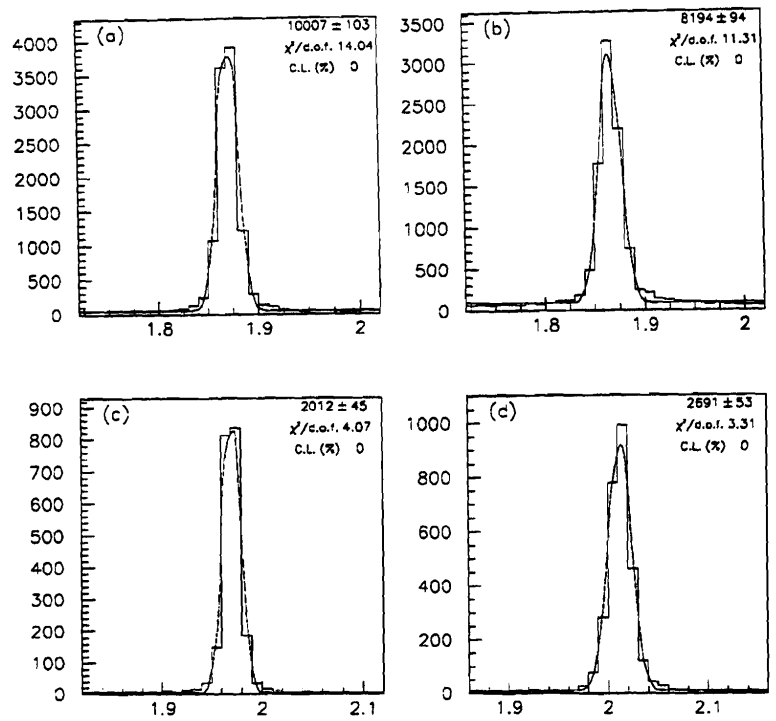

Figure 7.6: Negative-digitized unweighted MC events vs. invariant mass (GeV), $x_F > 0$, for (a) $D^+ \to K\pi\pi$, (b) $D^0 \to K\pi$, (c) $D_s \to \phi\pi$, and (d) $D^* \to D^0\pi$.

from $D^0 \to K\pi$ and $D^+ \to K\pi\pi$ MC respectively (offset by amounts indicated by the total MC signals).

The legitimacy of fixing the MC signal mass to a constant value in all bins of x_F was examined by refitting the $D^+ \to K\pi\pi$ MC signals, allowing the mass to float while keeping the widths fixed. Although some systematic dependence of the signal mass on x_F is apparent (see Fig. 7.8), deviations from constant mass are on the order of a few MeV in the x_F range of most interest. Fixing the mass at values 2 MeV greater and lower than that used in the analysis has no significant impact on the signal estimates returned by the fitter.

In order to determine the signals that go into the calculation of acceptance versus x_F, the MC signals are *refit*, this time fixing the mass *as well as* the widths (using the smooth signal width function). It should be noted that it is the negative MC that is

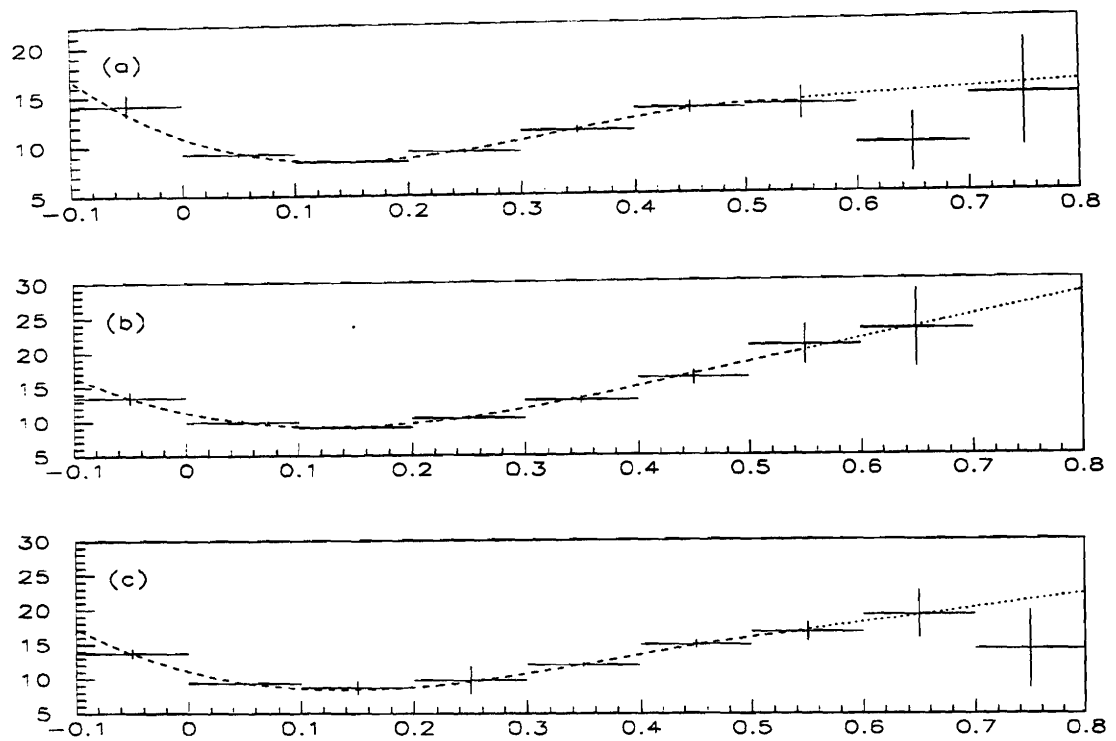

Figure 7.7: MC signal width (MeV) vs. x_F for (a) $D^+ \to K\pi\pi$, (b) $D^0 \to K\pi$, and (c) combined D.

used to obtain the signal widths. For $D^+ \to K\pi\pi$, the negative and positive MC are found to give signal width functions with consistent parameters. For $D^0 \to K\pi$, the correspondence is not as close. Nevertheless, for this mode the positive MC signal estimates obtained using the negative MC signal width function are completely consistent with those obtained using the positive MC signal width function. Therefore, for the sake of simplicity, the negative MC width functions are used across the board. Examples of these fits and the resulting signal estimates are shown for the unweighted negative-digitized combined D MC signals in Fig. 7.9.

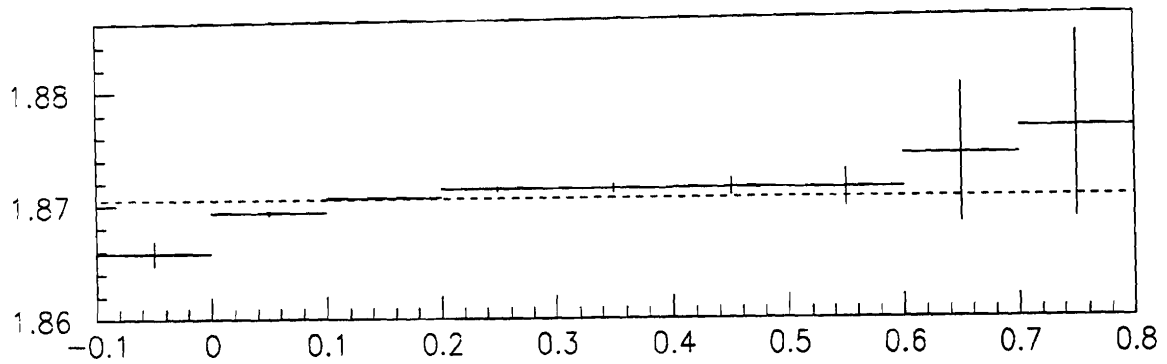

Figure 7.8: $D^+ \to K\pi\pi$, negative MC, signal mass (GeV) vs. x_F. The dotted line indicates the constant mass value used in the $D^+ \to K\pi\pi$ analysis.

7.3.2 MC signals vs. p_T^2

In fitting MC signals broken down into bins of p_T^2 (see Section 6.3.2 for a discussion of the variable binwidths used in the p_T^2 analysis), it is assumed that the signal width does not vary as a function of p_T^2. Both mass and width are fixed to the values obtained from the fit of the total MC signal.

Fits and signal estimates are shown for unweighted negative-digitized combined D modes MC signals in Fig. 7.10. Note that the entire p_T^2 analysis is carried out using positive x_F signals (MC and data) only. Where units are not explicitly shown, p_T^2 is measured in GeV^2.

7.4 Results

In Table 7.5, "geometric" efficiencies ϵ_{geom} are shown for each decay mode. Values are shown for π^- and π^+ beams in order to show the variation of this efficiency with running conditions (the most important of which is beam intensity). As described in Section 7.2.3, dependence of ϵ_{geom} on beam particle type is relatively weak, so kaon and proton beam values are not tabulated. Note, however, that a significant fraction of the p-induced signal events were produced in Region 4, during which ϵ_{geom} is about

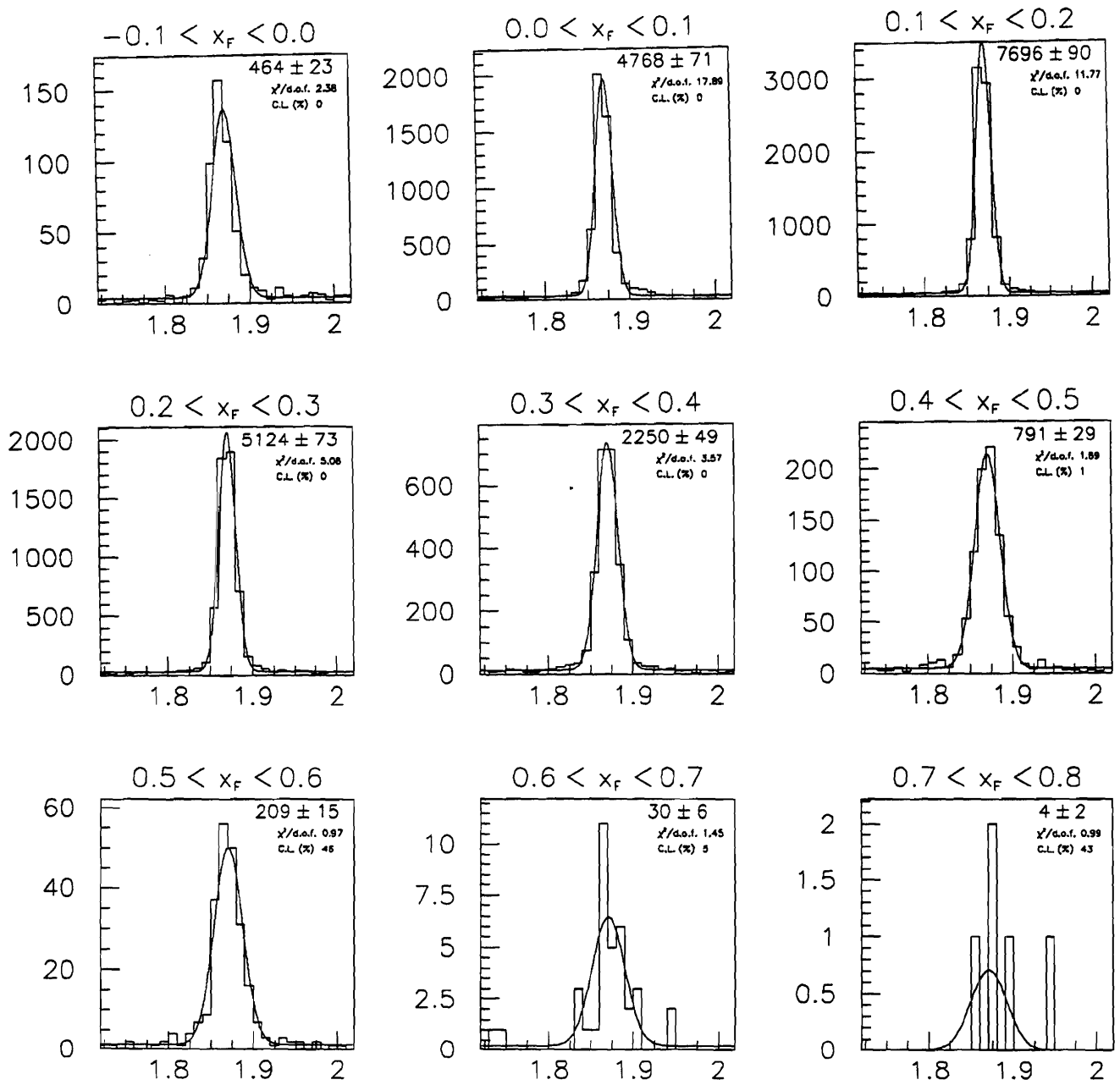

Figure 7.9: Combined D unweighted negative-digitized MC events vs. invariant mass (GeV).

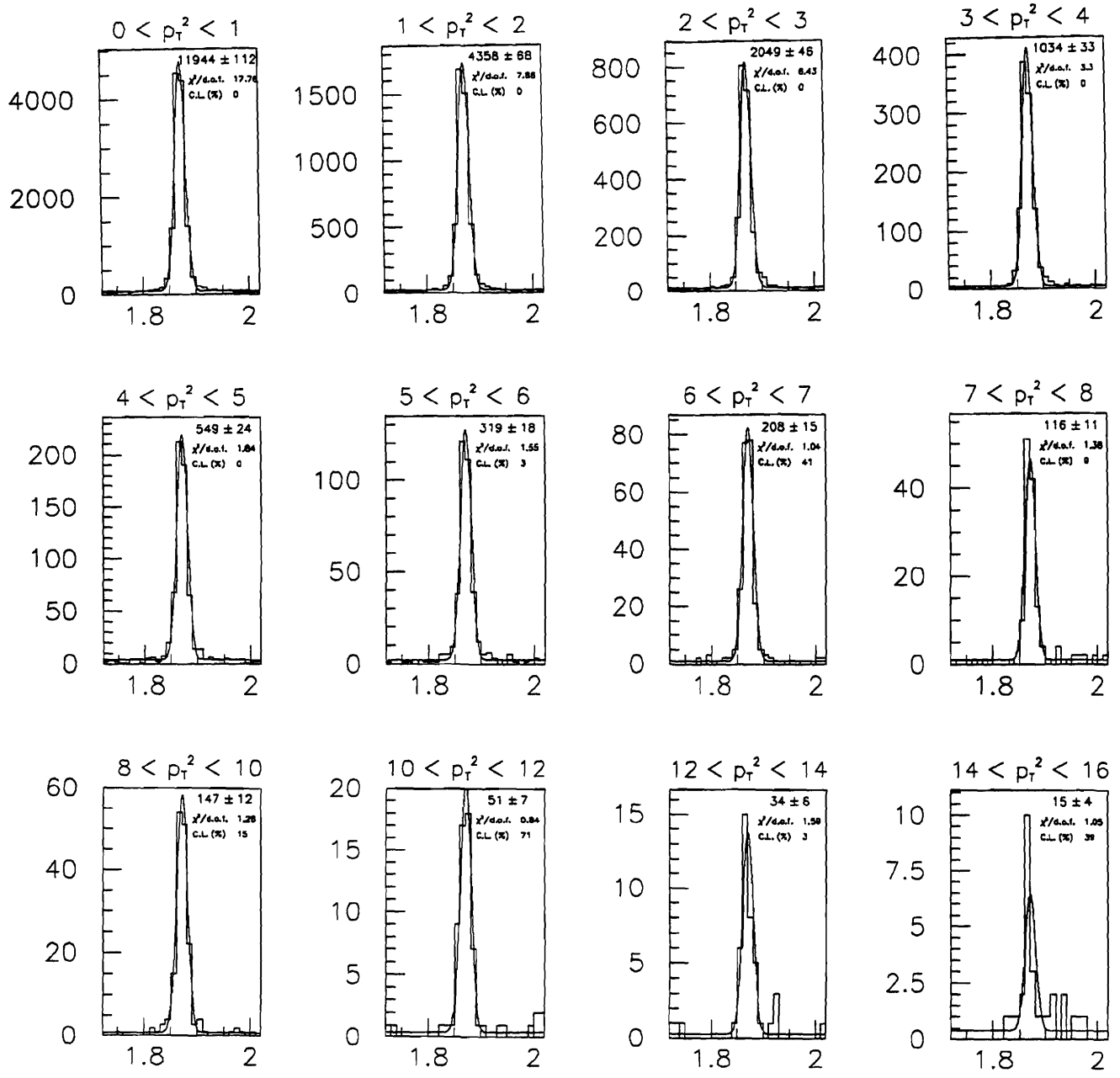

Figure 7.10: Combined D unweighted negative-digitized MC events vs. invariant mass (GeV), $x_F > 0$.

17% lower than in Region 3 due to drift chamber conditions (see Section 7.2.5).

Decay mode	$\epsilon_{geom}(B = \pi^-)$ (%)	$\epsilon_{geom}(B = \pi^+)$ (%)
$D^+ \to K\pi\pi$	8.35 ± 0.08	5.93 ± 0.07
$D^0 \to K\pi$	6.85 ± 0.08	5.36 ± 0.07
$D^* \to D^0\pi$	7.75 ± 0.15	5.59 ± 0.13
$D_s \to \phi\pi$	3.47 ± 0.08	2.31 ± 0.06
$D_s \to K^*K$	2.29 ± 0.05	1.49 ± 0.04

Table 7.5: "Geometric" efficiencies, ($x_F > 0$).

The errors on ϵ_{geom} are determined by taking the *relative* errors on efficiencies derived from weighted and unweighted MC events to be equal; the absolute error on the latter is simply the error on the binomial probability ϵ:

$$\sigma_\epsilon = \sqrt{\frac{(1-\epsilon)\epsilon}{N_{gen}^{MC}}}, \tag{7.11}$$

where ϵ in this case is the "raw" efficiency calculated with unweighted MC. In the rest of this chapter, errors shown on acceptances will be those derived from MC statistics as just described. Additional systematic errors arising from the various weightings used (e.g., ϵ_{trig}) are detailed in Section 8.2.

As defined in the first section of this chapter, "acceptance" is the product of efficiencies ϵ_{trig} and ϵ_{geom}, where the former includes the effect of prescaling. Trigger efficiencies and forward acceptances for $D^+ \to K\pi\pi$ are given in Table 7.6. Because ϵ_{trig} is only weakly dependent on the identities of the charm species in the event, information from Tables 7.5 and 7.6 is sufficient to obtain estimates of acceptance for any data subset/charm meson decay combination relevant to this analysis. The errors shown for the tabulated acceptances arise from MC statistics only; systematic errors in acceptance (including those associated with ϵ_{trig}) are detailed in Section 8.2.2.

The shapes of the differential acceptances do not depend strongly on either charm

Data subset[a]	$\epsilon_{trig}(T, D^+ \to K\pi\pi)^b$ (%)	$Acc(D^+ \to K\pi\pi)$ (%)
Reg. 1 π^-	38	3.18 ± 0.03
Reg. 2 π^-	17	1.406 ± 0.013
Reg. 1 K^-	78	6.51 ± 0.06
Reg. 2 K^-	78	6.41 ± 0.06
π^+	6	0.355 ± 0.004
K^+	89	5.27 ± 0.06
p	9	0.513 ± 0.006

[a]In most cases, specification of the beam particle type is sufficient to determine the data subset (listed in Section 6.2). It must be kept in mind, however, that these data subsets are in general *also* distinguished by different trigger types and run regions.

[b]Recall that these trigger efficiencies include the effects of prescalers.

Table 7.6: $D^+ \to K\pi\pi$ trigger efficiencies and acceptances, ($x_F > 0$).

species or data subset. To support the former independence, combined π beam acceptances are shown for each charm meson species versus x_F and p_T^2 in Figs. 7.11 and 7.12, respectively. The latter is supported by Figs. 7.13 and 7.14, in which combined D acceptances are shown for different beams versus x_F and p_T^2, respectively. The absolute scales of these acceptance plots are correct, given that inefficiencies due to prescalers are not included.[10]

In the combined D acceptance plots, the combined K beam subset has the highest acceptance because all of the data is required to pass only the low-E_T threshold. Next comes the combined π beam subset, the acceptance of which is lowered by the effect of the relative π^-/π^+ prescale and the presence of a component coming in under the high-E_T threshold. Finally, the p beam subset has the lowest acceptance, due not only to a high-E_T component but also to a Region 4 component, with its reduced drift chamber efficiency.

[10]In the case of combined π and p beam acceptances, where two data subsets with differing average prescalers are averaged, the MC is normalized so that the effect of the prescaler on the *more populated* subset is removed; a relative prescale between the two subsets remains.

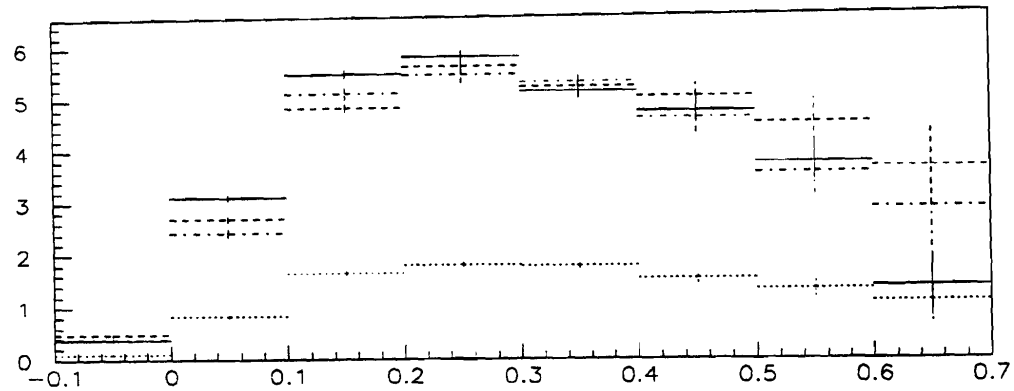

Figure 7.11: π beam acceptance (%) vs. x_F for $D^+ \rightarrow K\pi\pi$ (solid), $D^0 \rightarrow K\pi$ (dashed), $D_s \rightarrow KK\pi$ (dotted), and $D^* \rightarrow D^0\pi$ (dot-dashed).

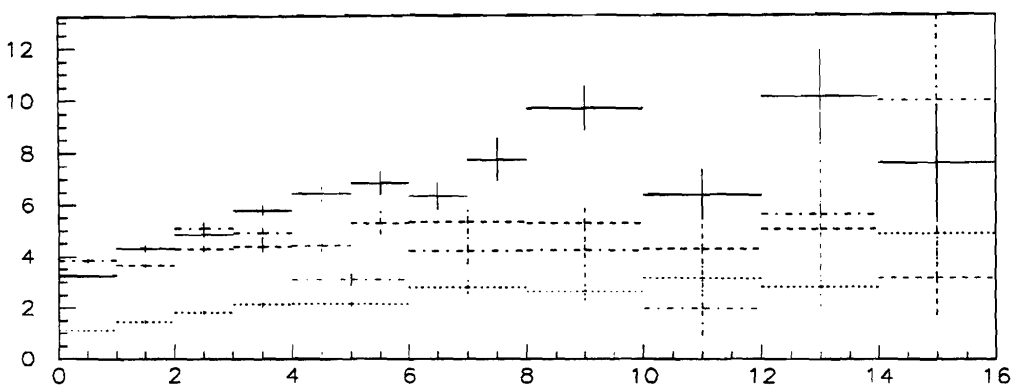

Figure 7.12: π beam acceptance (%) vs. p_T^2 (GeV^2) for $D^+ \rightarrow K\pi\pi$ (solid), $D^0 \rightarrow K\pi$ (dashed), $D_s \rightarrow KK\pi$ (dotted), and $D^* \rightarrow D^0\pi$ (dot-dashed).

As detailed earlier, weighting is introduced when combining MC signals in order to force the relative fractions of each constituent to match those in the corresponding combined data signals. This weighting (except for that simulating relative prescaler values) must also be used to obtain the correct total number of generated MC events. The ratio of these quantities gives the acceptance for combined samples. The error on this acceptance, however, cannot be obtained by simply evaluating the binomial error on the "raw" acceptance, as that would give each constituent equal statistical power

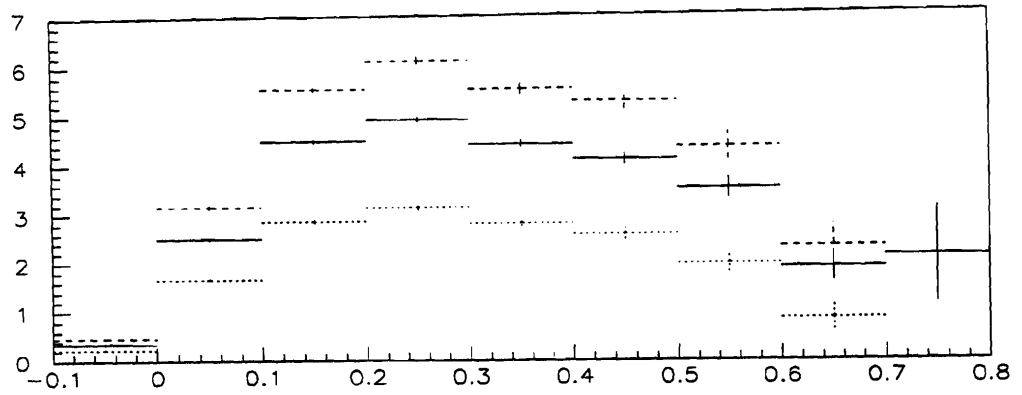

Figure 7.13: Combined D acceptance (%) vs. x_F for combined π beam (solid), combined K beam (dashed), and p beam (dotted).

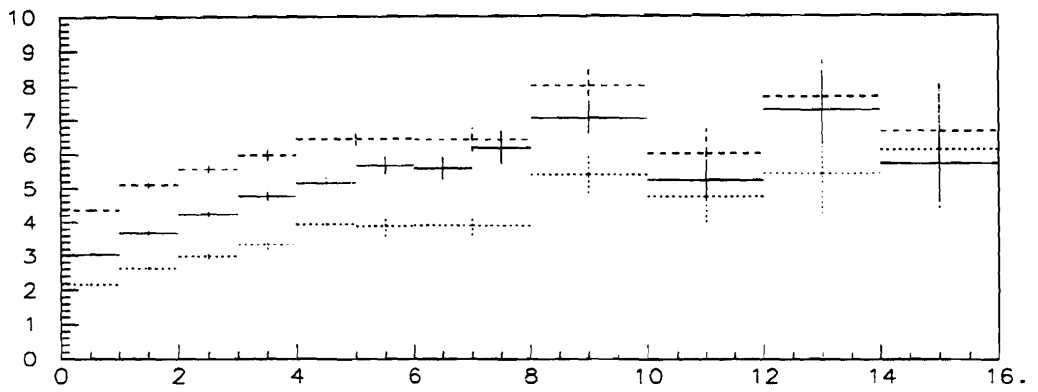

Figure 7.14: Combined D acceptance (%) vs. p_T^2 (GeV^2) for combined π beam (solid), combined K beam (dashed), and p beam (dotted).

(assuming an equal number of generated events) despite the fact that some comprise only a small fraction of the signal after weighting. Therefore, the relative error of a "combined" acceptance is taken to be equal to that of the fraction-weighted sum of the constituent acceptances, each of whose relative errors are in turn derived from their "raw" acceptances, as described above. The combined D calculation is given as an example:

$$\frac{\sigma(Acc_D)}{Acc_D} = \frac{\sigma(\sum_i wgt_i Acc_i)}{\sum_i wgt_i Acc_i} = \frac{\sqrt{\sum_i (wgt_i \sigma(Acc_i))^2}}{\sum_i wgt_i Acc_i}, \qquad i = \begin{cases} D^+ \\ D^0 \\ D_s \to \phi\pi \\ D_s \to K^* K \end{cases} \tag{7.12}$$

Chapter 8

Forward Cross-sections

8.1 Definition and calculation

What is the probability of a collision when a spherical projectile of diameter D_P impinges on a sheet of sparsely-packed spherical targets of diameters D_T? Classically, the answer is simply the product of the number of targets per area multiplied by the *effective* cross-section of one target. Because the projectile has finite size, we can see schematically (Fig. 8.1) that the cross-sectional area about the center of a given target in which a collision will result if entered by the center of a projectile is a circle of diameter $D_{int} = D_P + D_T$. The subscript "*int*" underscores the fact that the effective cross-section is a property of the interaction, that is, of both target and projectile, rather than the target alone.

This concept, the cross-section of an interaction (denoted σ), can usefully be extended to quantify the likelihood of *any* interaction between colliding particles. Here, we are concerned with the cross-section of charm meson production in high-energy collisions of various charged hadrons on a fixed target composed of a variety of nuclear materials. Although wave-particle duality and the presence of long-range forces complicates the interpretation of the total cross-section for interaction between two particles in terms of their physical sizes, in the case of hadronic collisions, where strong interactions dominate, this picture remains essentially valid. Due to color confinement, the strong interaction is at low energy scales effectively mediated not by

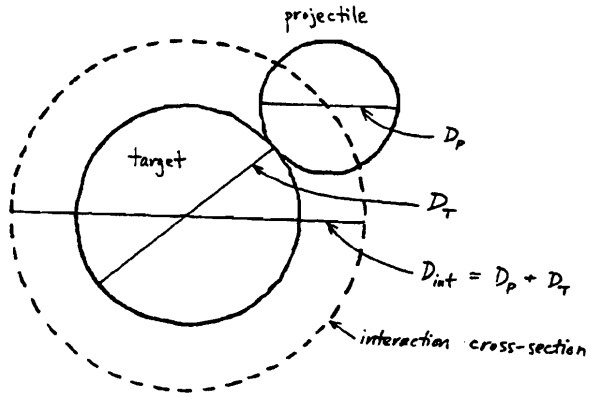

Figure 8.1: Classical cross-section for a collision of two spheres.

the massless gluon but rather by the massive pion. Therefore, the pion mass (~140 MeV) sets the distance scale of strong bonds between color-neutral states at around a fermi. Barring some exotic deconfined state such as quark-gluon plasma, this distance scale will also correspond to the sizes of the hadrons themselves. Take, for example, the total cross-section for pp scattering (elastic plus inelastic) at E769's beam energy, measured to be approximately 40 mb [35]. Solving for the diameter of the proton, we obtain

$$D = \sqrt{\frac{\sigma(pp)}{\pi}} = \sqrt{\frac{40\,\mathrm{mb}}{\pi}} = \sqrt{\frac{40 \times 10^{-27}\,\mathrm{cm}^2}{\pi}} \simeq 1\,\mathrm{fm}, \tag{8.1}$$

which corresponds to measures of nucleonic[1] size obtained by other means.

In the above discussion, we have not addressed the issue of composite targets, such as nuclei, which are roughly-spherical bound states of some number (the atomic mass A) of nucleons. For many processes, the per-nucleus cross-section can be parametrized by the following power law:

[1]The near equality of the total pp and pn cross-sections indicates that protons and neutrons are of the same size, in keeping with isospin symmetry.

$$\sigma_A = \sigma_0 A^\alpha, \tag{8.2}$$

where σ_0 is a constant. Assuming the volume of a nucleus is proportional to A, the "physical" cross-section of the nucleus should be governed by an $\alpha = 2/3$ dependence. In fact, for nucleon-nucleus scattering, $\alpha \simeq 0.7$ [35]. At high momentum transfers, however, we expect the effect of "nuclear shadowing" to diminish for particular hadronic processes as the distance scale of the interaction decreases; in this case, the projectile "sees" nucleons rather than nuclei (and ultimately partons rather than nucleons). In this limit, the nucleus comes to look more and more like a loosely-packed collection of individual nucleonic targets, leading to a linear dependence of the per-nucleus cross-section on A (i.e., $\alpha = 1$). E769 has published measurements of α for both pseudoscalar and vector D production; α in both cases is found to be consistent with unity [7, 9].

The per-nucleon cross-section σ_N is simply related to σ_A:

$$\sigma_N = \frac{\sigma_A}{A} = \sigma_0 A^{\alpha-1} \tag{8.3}$$

For linear A-dependence (which we assume in all that follows), σ_N is constant. We now drop the subscript "N"; all cross-section measurements reported in this thesis are to be understood as cross-sections per nucleon.

Forward cross-sections are determined for each beam particle/beam energy combination present in the data. Since beam polarity, beam energy, DISC pressure setting, and trigger logic all varied one or more times at different points within the experimental running, each of these combinations is naturally associated with a particular subset of E769 events. These subsets are characterized by the run region(s) during which the events were collected and the trigger type(s) under which the events were written to tape. In Section 6.2, these parameters, as well as the beam particle flux (defined below), are tabulated for each data subset. In the following equations, extensive quantities (e.g., number of D events) are understood to be time-integrated (operationally, spill-integrated) sums over the appropriate run region(s); intensive quantities (e.g., trigger efficiency) are understood to be flux-weighted averages over

the same run region(s) unless they are constant or an alternate method of averaging is explicitly described.

The cross-section for inclusive forward production of a particle D in B-nucleon collisions is given by

$$\sigma(BN \rightarrow DX) = \frac{N_{prod}(B,D)}{F(B)\,T_N}. \tag{8.4}$$

In this equation,

$N_{prod}(B,D)$ = number of D's produced through B-target collisions,
$F(B)$ = number of B's incident on the target during the detector's livetime, and
T_N = nucleons/area in the target.

Rather than define the cross-section as a ratio of particle production rates to incident luminosities, we use the equivalent time-integrated quantities. N_{prod} refers to particles produced in the forward hemisphere in the center-of-mass frame of the interaction (i.e., $x_F > 0$); it is given by

$$N_{prod}(B,D) = \frac{N_{obs}(B,T,D \rightarrow xyz)}{B(D \rightarrow xyz)\;\epsilon_{geom}(D \rightarrow xyz)\;\epsilon_{beamID}(B)\;\epsilon_{trig}(T,D \rightarrow xyz)}. \tag{8.5}$$

In this equation,

$N_{obs}(B,T,D \rightarrow xyz)$ = number of D's ($x_F > 0$) observed through invariant mass reconstruction of decay $D \rightarrow xyz$ in events passing trigger T and with positive identification of B,
$B(D \rightarrow xyz)$ = branching fraction for decay $D \rightarrow xyz$,
$\epsilon_{geom}(D \rightarrow xyz)$ = efficiency for observing D ($x_F > 0$) through invariant mass reconstruction of decay $D \rightarrow xyz$,
$\epsilon_{beamID}(B)$ = efficiency for positive identification of B, and
$\epsilon_{trig}(T,D \rightarrow xyz))$ = efficiency for event containing $D \rightarrow xyz$ to pass trigger T.

Decay mode	$B(\%)$
$D^+ \to K\pi\pi$	9.1 ± 0.6
$D^0 \to K\pi$	4.01 ± 0.14
$D_s \to \phi\pi$	3.5 ± 0.4
$\phi \to K^+K^-$	49.1 ± 0.9
$D_s \to K^*K$	3.3 ± 0.5
$K^* \to K^-\pi^+$	$2/3 \times 100$ [a]
$D_s \to KK\pi_{res}$ [b]	3.92 ± 0.39
$D^* \to D^0\pi$	68.1 ± 1.3

[a] Derived from isospin analysis.
[b] Defined as sum of $\phi\pi$ and K^*K contributions to $KK\pi$.

Table 8.1: 94 PDG branching fractions.

In Table 8.1, 94 PDG branching fraction values for the relevant decay modes are listed.

We do not expect the efficiency for tagging a B to depend on whether charm is produced in the event. Therefore, we connect $F(B)$ to its tagged counterpart via the quantity $\epsilon_{beamID}(B)$ defined above:

$$F(B) = \frac{F_{ID}(B)}{\epsilon_{beamID}(B)}, \tag{8.6}$$

where $F_{ID}(B)$ is the number of positively-identified B's incident on the target during the detector's livetime (hereafter called the "B flux").

As described in Section 3.2, beam-particle identification is a two-step process. During spills in which the DISC pressure is set to identify either π, K, or p, a four-fold coincidence from the DISC (with at least one hit in each quadrant) is sufficient to identify the beam particle. If the DISC does not fire or is not set to identify any particular beam particle, however, additional information is required. In the negative running, this information is simply the *a priori* beam probabilities, which indicate that there is a greater than 90% chance that an unidentified beam particle is a π^-. In the positive running, this is not the case; the TRD must be used to distinguish pions

from non-pions. If the DISC is set to tag kaons, *a priori* beam probabilities indicate a greater than 90% chance that a non-DISC-tagged non-pion is a proton rather than a kaon.[2] Therefore, $F_{ID}(B)$ can be written

$$F_{ID}(B) = \chi_{att}(B)\ \chi_{empty}\ (F_{DISC}(B) + F_{NDISC}(B)), \tag{8.7}$$

where χ_{att} is a factor which corrects for the attenuation of the beam upstream of and within the target (see Section 3.3) and χ_{empty} is a subset-dependent factor correcting for the presence of anomalously-empty spills (i.e., spills for which the beam intensity is incorrectly recorded as zero).[3] Both of these correction factors are small, on the order of 1-2%.

The above equation is only approximately correct in that it ignores the contamination of the experimentally-tagged B sample by other beam particles. More properly, we should write

$$F_{trueID}(B) = \sum_b C_{bB}\ F_{ID}(b), \tag{8.8}$$

where the sum runs over beam particles and the matrix element C_{bB} gives the % contamination of "B" by b. A similar procedure would have to be carried out for the charm signals N_{obs} as well. In E769, the definition of positive identification of a beam particle is that the probability for a correct tag is greater than or equal to 90%. This puts an upper limit of 10% on the contamination of any tagged sample by other beams; in most instances, however, the contamination is much lower (see Section 3.2 for a full discussion and tabulation of beam contaminations). In this analysis, we forego this correction and simply use the contaminated beam samples. This simplification is justified not only by the typically low levels of contamination but also (after the fact) by the fairly weak dependence of our measured cross-sections (relative to their statistical precision) on beam particle type.

[2]If the DISC is set to tag protons, this is not the case. Therefore, in Region 4 *only* DISC-tagged protons contribute to the identified proton flux.

[3]This "empty-spill" correction is the kind that normally would have been taken care of through event weeding. Therefore, these correction factors are derived in Section 6.1.

Each component of $F_{ID}(B)$ is calculated using scaler[4] information in one of two ways, depending on the method of beam-particle identification. For DISC-tagged B's, the scaler tallying the number of four-fold coincidences in the DISC (N_{DISC}) can be used as a direct count of events. In this case,

$$F_{DISC}(B) = \sum_{i}^{spills} (N_{DISC})_i \; (\epsilon_{live})_i, \tag{8.9}$$

where the sum runs over spills in which the DISC pressure is set to tag B and ϵ_{live} is the detector livetime. Note that in the absolute cross-section analysis, full-weeding of events (including scalers) is required.

The DISC, whose four-fold coincidences are amenable to counting, is included in E769's trigger logic to enhance the number of K and p-induced charm events written to tape. The output of the TRD, on the other hand, consists of multiple signals, up to one from each of its planes. TRD beam probabilities are (run-dependent) functions of the number of planes that fire. Thus, the TRD is not used to trigger events, and no scaler N_{TRD} exists to provide tagged-B totals analogous to N_{DISC}. For non-DISC-tagged B's, fluxes must therefore be calculated from the scaler tally of the total number of beam particles impinging on the target (N_{BEAM}). In this case,

$$F_{NDISC}(B) = f(B) \sum_{i}^{spills} (N_{BEAM})_i \; \epsilon_{NDISC}(B)_i \; (\epsilon_{live})_i, \tag{8.10}$$

where the sum runs over all spills, $f(B)$ is the *a priori* B probability, and $\epsilon_{NDISC}(B)$ is the efficiency for tagging B through means other than the DISC. (Since in the negative running, *all* non-DISC-tagged particles are identified as π^-, the product $f(\pi^-)\,\epsilon_{NDISC}(\pi^-)$ should be taken to equal one.) This equation, however, does not include all of the information that is potentially available, namely the DISC setting and how many times the DISC fired in each spill; it is therefore only applicable for spills in which the DISC is not set to tag anything or is not operational.

The need for a modification in the more general case that the DISC *is* set is made clear by an example. In order to count the number of beam pions in a spill during

[4]See Section 3.6 for a discussion of the scalers used in this analysis.

which the DISC is set to tag kaons, we apply efficiencies to the scaler count only after the positively-identified kaons have been subtracted. The beam probabilities $f(B)$ must therefore also be adjusted in order to reflect the particle fractions in the remaining subset of the beam. These refinements lead to the following equation:

$$F_{NDISC}(B) = \sum_{i}^{spills} (N_{BEAM} - N_{DISC})_i \; f'(B)_i \; \epsilon_{NDISC}(B)_i \; (\epsilon_{live})_i, \tag{8.11}$$

where the sum runs over spills with the DISC set to tag something and $f'(B)$ is the B probability in the absence of a DISC tag, given by

$$f'(B) = \frac{(1 - \delta_{bB}\, \epsilon_{DISC})\, f(B)}{1 - \epsilon_{DISC}\, f(b)}, \tag{8.12}$$

where the DISC is set to b, δ_{bB} is equal to 1 if $b = B$ and equal to zero otherwise, and ϵ_{DISC} is the tagging efficiency of the DISC.[5] (As explained above, $f'(\pi^-)\, \epsilon_{NDISC}(\pi^-)$ should be taken to equal one.) The efficiencies ϵ_{DISC} and ϵ_{NDISC} are discussed in Section 3.2.

The cross-section is given its dimension by the T_N term, given by

$$T_N = N_{AV} \sum_{i}^{mat.} \rho_i \, t_i, \tag{8.13}$$

where the sum runs over the materials comprising the target. In this equation,

N_{AV} = Avogadro's number = 6.022×10^{23},
ρ = mass density in grams/volume, and
t = thickness along the beam direction.

In this analysis, charm particles produced in all 26 target foils (comprised of four materials) as well as in the interaction scintillator are included in the final data samples. The target is described (including the densities and thicknesses of its components)

[5]The DISC efficiency is taken to be independent of B. The systematic error associated with this assumption is discussed in Section 8.2.

in Section 3.3. The simple calculation described above leads to the following result: $T_N = 1.66 \times 10^{-3}$ nucleons/mb.

By defining the acceptance $Acc(T, D \rightarrow xyz)$ as the product of $\epsilon_{geom}(D \rightarrow xyz)$ and $\epsilon_{trig}(T, D \rightarrow xyz)$ (see Section 7.4 for a full discussion), we can now write the cross-section equation in terms of directly-measured quantities:

$$\sigma(BN \rightarrow DX) = \frac{N_{obs}(B, T, D \rightarrow xyz)}{B(D \rightarrow xyz)\ Acc(T, D \rightarrow xyz)\ F_{ID}(B)\ T_N}. \tag{8.14}$$

Forward cross-section results for each beam/particle combination are tabulated in Section 8.3.1. For information regarding the numerical values of the various inputs to the above equation, refer to the relevant sections:

$N_{obs}(B, T, D \rightarrow xyz)$	Section 6.3
$Acc(T, D \rightarrow xyz)$	Section 7.4
$B(D \rightarrow xyz)$	Section 8.1
$F_{ID}(B)$	Section 6.2
T_N	Section 8.1

8.2 Systematic errors

The precision of cross-section measurements is limited by statistical uncertainty (σ_{stat}) in the number of events seen N_{obs}; in most cases, although analysis cuts have been optimized to maximize the statistical significance of the D signals, σ_{stat} remains the dominant contribution to the overall error. As described in Section 6.3, signal estimates are obtained through log-likelihood fits. The standard (or "1σ") error on a fit parameter (such as the number of signal events) is returned by the fitter on the basis of how variations in that parameter affect the quality of the fit, in this case quantified by the log-likelihood function. Although the details of the fitting procedure may differ, ultimately the statistical error on the number of signal events is determined through Poisson statistics by the numbers of signal and background events in the invariant mass range corresponding to a given particle decay; σ_{stat} is therefore

separated from errors which arise from other sources, such as procedural choices in the analysis or lack of precise knowledge of experimental conditions. These latter errors are called "systematic" and are discussed in this section; statistical errors are compiled in Section 6.3.

The total systematic error on a cross-section is given by the systematic errors on the data signal, acceptance, and flux, where these independent contributions are added in quadrature. (Errors in the cross-sections due to uncertainty in the branching fractions of decay modes are listed separately from errors contingent upon E769-specific details.) In comparing two cross-section results, it is important to know which components of their respective systematic errors are common to both and which are independent. Systematic errors of the forward cross-sections are usefully divided into two categories: those which depend on the data subset and those which do not. In reporting cross-sections, the systematic errors will be split along this line. While this allows for convenient calculation of the appropriate common systematic error for a comparison of, say, D^+ cross-sections for production induced by different beams, a different comparison, for example between π-induced D^+ and D^0 cross-sections, will require a different partitioning of systematic errors. In the following subsections, the reader will be given enough information to derive the systematic error appropriate to any given comparison of forward cross-section results. Note that these systematic errors are tabulated as *relative* errors on the relevant quantities.

8.2.1 Data signals

In addition to the statistical error on N_{obs} mentioned above, a systematic error on this quantity, attributable to choices made in the fitting procedure, can be estimated. Two potential contributions to this error were examined, namely, uncertainty in the data signal estimates due to the fixed widths and fixed central masses chosen. As described in Section 6.3, widths are fixed to floating values obtained by fits to the total simply-weeded signals and masses are fixed to 94 PDG values. The mean change in the signal estimate due to fixing these quantities at $\pm 1\sigma$ from the central value is taken to be the systematic error. Errors associated with the fixed signal width are listed in Table 8.2; no significant error arises from the uncertainties in the PDG

masses, which are known to better than 1 MeV.

Data subset	D^+	D^0	D_s	D^*
Reg. 1 π^-	2.4%	2.3%		
Reg. 2 π^-	2.0%	2.3%	5.5%	2.7%
Reg. 1 K^-	2.4%	1.6%		
Reg. 2 K^-	1.3%	2.0%	2.5%	.9%
π^+	1.9%	3.1%	4.5%	2.9%
K^+	1.6%	3.1%	2.4%	4.4%
p	1.9%	3.2%	8.9%	5.7%

Table 8.2: Systematic errors on data signal estimates due to uncertainty in fixed data signal width.

8.2.2 Acceptance

As described in Section 7.4, the systematic error on acceptances due to statistical error in the MC signals are determined using unweighted MC for each species. These errors are given in Table 8.3. In addition to these, there are systematic errors associated with each of the MC weighting functions used (or in the case of the Čerenkov efficiency correction, *not* used) in the absolute cross-section analysis.

Beam polarity	D^+	D^0	D_s	D^*
negative	1.0%	1.1%	1.7%	1.8%
positive	1.2%	1.2%	2.1%	2.2%

Table 8.3: Systematic errors on acceptance due to MC statistics.

The errors associated with the drift chamber efficiency correction factors χ_{DC} (see Section 7.2.5) are derived from MC statistics in the same way as those listed above,

except that the overall error is obtained by propagating the errors on each of the acceptances in the flux-weighted average corresponding to a given run region. These errors are listed in Table 8.4. Because χ_{DC} is derived using D^+ MC, the treatment of errors for this particle differs from that for the remaining species (see footnotes in Table 8.4).

Data subset	$F_{prod}(x_F)$	$F_{prod}(p_T^2)$	ϵ_{trig}	χ_{DC}	total σ_{syst}
Reg. 1 or 2 π^-	0.2%	0.9%			
Reg. 1 π^-			0.7%	—	1.2%
Reg. 2 π^-			1.0%		1.4%
Reg. 1 or 2 K^-	0.4%	1.6%			
Reg. 1 K^-			0.2%	—	1.7%
Reg. 2 K^-			0.1%		1.7%
π^+	0.1%	1.2%	1.0%	0.7% (1.4%)[a]	5.2% (5.3%)[b]
K^+	0.1%	1.7%	0.1%	0.7% (1.4%)	1.8% (2.2%)
Reg. 3 p			1.0%	0.7% (1.4%)	
Reg. 4 p			0.5%	1.0% (1.5%)	
Reg. 3+4 p	1.2%	2.2%			6.3% (6.4%)

[a]For D^+, the error on the DC efficiency correction factor *replaces* the error due to MC statistics. For other particles, the DC efficiency error in parentheses is *added in quadrature* to the MC statistical error.

[b]Total systematic errors in parentheses are for particles other than D^+.

Table 8.4: Data subset-dependent systematic errors on acceptance. $F_{prod}(x_F)$ and $F_{prod}(p_T^2)$ errors for D^* are calculated separately.

Up to this point, the systematic errors have been calculated using standard error propagation for a function of one or more independent variables. In the cases of differential distribution and trigger efficiency weighting, however, the function (here, the acceptance) depends on a number of correlated variables, namely the parameters returned by some fit. In order to take these correlations into account correctly, we use the following formula:

$$\sigma_{syst}(Acc) \equiv \sqrt{\sigma^2(Acc)} = \sqrt{\sum_i (\frac{\partial Acc}{\partial x_i}\ \sigma(x_i))^2 + 2\sum_{i>j} \rho_{ij}\ \frac{\partial Acc}{\partial x_i}\ \frac{\partial Acc}{\partial x_j}\ \sigma(x_i)\ \sigma(x_j)}, \tag{8.15}$$

where the sum runs over a set of correlated variables x, ρ_{ij} is the correlation coefficient for x_i and x_j (an element of the error matrix returned by MINUIT), and $\sigma(x_i)$ is the 1σ variation in x_i.

The systematic errors associated with differential distribution weighting are not expected to depend strongly on the charm species. Therefore, D^+ MC is used to determine this error for all species except D^*, for which these errors are separately calculated. Similarly, errors associated with trigger efficiency weighting were also found using D^+. Both of these contributions to the systematic error on acceptance are given in Table 8.4; see Table 8.5 for the D^* systematic errors. In all cases, these weighting errors prove to be relatively small components of their respective total systematic errors.

Data subset	$F_{prod}(x_F)$	$F_{prod}(p_T^2)$	total σ_{syst}
π/K	1.5%	1.5%	2.1%
p	3.6%	0.9%	3.7%

Table 8.5: Systematic errors on D^* acceptance due to differential distribution weighting.

As discussed in Section 7.2.2, no Čerenkov efficiency weighting was implemented in the absolute cross-section analysis. The uncertainty in the data-determined efficiency is used, however, to calculate a contribution to the overall systematic error on acceptance. Here the independent parameters which are adjusted are the Čerenkov efficiencies in each bin of p_K. After summing in quadrature the effect of these variations, the total systematic error due to uncertainty in the Čerenkov kaon identification efficiency is found to be 4.2%. Note that this is the error for one kaon decay product; therefore, this systematic error is doubled for the D_s modes. Clearly, this error

dominates the systematic uncertainty on acceptance.

In Table 8.6, the acceptance uncertainties associated with the errors in the 94 PDG average lifetime values are given; these were measured by varying the lifetimes (via weighting) by $\pm 1\sigma$ and noting the effect on acceptance. The relative errors on acceptance were found to go as those on the lifetimes themselves, multiplied by 150%, independent of data subset.

Particle	$F_{\tau dist.}$
D^+	1.2%
D^0	1.4%
D_s	5.5%
D^*	1.2%

Table 8.6: Systematic errors due to lifetime weighting.

8.2.3 Flux

Of the factors that go into the calculation of live flux, only ϵ_{live}, $f'(\pi^+)$, and $f'(p)$ are found to have significant systematic errors associated with them. Due to the large numbers involved, the raw flux totals obtained from scaler sums have no appreciable statistical errors. By weeding out of the absolute cross-section analysis spills for which these scalers are missing or pathological in some way, large systematic errors are also avoided; this weeding is described in Section 6.1. In the positive running, another potential source of systematic error is ϵ_{NDISC} (here, ϵ_{TRD}). Again, because high-statistics fits are used to determine TRD beam probabilities as a function of the number of TRD planes which fire (see Section 3.2), no significant contribution to the systematic error on the positive fluxes arises.

As detailed in Section 3.6, the detector livetime is calculated as a ratio of scalers, specifically the ratio of the scaler downstream of the PLU counting prescaled interaction triggers to the corresponding upstream scaler. Since the PLU is disabled while

the DA system is busy with an event, this ratio provides a high-statistics measure of ϵ_{live}. This procedure for measuring livetime is not the only one possible; an alternative is to take the ratio of scalers at the end and beginning of the strobe stream leading into the PLU, which is disabled during deadtime by the absence of a strobe input signal. One would expect these two measures of livetime to be the same. An average discrepancy of about 1.5%, however, was found between the two. This is taken as an estimate of the systematic uncertainty in ϵ_{live}, which contributes to the total systematic error on the flux.

In the negative running, where beam particle identification proceeds using DISC information or by default in the absence of same, the *a priori* beam probabilities do not come into the flux calculation. As detailed in Section 8.1, these beam fractions (or more precisely, their modified counterparts $f'(\pi^+)$ and $f'(p)$) are needed to determine non-DISC-tagged fluxes in Region 3. Although uncertainty in the DISC-tagging efficiency does lead to uncertainties in these quantities, this contribution is negligible compared to that arising from the intrinsic uncertainties in $f(\pi^+)$ and $f(p)$ themselves. These *a priori* beam probabilities are determined from fits to DISC pressure curves (see Section 3.2), with relative uncertainties of 4.9% and 8.8%, respectively.

8.2.4 Summary

In Table 8.7, total E769-dependent (everything excluding the branching fraction errors) systematic errors are given for each data subset/charm species combination. Note that these errors are correlated with one another to some degree both vertically and horizontally within the table. In addition to these, uncertainties in the 94 PDG branching fractions for the relevant modes contribute the following relative errors into the forward cross-section results: 6.6% for D^+, 3.5% for D^0, 9.9% for D_s, and 4.0% for D^*.

Data subset	D^+	D^0	D_s	D^*
Reg. 1 π^-	5.5%	5.4%		
Reg. 2 π^-	5.3%	5.5%	11.5%	6.3%
Reg. 1 K^-	5.4%	5.3%		
Reg. 2 K^-	5.2%	5.4%	10.8%	5.9%
π^+	7.4%	7.7%	12.7%	8.1%
K^+	5.1%	6.1%	10.8%	7.1%
p	7.9%	8.7%	15.1%	10.0%

Table 8.7: Total E769-dependent systematic errors.

8.3 Results

8.3.1 Forward cross-sections

The results for absolute forward production cross-sections, the calculation of which was outlined in Section 8.1, are tabulated here (Tables 8.8-8.11) for each beam particle/charm meson combination. For D^+ and D^0, 210 GeV beam energy results are given in addition to those at 250 GeV. Four absolute errors are shown for each cross-section value: (1) statistical, (2) data subset-dependent systematic, (3) data subset-independent systematic, and (4) branching fraction. In cases where the data signal has less than a 3σ statistical significance, Bayesian 90% confidence level lower and upper limits are also given.[6] Combined π and K beam weighted averages are calculated.

Over the range in beam energy at which modern fixed-target measurements of charm particle cross-sections have been made (200-800 GeV), $\sigma_{c\bar{c}}$ is expected to rise rapidly; at E769's energy, a rate of increase of about 50% per 100 GeV is predicted. Our 250 (210) GeV results are therefore only directly comparable to those published

[6]The cross-section probability distribution is taken to be a Gaussian with a center and standard deviation as indicated in the tables and the unphysical region below zero excluded. The lower (upper) limit is calculated by finding the boundary of the lower (upper) tail of this distribution whose area is 10% of the total.

B	$\sigma(BN \to D^+X, x_F > 0)$ (μb/nucleon)
π^-	$3.58 \pm 0.23 \pm 0.10 \pm 0.16 \pm 0.23$
	$(1.72 \pm 0.26 \pm 0.05 \pm 0.08 \pm 0.11)$
π^+	$2.58 \pm 0.30 \pm 0.15 \pm 0.12 \pm 0.17$
π	$3.21 \pm 0.18 \pm 0.08 \pm 0.15 \pm 0.21$
K^-	$3.29 \pm 0.68 \pm 0.08 \pm 0.15 \pm 0.22$
	$(3.37 \pm 1.06 \pm 0.10 \pm 0.15 \pm 0.22)$
K^+	$2.90 \pm 0.39 \pm 0.07 \pm 0.13 \pm 0.19$
K	$3.00 \pm 0.34 \pm 0.06 \pm 0.14 \pm 0.20$
p	$3.25 \pm 0.42 \pm 0.21 \pm 0.15 \pm 0.21$

Table 8.8: D^+ forward cross-sections, 250 (210) GeV beam.

B	$\sigma(BN \to D^0X, x_F > 0)$ (μb/nucleon)
π^-	$8.24 \pm 0.70 \pm 0.25 \pm 0.38 \pm 0.28$
	$(6.36 \pm 0.89 \pm 0.18 \pm 0.29 \pm 0.22)$
π^+	$5.71 \pm 0.86 \pm 0.35 \pm 0.27 \pm 0.20$
π	$7.23 \pm 0.54 \pm 0.21 \pm 0.34 \pm 0.25$
K^-	$7.62 \pm 2.07 \pm 0.22 \pm 0.35 \pm 0.26$
	$(4.74 \pm 2.75 \pm 0.12 \pm 0.22 \pm 0.16)$
K^+	$7.07 \pm 1.22 \pm 0.28 \pm 0.33 \pm 0.24$
K	$7.21 \pm 1.05 \pm 0.22 \pm 0.34 \pm 0.25$
p	$5.65 \pm 1.35 \pm 0.41 \pm 0.27 \pm 0.20$

Table 8.9: D^0 forward cross-sections, 250 (210) GeV beam.

by the ACCMOR NA32 collaboration for their 230 (200) GeV π^- and K^- beam runs [17, 19].[7] These results are given in Table 8.12. Considering NA32's relatively low statistics, it is not surprising that our cross-sections are consistent with theirs for each case in which comparison is possible. Note that these and other previous

[7]We limit our comparisons to direct measurements of forward cross-sections (as opposed to extrapolations from more limited x_F ranges).

B	$\sigma(BN \to D_s X, x_F > 0)$ (μb/nucleon)	90% C.L. limits
π^-	$2.11 \pm 0.44 \pm 0.12 \pm 0.21 \pm 0.21$	
π^+	$1.97 \pm 0.61 \pm 0.15 \pm 0.20 \pm 0.19$	
π	$2.06 \pm 0.36 \pm 0.09 \pm 0.21 \pm 0.20$	
K^-	$2.44 \pm 1.36 \pm 0.08 \pm 0.25 \pm 0.24$	$> 0.90, < 4.46$
K^+	$3.35 \pm 0.96 \pm 0.12 \pm 0.34 \pm 0.33$	
K	$3.04 \pm 0.79 \pm 0.08 \pm 0.31 \pm 0.30$	
p	$1.41 \pm 0.85 \pm 0.16 \pm 0.14 \pm 0.14$	$> 0.49, < 2.57$

Table 8.10: D_s forward cross-sections, 250 GeV beam.

B	$\sigma(BN \to D^* X, x_F > 0)$ (μb/nucleon)	90% C.L. limits
π^-	$2.71 \pm 0.33 \pm 0.11 \pm 0.13 \pm 0.11$	
π^+	$3.13 \pm 0.49 \pm 0.21 \pm 0.14 \pm 0.12$	
π	$2.84 \pm 0.27 \pm 0.10 \pm 0.13 \pm 0.11$	
K^-	$1.23 \pm 0.80 \pm 0.04 \pm 0.06 \pm 0.05$	$> 0.41, < 2.29$
K^+	$1.90 \pm 0.56 \pm 0.10 \pm 0.09 \pm 0.08$	
K	$1.67 \pm 0.46 \pm 0.07 \pm 0.08 \pm 0.07$	
p	$1.78 \pm 0.59 \pm 0.16 \pm 0.08 \pm 0.07$	

Table 8.11: D^* forward cross-sections, 250 GeV beam.

measurements reported in this and following subsections are adjusted where necessary to correspond to 94 PDG branching fractions; systematic errors (in which branching fraction errors are included) are changed accordingly.

Both D^+ and D^0 cross-section values have been published by most modern fixed-target experiments which address charm hadroproduction issues. Since the sum of these two species forms a significant fraction of the total charm cross-section,[8] these measurements can be used to assess the current state of theory. In Figs. 8.2 and

[8]Just what fraction of the charm cross-section might be comprised of D^+ and D^0 will be discussed later in this section.

B	$\sigma(BN \to DX, x_F > 0)$ (μb/nucleon)			
	D^+	D^0	D_s	D^*
π^-	$2.7 \pm 0.2 \pm 0.6$	$6.1 \pm 0.3 \pm 1.3$	$1.4 \pm 0.2 \pm 0.2$	$2.4 \pm 0.2 \pm 0.6$
	$(2.0\ ^{+0.5}_{-0.3} \pm 0.2)$	$(4.2\ ^{+0.6}_{-0.4} \pm 0.5)$	—	$(2.0 \pm 0.5 \pm 0.2)$
K^-	—	—	$2.3 \pm 1.2 \pm 0.5$	—
	$(4.7\ ^{+1.4}_{-1.0} \pm 0.5)$	$(5.0\ ^{+1.9}_{-1.1} \pm 0.5)$	$(5.8\ ^{+2.4}_{-1.4} \pm 1.0)$	$(2.9 \pm 1.4 \pm 0.3)$

Table 8.12: NA32 forward cross-sections, 230 (200) GeV beam [17,19].

8.3, we compare E769 results for π[9] and p-induced production of charm mesons (D^+, D^-, D^0, and $\overline{D}^0$) to results of previous experiments [17, 19, 2, 4, 12, 29, 30] as a function of beam energy. Also plotted are next-to-leading order (NLO) QCD predictions for the total charm plus anticharm particle forward cross-section; these are obtained by multiplying the $c\bar{c}$ cross-section, generated using the program of Mangano *et al.* [33], by a factor of 2 and requiring the c quark to have $x_F > 0$. HMRSB (SMRS2) parton distribution functions are assumed for target nucleons and beam protons (pions) [28], and theoretical parameters have been set to the default values used in [32]. An underestimate of the theoretical uncertainty has been obtained by varying the renormalization scale; other contributions, most notably those due to uncertainties in the charm quark mass and factorization scale, are expected to be at least as large [32]. If fragmentation is assumed to be constant as a function of energy, the energy dependence of D meson cross-sections can be directly compared to the theory for quarks; the agreement over the energy range shown appears reasonable.

In order to assess the accuracy of the NLO QCD central prediction for the total charm particle cross-section ($x_F > 0$), an estimate must be made of the fraction of the total cross-section accounted for by presently-measured species. Cross-section information on one further charm hadron is available, namely the lightest charm

[9]In the π beam plot, although all other experiments measure π^--induced production, E769's *combined* π beam result is used in order to maximize precision. The assumption implicit in this procedure, namely, that charm production is insensitive (at least at the level of E769 precision) to the charge of mesons impinging on a nuclear target, is discussed in Section 8.3.2.

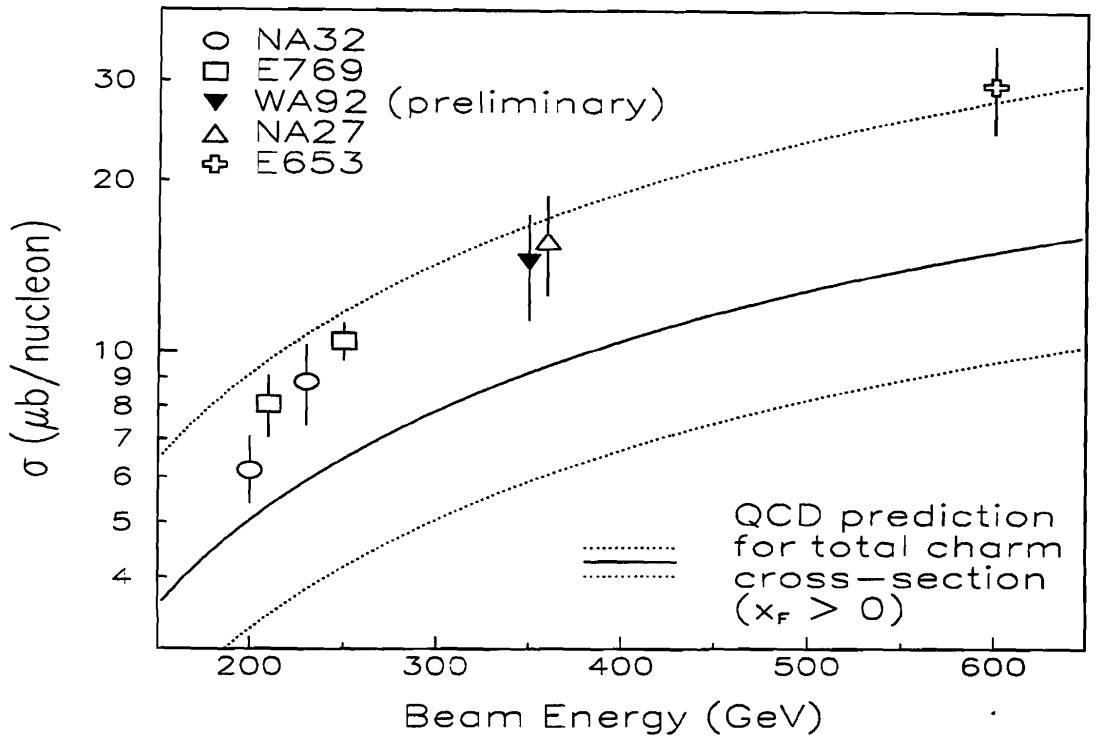

Figure 8.2: $\sigma(\pi N \to DX,\ x_F > 0)$, $D = D^+, D^-, D^0$, and $\overline{D}^0$. Measured values for E769 and previous experiments [17,19,2,29] compared to NLO QCD prediction [32] for total forward charm plus anticharm particle production. The band bordered by the dotted lines is an underestimate of the theoretical uncertainty in the central value represented by the solid line. Error bars include branching fraction uncertainty.

baryon Λ_c. In the same paper in which the forward cross-section results of this analysis are presented, a well-measured Λ_c cross-section (combined π beam) of $3.4 \pm 1.1 \pm 0.5$ μb/nucleon is given [10]. This value is consistent with that measured by NA32 with a 230 GeV π^- beam: $4.1 \pm 0.5 \pm 0.7$ μb/nucleon [18]. Weighted averages of π^- and π^+ beam results for the species D^+, D^0, D_s, and Λ_c and their antiparticles are summed in order to obtain our most precise partial measure of the charm plus anticharm particle cross-section ($x_F > 0$): $15.9 \pm 1.3 \pm 0.9$ μb/nucleon.

Forward production of Λ_c is evidently not suppressed with respect to D^+ at this energy. This and the significant D_s cross-section make it probable that undetected

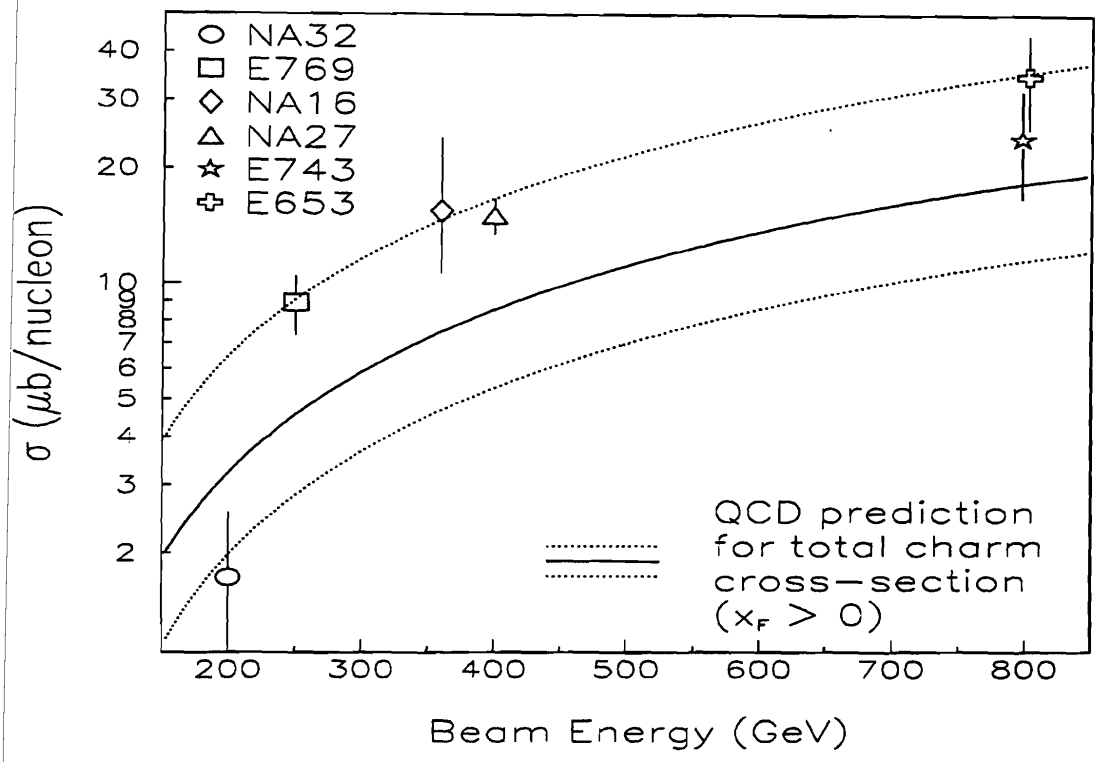

Figure 8.3: $\sigma(pN \to DX,\ x_F > 0)$, $D = D^+, D^-, D^0$, and $\overline{D}^0$. See explanation in Fig. 8.2 caption, replacing the references cited therein with [17,1,4,12,30]. Here, cross-sections shown for NA27 [4], E743 [12], and E653 [29] are 50% of values published for all x_F.

(including charm strange) baryonic species contribute appreciably to the total charm cross-section. Including an estimate for unseen charm species, it is evident that the NLO QCD central prediction for the total charm cross-section is low by about a factor of three. Given the huge latitude in normalization allowed by the current state of theory, however, this discrepancy is not particularly telling. It is interesting, nevertheless, to note that the $b\bar{b}$ cross-section predicted by QCD is also low compared with measurements [38].

8.3.2 Beam particle dependence

Before discussing the dependence of charm cross-sections on the three E769 beam species (π, K, p), we will justify the procedure of combining oppositely-charged meson beam results for purposes of comparison with results from previous experiments, which are obtained with π^- and K^- beams only. With its negatively and positively-charged mixed hadron beams, E769 is the first experiment to provide data (for both π and K) addressing this issue.

As discussed in Chapter 2, charm production at E769's energy is expected to be dominated (80% or more) by gg fusion, the balance coming primarily from $q\overline{q}$ annihilation. Since oppositely-charged mesons are charge conjugates of one another, specification of one set of parton distributions suffices to determine the other. Given the near u-d symmetry of the nuclear target (good to within a few percent), we do not expect between π^- and π^+ beams any significant difference in the hard-scattering amplitudes underlying charm production.[10] The situation with charged kaons is different, due to the replacement of d with s, the latter of which only contributes to the "sea" component of the target's parton distributions. The valence $\overline{u}$ quark of the K^- can annihilate with valence u quarks in the target, a mechanism not available in K^+-induced production. We therefore expect K^--induced cross-sections to be higher than those for K^+ by an amount on the order of 10%,[11] everything else being equal.

The only other likely mechanism for enhancement of production induced by one sign of beam meson over the other is the leading-particle effect (defined in Section 2.5). Measurements of this effect for different beam/charm meson combinations are given in Section 8.3.4. As a rough estimate, however, suffice it to say that in the forward hemisphere, the probability of hadronization to a leading charm meson is as much as 160% that for the non-leading antimeson. In this analysis, we combine leading and non-leading mesons (i.e., particle and antiparticle) into common signals, thereby

[10]The u-d mass difference is too slight compared to the available energy to have any measurable effect.

[11]The fraction of πN charm production attributable to $q\overline{q}$ annihilation is 20%. For the present estimate, however, we must subtract away "valence-sea" $q\overline{q}$ interactions. Assuming these latter occur with the $q\overline{q}$ probability predicted in pN charm production (10%), we obtain the rough prediction for K^- beam enhancement given in the text.

diluting this enhancement to the 15-30% level over the *neutral*-leading case and eliminating completely any discrepancy between charm particle cross-sections expected with beam particles of opposite sign.

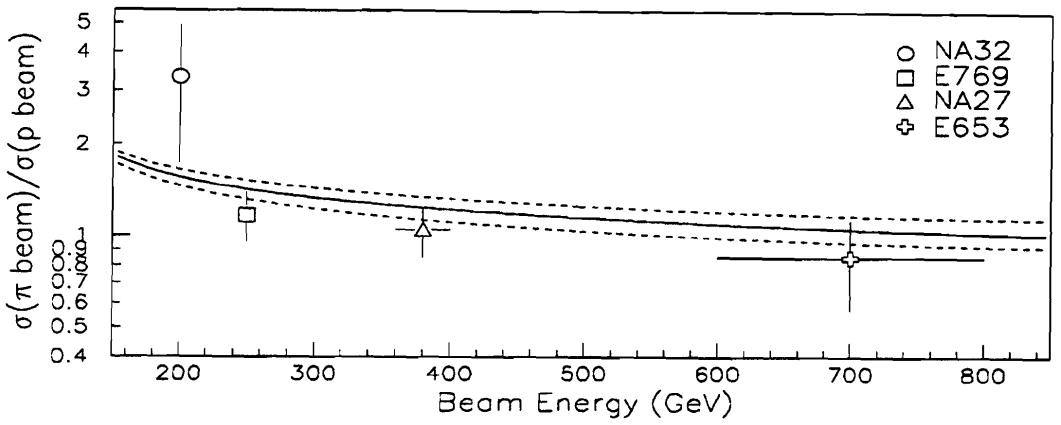

Figure 8.4: Ratio of $\sigma(\pi N \to DX,\, x_F > 0)$ to $\sigma(pN \to DX,\, x_F > 0)$ vs. beam energy (GeV), $D = D^+, D^-, D^0$, and $\overline{D}^0$. Measured values for E769 and previous experiments compared to NLO QCD prediction for total forward $c\bar{c}$ production (solid line). The band bordered by the dashed lines represents the theoretical uncertainty associated with parton distributions in the pion; an analogous uncertainty due to the proton should also contribute, but is not shown.

For π^- (K^+) beam, our most precise cross-section measurement for an individual charm species is at the 10% (15%) level. Therefore, any expected discrepancies should be indistinguishable from statistical fluctuations. It remains to be demonstrated, however, that no theoretically unexpected effects are at work. Our most precise measure of the π^-/π^+ beam cross-section ratio is obtained by summing D^+, D^0, and D_s mesons:

$$\frac{\sigma(\pi^- N \to DX,\, x_F > 0)}{\sigma(\pi^+ N \to DX,\, x_F > 0)} = 1.36 \pm 0.17 \pm 0.09. \tag{8.16}$$

For D^+ and D^0, the differences between π^- and π^+ beam cross-sections are only marginally significant, providing no compelling evidence of a physical effect.[12] For

[12] A lengthy search for a systematic cause, however, turned up nothing.

the kaon beams, the corresponding ratio is calculated without including D_s, which is not well-measured for K^-:

$$\frac{\sigma(K^-N \to DX,\ x_F > 0)}{\sigma(K^+N \to DX,\ x_F > 0)} = 1.09 \pm 0.26 \pm 0.04. \tag{8.17}$$

On the basis of this evidence (and the accompanying theoretical prejudice), combined π and K beam cross-sections are used for comparisons with previous measurements.

The total charm cross-section is expected to exhibit a significant dependence on beam, this sensitivity deriving in particular from the gluon momentum distributions of the interacting hadrons. As detailed in Chapter 2, this dependence can be expressed in terms of the first two moments of the beam particle gluon distribution, $<g>_{thr}$ and $<xg>_{thr}$, where the subscript indicates that the lower limit of integration is an effective charm threshold. Non-gg contributions to charm production must also be taken into account in predicting ratios of cross-sections for different beams. In this section we present ratios of forward charm particle plus antiparticle cross-sections, whose predicted values potentially differ from those for $\sigma_{c\bar{c}}$ due to two additional factors: forward-backward asymmetry in meson-nucleon hadroproduction and leading-particle enhancement. See Chapter 2 for a full discussion of these effects.

Comparing our measured forward cross-sections for different beams, no significant beam dependence in any of the individual D or combined pseudoscalar[13] cross-sections is found, suggesting that the average fractions of pion, kaon, and proton momenta carried by gluons above the charm threshold are at least comparable. In order to present our most precise measures of beam-particle dependence, we combine D^+ and D^0 results[14] for π, K, and p beams. These ratios are given in Table 8.13. Our π/K ratio is consistent with that obtained by NA32 at 200 GeV: $0.67\ ^{+0.14}_{-0.18}$ [17].

Well-measured parton distributions are available for the pion and proton, so a QCD prediction for the π/p cross-section ratio can be made. In Fig. 8.4, previous measurements[15] are compared to the theoretical prediction as a function of beam

[13] D^* cross-sections are not independent of those for D^+ or D^0 mesons, to which D^* decays strongly.

[14] p-induced D_s production is not well-measured.

[15] For the remainder of this chapter, measurements from other experiments are given without additional referencing. The reader is referred to the captions of Figs. 8.2 and 8.3.

B_1/B_2	$\frac{\sigma(B_1 N \to DX, x_F>0)}{\sigma(B_2 N \to DX, x_F>0)}$
π/p	$1.17 \pm 0.20 \pm 0.08$
K/p	$1.15 \pm 0.22 \pm 0.08$
π/K	$1.02 \pm 0.12 \pm 0.03$

Table 8.13: D forward cross-section ratios, $D = D^+, D^-, D^0$, and $\overline{D}^0$, 250 GeV beam.

energy. Horizontal error bars on the NA27 and E653 points reflect the fact that π^- and p beam measurements were made at different energies. Above 300 GeV, however, this ratio is expected to be relatively insensitive to beam energy. The data is consistent with the theoretical prediction, the measured π/p cross-section ratios following the expected decline with beam energy.

8.3.3 Hadronization

The total charm cross-section is the sum of cross-sections for all possible charm particles and antiparticles, divided by a factor to eliminate double-counting of $c\bar{c}$ pairs.[16] Cross-sections for all charm species, most notably charm baryons, have not yet been measured (or measured well). In connecting measured cross-sections to $\sigma_{c\bar{c}}$, it is therefore important to estimate the contribution of "missing" charm to the total. This requires knowing to what extent production of heavier charm hadrons is suppressed with respect to the "light" D^+ and D^0 mesons. As hadronization is a process that involves the exchange of many soft gluons, it cannot be treated in the context of perturbative QCD. Measurement of cross-section ratios for the lighter charm particles can at least provide experimental input for phenomenological models of hadronization (e.g., Monte Carlo fragmentation algorithms). In this section, we present cross-section ratio values and compare them to previous measurements.

Pseudoscalar D mesons are created either through hadronization of a charm quark or decay of a vector D^*; these processes are known as direct and indirect production,

[16]This factor would be exactly two if not for the existence of charmonium states.

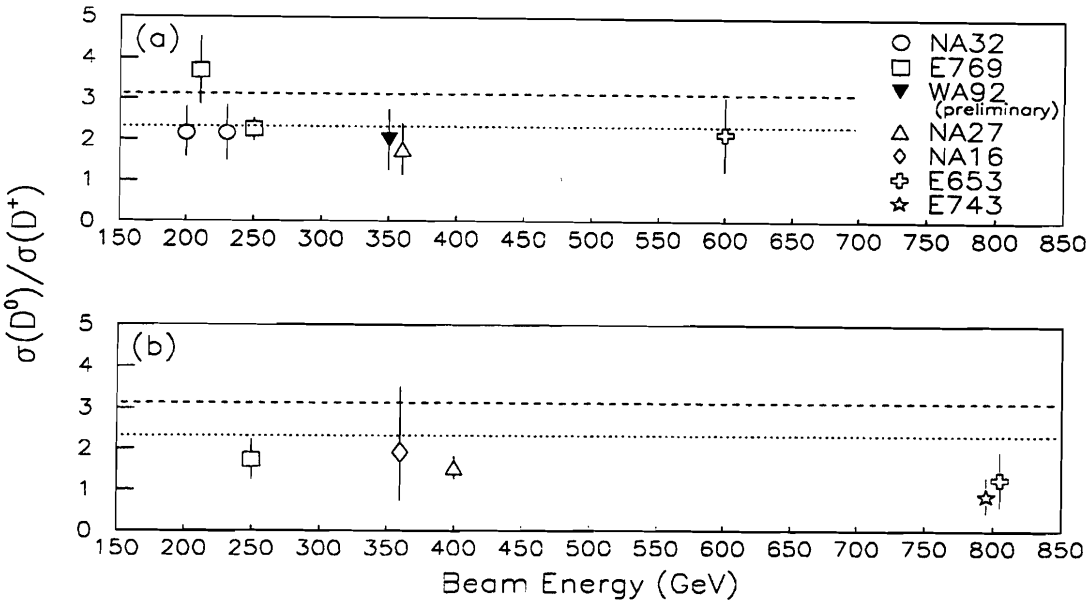

Figure 8.5: Ratio of $\sigma(BN \to D^0X,\ x_F > 0)$ to $\sigma(BN \to D^+X,\ x_F > 0)$ vs. beam energy (GeV) for (a) π and (b) p beams. Measured values for E769 and previous experiments compared to "simple-model" prediction (see text) assuming 94 (dashed) and 90 (dotted) PDG D^{*+} branching fractions.

respectively. By making two plausible assumptions, it is possible to predict the ratio of D^0 to D^+ cross-sections. First, we assume that $u\bar{u}$ and $d\bar{d}$ pairs are created with equal probability in the aftermath of a collision of high-energy hadrons. This implies that equal numbers of charged and neutral light D mesons will be produced. Second, we assume that hadronization to vector mesons (charged and neutral) is enhanced by a factor of three over corresponding pseudoscalar mesons. Since charged (neutral) D^*'s decay preferentially (exclusively) to D^0, the D^0 cross-section is expected to be higher than that for D^+.

In Fig. 8.5, measurements by E769 and previous experiments of the D^0/D^+ forward cross-section ratio are presented as a function of beam energy for π and p beams. Two "simple-model" predictions are given, corresponding to 94 and 90 PDG D^{*+} branching fractions. Interestingly, the data seems to conform much more closely

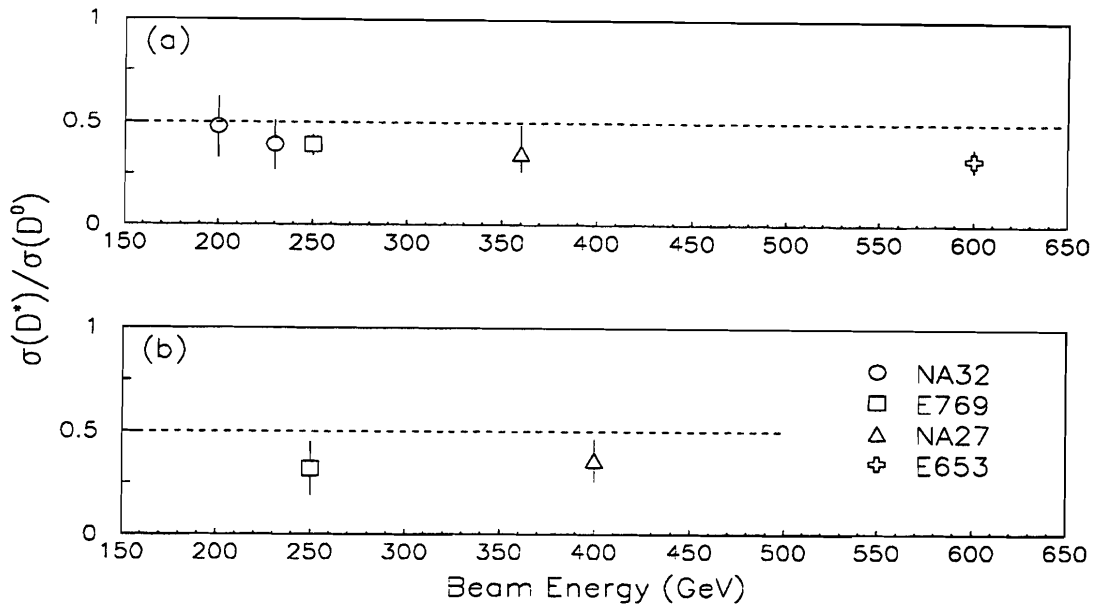

Figure 8.6: Ratio of $\sigma(BN \to D^{*+}X,\, x_F > 0)$ to $\sigma(BN \to D^0X,\, x_F > 0)$ vs. beam energy (GeV) for (a) π and (b) p beams. Measured values for E769 and previous experiments compared to "simple-model" prediction (see text) assuming 94 PDG D^{*+} branching fractions (dashed).

to the latter. The 94 PDG branching fractions for D^{*+} are dominated by a single set of measurements (1992 CLEO II). Assuming that these more recent branching fractions are accurate, one or both of the aforementioned assumptions might have to be discarded. The value of the D^0/D^+ cross-section ratio is much more sensitive to the charged/neutral ratio than to the vector/pseudoscalar ratio, making the former the more likely candidate for modification. In order to reach agreement with the general trend in π beam data, however, a charged/neutral (i.e., $d\bar{d}/u\bar{u}$) ratio of more than 1.5 must be assumed! Note that the p beam ratio is expected to be raised somewhat by higher leading-particle enhancement of D^0 over D^+. For neither π nor p beam is there any compelling evidence of energy dependence in the D^0/D^+ cross-section ratio.

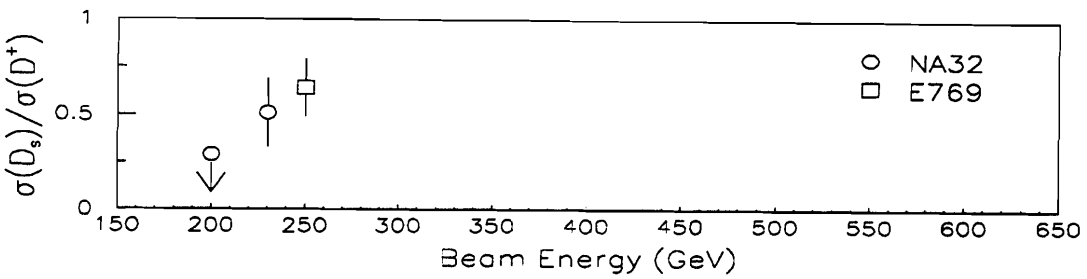

Figure 8.7: Ratio of $\sigma(\pi N \to D_s X,\, x_F > 0)$ to $\sigma(\pi N \to D^+ X,\, x_F > 0)$ vs. beam energy (GeV). Measured values for E769 and NA32.

The assumptions discussed above also lead to a prediction for the D^{*+}/D^0 cross-section ratio. In Fig. 8.6, E769 and previous measurements of this quantity are presented for π and p beams. Unlike the D^0/D^+ ratio, the ratio of D^{*+} to D^0 is not particularly sensitive to the D^{*+} branching fractions assumed; therefore, only the simple-model prediction assuming 94 PDG values is plotted. The data for both beams tends to fall significantly below the expected ratio. Only the p beam ratio should be affected (in this case, lowered) by differential leading-particle enhancement. Interestingly, these measured values of the D^{*+}/D^0 cross-section ratio (which is also sensitive to the charged/neutral ratio) favor a charged/neutral ratio of around 0.7, a change in the direction opposite to that indicated by the D^0/D^+ ratio. It seems evident that some modification must be made to the simple model used in making these predictions, such as allowing the vector/pseudoscalar ratio to differ in the charged and neutral D cases.

In Fig. 8.7, we present a final cross-section ratio, namely D_s/D^+. As these mesons are identical except for the replacement of a d by an s quark, this ratio gives a measure of the suppression of the heavier quark's production at this energy. In interpreting this ratio, however, it should be recalled that only about one third of D^{*+}'s decay to D^+ while all D_s^*'s decay to D_s.

Beam	Particle	Leading flavor(s)	A
π	D_s	none	-0.11 ± 0.07
K	D^+	none	-0.11 ± 0.07
	D^0	u or none	-0.19 ± 0.06
	D_s	s	0.25 ± 0.11
p	D^+	d	0.18 ± 0.05
	D^0	u or d	0.06 ± 0.06
	D_s	none	-0.10 ± 0.17
	D^*	d	0.36 ± 0.13

Table 8.14: Leading particle asymmetries ($x_F > 0$). Statistical errors are shown; systematic errors are negligible. For beam/particle combinations for which the leading-particle effect is undefined (neutral-leading case) or diluted by indirect production (K beam, D^0), the asymmetry is defined as that between particle (containing c) and antiparticle (containing $\bar{c}$), irrespective of beam particle charge.

8.3.4 Leading-particle asymmetries

One aspect of hadroproduction which cannot be treated perturbatively is the leading-particle effect, which is defined and discussed in Chapter 2. The size of this effect is usually quantified as a leading-particle asymmetry A, defined as

$$A \equiv \frac{\sigma(\text{leading}) - \sigma(\text{nonleading})}{\sigma(\text{leading}) + \sigma(\text{nonleading})}, \tag{8.18}$$

where $\sigma(x)$ is the forward cross-section for x particles. Since the absolute normalization cancels out in this quantity, the cross-sections σ can be calculated as simply the number of x events divided by the acceptance, as a function of x_F, integrated over $x_F > 0$. This binwise calculation is important because A has been measured to have a strong dependence on x_F [8]. Measured values of A for production of various charm particles for K and p beams are shown in Table 8.14.

The asymmetry induced by a leading s quark is found to be consistent with that of the lighter quarks. These A values should be compared with our previously-published

π beam results, $A_{D^+} = 0.18 \pm 0.06$, $A_{D^0} = -0.06 \pm 0.07$, and $A_{D^*} = 0.09 \pm 0.06$ [6, 9].[17]

[17]The D^+ and D^0 results are obtained with π^- beam data only. The latter is diluted by indirect production.

Chapter 9

Differential Cross-sections

9.1 Definition and calculation

Perturbative QCD, in addition to providing a prediction of the production cross-section of $c\bar{c}$ pairs in hadronic collisions, can be used to calculate the momentum distribution of these charm quarks.[1] This distribution is a scalar function of momentum, where the domain in momentum space is limited by kinematic constraints to a sphere of radius p_{max}.[2] Integration of the distribution function over this volume V_{int} yields a value equal to the total cross-section:

$$\sigma = \oint_{V_{int}} \frac{d^3\sigma}{d^3p}\, dV = \int_0^{2\pi} \int_0^{p_{max}} \int_{-p_{max}}^{p_{max}} \frac{d^3\sigma}{dp_L\, dp_T\, d\phi}\, dp_L\, dp_T\, d\phi, \tag{9.1}$$

where p_L is the longitudinal component of the momentum (parallel to the beam axis), p_T is the transverse component, and ϕ is the azimuthal angle about the beam axis. Neither the beam nor the target in E769 is polarized; the absence of any preferred direction which can break the azimuthal symmetry about the beam axis allows us integrate away the ϕ dependence without loss of generality. Further transforming

[1] Here, "charm quarks" is meant to include both quarks and antiquarks. Interestingly, QCD predicts a tiny difference in the c and $\bar{c}$ momentum distributions [37]. In this analysis, we measure the particle-plus-antiparticle differential cross-sections of a given charm meson; therefore we probe indirectly the *average* of the charm quark and antiquark distributions.

[2] As implied by the spherical shape, we are defining momentum in the center-of-mass frame of the interaction. Therefore, p_{max} is given by $E_{CM}/2$ ($\simeq$ 10.8 GeV for E769).

variables, we obtain

$$\sigma = \int_0^{p_{max}} \int_{-p_{max}}^{p_{max}} \frac{d^2\sigma}{dp_L\, dp_T}\, dp_L\, dp_T = \int_0^{p^2_{max}} \int_{-1}^{1} \frac{d^2\sigma}{dx_F\, dp_T^2}\, dx_F\, dp_T^2. \tag{9.2}$$

Use of the Feynman-x variable facilitates comparison of longitudinal distributions obtained at different energies; such comparisons test the zeroth-order scale invariance expected from the constituent parton model. Via the change from p_T to p_T^2, we obtain a transverse momentum distribution with a simple form which does not vanish at zero.

The bivariate distribution $\frac{d^2\sigma}{dx_F\, dp_T^2}(x_F, p_T^2)$ cannot be factored into a product of x_F and p_T^2-independent parts. Given the level of precision afforded by our data (not to mention the current state of theory), no valuable information is sacrificed by treating the two momentum components separately. We therefore confine our study to measurements of the differential cross-section distributions in each variable, integrated over the other variable:

$$\frac{d\sigma}{dx_F}(x_F) = \int_0^{p^2_{max}} \frac{d^2\sigma}{dx_F\, dp_T^2}(x_F, p_T^2)\, dp_T^2 \tag{9.3}$$

$$\left.\frac{d\sigma}{dp_T^2}(p_T^2)\right|_{x_F>0} = \int_0^1 \frac{d^2\sigma}{dx_F\, dp_T^2}(x_F, p_T^2)\, dx_F. \tag{9.4}$$

Note that this definition of the transverse distribution will apply in all that follows, even when the label "$x_F > 0$" is dropped. The extension of the above discussion to differential cross-section distributions for charm mesons is straightforward: the momentum of the quark is simply replaced by the momentum of the hadron containing the quark. Issues surrounding the expected relationship between the quark and hadron distributions are discussed in Chapter 2.

In practice, we measure the $d\sigma/dx_F$ and $d\sigma/dp_T^2$ distributions by obtaining approximate[3] samples of them at a number of points. In order to illustrate the procedure, we use the longitudinal differential cross-section of D meson production, where B represents the beam particle:

[3]Given the bin sizes used in this analysis, the errors associated with this approximation are negligible.

$$\frac{d\sigma}{dx_F}(BN \to DX;\, x_{F(i)}) \simeq \frac{1}{\Delta_i} \int_{x_{F(i)}-\Delta_i/2}^{x_{F(i)}+\Delta_i/2} \frac{d\sigma}{dx'_F}\, dx'_F = \frac{N_{prod}(B, D;\, x_{F(i)})}{F(B)\, T_N}. \quad (9.5)$$

In this equation, $x_{F(i)}$ (Δ_i) is the central value (width[4]) of the ith x_F bin, $N_{prod}(x_{F(i)})$ is the number of D's produced ($|x_F - x_{F(i)}| < \Delta_i/2$) through B-target collisions, and $F(B)$ and T_N appear in the analogous absolute cross-section equation (Equation 8.4).

By binning all $x_F(p_T^2)$-dependent quantities, the calculation of $d\sigma/dx_F$ ($d\sigma/dp_T^2$) in each bin can be carried out exactly as that outlined in Section 8.1.[5] It is easier, however, to discard temporarily all quantities which do not depend on x_F (p_T^2), calculate the shape of the differential distribution, and then fix the normalization so that following equations holds:

$$\sigma(BN \to DX)_{x_F>0} = \sum_i^{x_F>0} \frac{d\sigma}{dx_F}(BN \to DX;\, x_{F(i)})\, \Delta_i \quad (9.6)$$

$$= \sum_j \frac{d\sigma}{dp_T^2}(BN \to DX;\, p_{T(j)}^2)\, \Delta_j, \quad (9.7)$$

where the sum i (j) runs over x_F (p_T^2) bins for which there is data.

Dropping the subscript which indicates the binning of the kinematic variables, it is now sufficient to write

$$\frac{d\sigma}{dx_F}(BN \to DX;\, x_F) \propto \frac{N_{obs}(B, T, D \to xyz;\, x_F)}{Acc(T, D \to xyz;\, x_F)}$$

$$= \frac{N_{obs}(B, T, D \to xyz;\, x_F)\; N_{gen}^{MC}(D \to xyz;\, x_F)}{\hat{N}_{obs}^{MC}(T, D \to xyz;\, x_F)}. \quad (9.8)$$

See the text immediately following Equation 7.1 or 8.14 for the definitions of these quantities. Note that the MC weighting used to obtain $\hat{N}_{obs}^{MC}$ differs in the absolute

[4]The x_F bins have a constant width of 0.1, but as explained in Section 6.3.2, the width of a p_T^2 bin is either 1 or 2 GeV^2.

[5]This binning procedure rests on the assumption that measurement resolutions for x_F and p_T^2 are small compared to the relevant bin width. This assumption is supported by MC studies, which indicate that typical measurement errors associated with these variables are on order of 10% of the bin width used.

and differential cross-section analyses; these differences are detailed in Section 7.1. An equation analogous to (9.8) holds for $d\sigma/dp_T^2$.

In Section 9.3.1, combined D differential cross-section results ($d\sigma/dx_F$ and $d\sigma/dp_T^2$) for combined π, combined K, and p beams are tabulated. In addition, for those (combined or individual) charm species/beam combinations for which the differential distributions are well-measured, plots showing fits to standard parametrizations are provided.

9.2 Systematic errors

The conclusion of this section will be that systematic errors on the shapes[6] of the differential cross-section distributions are negligible compared to their statistical counterparts. Despite the caveats placed on the interpretation of the standard shape parameters as fundamental physical quantities (see Section 9.3.1), nevertheless they remain our most useful handle on variation in the shapes of $d\sigma/dx_F$ and $d\sigma/dp_T^2$ due to any given change in assumptions or analysis procedure.

Distributions in x_F (p_T^2) are generally well-fit by functions with one (one or two) shape parameters, namely n (b or α and β); the specific forms of these functions, the quality of given fits, and the values of parameters returned by these fits are discussed in detail in Section 9.3.1. For our present purpose, we need only know the scales of the typical statistical errors in these parameters so that we may judge whether a given systematic error contributes appreciably when combined in quadrature. For our highest-statistics sample (combined π beam, combined D), n is measured to a relative precision of 4.4%, b to 4.6%, α to 21%, and β to 12%.

Information concerning systematic dependencies of D meson differential distribution shapes can be found in the extensive previous studies carried out by members of the E769 collaboration. Two E769 papers reporting differential cross-section results have been published. The first ([6]) is on π^--induced production of D^+ and D^0, the second ([9]) on $\pi^\pm$-induced production of D^{*+}. We will concern ourselves with the

[6]Because these distributions are presented with absolute normalization, the systematic errors detailed in Section 8.2 apply. However, in this chapter we concern ourselves only with the shapes of the distributions, which are in general much less sensitive to these effects.

former (including supporting studies found in the theses of E769 graduate students [41, 43]); due to the relatively-low statistics of the D^* signal used in this analysis, statistical errors are sure to swamp any systematic effects connected specifically to this species.

In the pseudoscalar D paper, systematic errors in the differential acceptances are said to "include the uncertainties in trigger simulation and detector efficiencies" and to be "small compared to the statistical errors in the data"; only these latter errors on the shape parameters are quoted. These statements are supported by the systematic error studies detailed in Section 6.6 of S. Takach's thesis (from which the results of the aforementioned paper are taken) ([41], pp.115-118). He finds the relative errors in n and b due to uncertainties in the MC weighting (Čerenkov and trigger efficiency) to be on the order of 1%. He also confirms that weighting to correct for the production distributions generated by the MC (a correction used in the present analysis only for absolute cross-section calculations) has a negligible impact on the shape parameters. In addition to these systematic errors, Takach estimates the error due to the procedure used to fit the mass plots. As this error is correlated to the dominant statistical error (which was larger for his results), we assess the importance of the former based on its ratio of the latter. This ratio is less than 0.5, indicating that any systematic component independent of the statistical error will be small.

One potentially significant systematic error in the differential acceptance which is not addressed in Takach's thesis is that associated with DC efficiencies, specifically uncertainty in the measured dimensions of the "DC holes", areas of diminished efficiency near the beam line. In Section 6.3 of his thesis on x_F-dependence in π^--induced D^+ production ([43], pp.94-95), Z. Wu provides some relevant information. In bins of x_F, he shows the average effect on acceptance due to $\pm 1\sigma$ variations in the widths of the DC holes. At higher values of x_F, the relative change in the acceptance is at most a few percent more than the effect in the x_F range where most of the data resides. Since only *differences* in the relative changes in acceptance at low and high x_F can effect the shape of the differential acceptance, this contribution to the systematic error must be negligible. In fact, the error is even much lower than the above discussion might imply, because the changes in acceptance obtained by varying

all DC hole widths together (by $\pm 1\sigma$) is a gross overestimate of the systematic error which should properly be associated with the independent uncertainties in the DC hole dimensions.

In the present analysis, combined D differential cross-sections are used to estimate systematic relative errors on the shape parameters. As discussed in Section 9.3.1, the standard n (b) parameter exhibits a systematic dependence on the upper (lower) limit chosen for the fit range. Rather than serving as evidence of systematic errors in well-defined fundamental quantities, this range dependence points to the inadequacy of these one-parameter functions as analytic forms for the differential distributions. Therefore, no systematic error is associated with n and b due to this effect; rather, these quantities are reported as range-dependent.

Fits to $d\sigma/dx_F$ and $d\sigma/dp_T^2$ also show some sensitivity to the choice made in the point at which to exclude bins for which the data signal was not well-measured. By adding an extra bin (at high x_F or p_T^2) to the number indicated by the default cutoff in signal significance (described in Section 9.3.1), this systematic error was estimated and found in all cases to be a fraction of the statistical error. As these errors are correlated, any independent systematic effect is even less significant and therefore negligible.

One final systematic error, applying to the combined D differential cross-section results, arises from the relative weights given D^+, D^0, and D_s acceptances in the composite average acceptance. These weights are calculated in Section 7.2.6. An overestimate of this error was obtained by varying the $D^+/D^0/D_s$ cross-section ratio assumed from 2:4:1 to 2:2:1; this changes n by about 30% of the statistical error. As shown in Figs. 7.11 and 7.12, differential acceptance shapes are insensitive to the identity of the D meson.

9.3 Results

9.3.1 Differential cross-sections

Combined D differential cross-section results for π, K, and p beams are given in Tables 9.1 and 9.2. While these and other results presented in this section are absolutely normalized using the results of Chapter 8, what shall concern us here are the *shapes* of these differential distributions. Differential cross-section shapes are commonly characterized by standard parametrizations which, while having some theoretical motivation, are justified primarily on a phenomenological basis (i.e., they give a decent fit to the data and/or theory). By fitting observed $d\sigma/dx_F$ and $d\sigma/dp_T^2$ distributions with these functional forms, we are able to quantify their shapes as a small number (1-3) of independent[7] parameters.

x_F range	$d\sigma/dx_F$ (μb/nucleon)		
	π beam	K beam	p beam
$-0.1 - 0.0$	17 ± 8	< 53	< 54
$0.0 - 0.1$	47 ± 3	48 ± 7	50 ± 7
$0.1 - 0.2$	35 ± 2	38 ± 4	31 ± 4
$0.2 - 0.3$	21.9 ± 1.4	24 ± 3	16 ± 3
$0.3 - 0.4$	11.4 ± 1.1	12 ± 2	3.5 ± 1.6
$0.4 - 0.5$	4.7 ± 0.8	5.2 ± 1.8	< 0.7
$0.5 - 0.6$	2.3 ± 0.6	4.2 ± 1.7	
$0.6 - 0.7$	1.1 ± 0.5	< 1.6	
$0.7 - 0.8$	< 1.1		

Table 9.1: E769 measurements of differential cross-sections vs. x_F for π, K, and p-induced D meson (D^+, D^-, D^0, $\overline{D}^0$, D_s^+, and D_s^-) production. In addition to the statistical errors shown, there are overall normalization errors of about 6%, 6%, and 9% for π, K, and p results, respectively. Inequalities are given for 90% confidence level upper limits.

[7]While the shape parameters are independent of one another, in general their errors, derived statistically using the fitter's minimization algorithm, are to some degree correlated.

p_T^2 range (GeV^2)	$d\sigma/dp_T^2$ (μb/(nucleon GeV^2))		
	π beam	K beam	p beam
$0-1$	8.3 ± 0.4	8.8 ± 0.8	6.2 ± 0.8
$1-2$	2.25 ± 0.16	2.6 ± 0.4	2.6 ± 0.4
$2-3$	0.90 ± 0.09	1.0 ± 0.2	0.69 ± 0.17
$3-4$	0.45 ± 0.06	0.56 ± 0.14	0.24 ± 0.10
$4-5$	0.28 ± 0.04	—	0.16 ± 0.07
$4-6$	—	0.07 ± 0.04	—
$5-6$	0.08 ± 0.02	—	0.11 ± 0.06
$6-7$	0.07 ± 0.02	—	—
$6-8$	—	0.06 ± 0.03	0.05 ± 0.03
$7-8$	0.025 ± 0.013	—	—
$8-10$	0.019 ± 0.007	< 0.02	< 0.02
$10-12$	0.006 ± 0.005		
$12-14$	0.007 ± 0.004		
$14-16$	< 0.005		

Table 9.2: E769 measurements of differential cross-sections vs. p_T^2 for π, K, and p-induced D meson (D^+, D^-, D^0, $\overline{D}^0$, D_s^+, and D_s^-) production. Description in Table 9.1 caption applies.

Theoretically-predicted $d\sigma/dx_F$ distributions, both for charm quarks (NLO QCD) and charm mesons (Lund MC), are well-fit in the x_F range accessible to E769 ($-0.1 < x_F < 0.8$) by the 3-parameter function defined in Equation 2.7. The former fits, described in Section 2.6.2, are used later in this section to compare measurements with theory; the latter fits determine the differential distribution correction functions (see Section 7.2.3) used to weight the MC in the absolute cross-section analysis. In fitting measured $d\sigma/dx_F$ distributions in the forward hemisphere, however, the following standard 1-parameter function (hereafter called the "n-form") is sufficient:

$$\frac{d\sigma}{dx_F} = N\ (1 - |x_F|)^n. \tag{9.9}$$

Although the data presented here does give some limited indication of the behavior

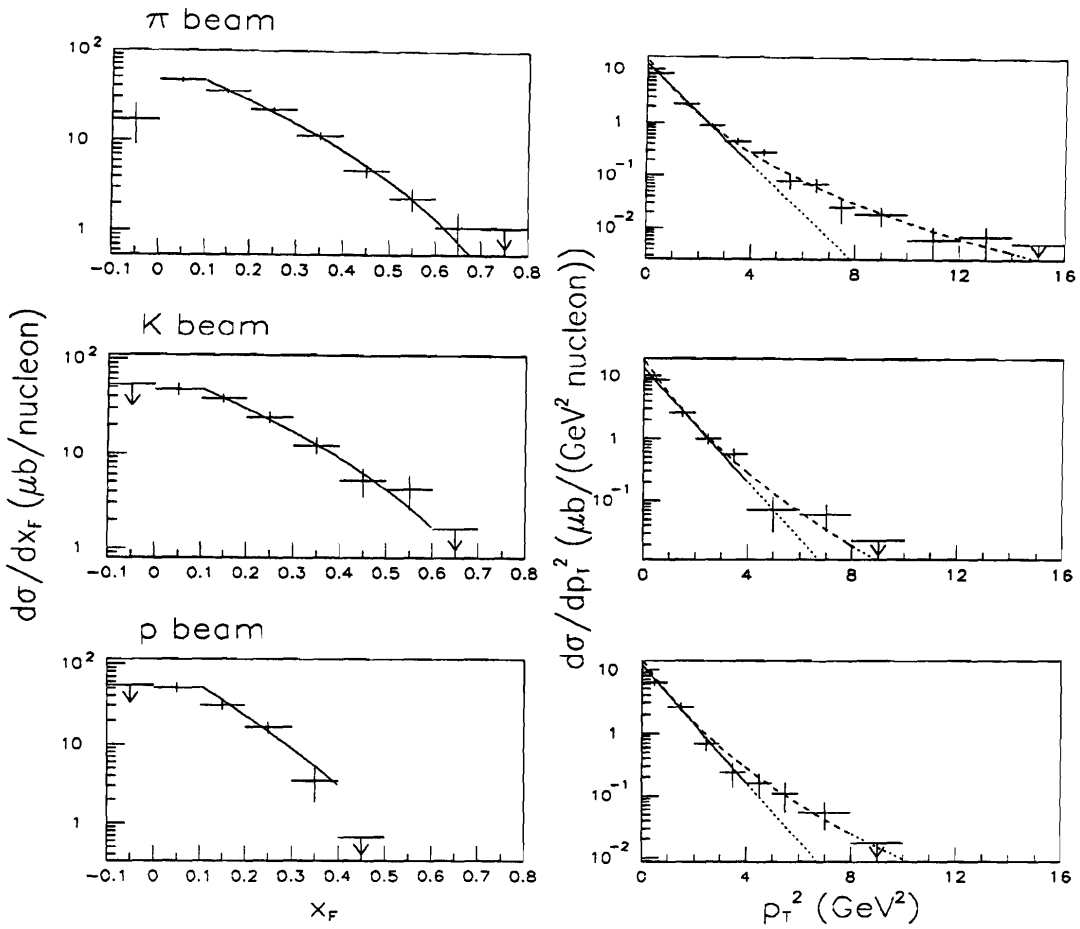

Figure 9.1: Combined D differential cross-sections with parametrization fits. Versus x_F (p_T^2), n-form (b-form) fits are indicated by a solid line. Fits of $d\sigma/dp_T^2$ using the FMNR form are shown as a dashed line. Extrapolations of fits beyond the fit range used are indicated by dotted lines.

of the cross-section in the backward hemisphere, negative-x_F cross-sections are not measured with enough precision to yield significant information about the "central" shape parameters x_c and x_b (defined in text following Equation 2.7). Use of the form of Equation 9.9 assumes, contrary to expectation in the case of π-induced production, that $d\sigma/dx_F$ is symmetric about zero. Furthermore, this function's discontinuous derivative at zero x_F gives it an unphysical cusp. Nevertheless, as stated above,

the shapes of measured $d\sigma/dx_F$ distributions in the full forward hemisphere can be characterized by the single "tail" parameter n. The usefulness of this parametrization is discussed further when results of the fits to data are presented later in this section.

Versus p_T^2, the 2-parameter FMNR form

$$\frac{d\sigma}{dp_T^2} = N\ (\alpha m_c^2 + p_T^2)^{-\beta}, \tag{9.10}$$

where m_c is the mass of the charm quark (set to 1.5 GeV), gives good fits to data (as well as theory) over the full p_T^2 range over which D meson signals are obtained (0-16 GeV^2). For the more precisely-measured distributions, this form supplants the following two forms, which provide acceptable fits to the data only at low and high p_T^2, respectively:

$$\frac{d\sigma}{dp_T^2} = N\ \exp -bp_T^2 \tag{9.11}$$

$$\frac{d\sigma}{dp_T^2} = N'\ \exp -b'\sqrt{p_T^2} = N'\ \exp -b'p_T. \tag{9.12}$$

The first exponential (b-form) is found to give poor-quality fits to the more precisely-measured distributions, even given the limited range in which it is used (0-4 GeV^2, unless otherwise specified). Unlike the FMNR function, however, the b-form has been used by numerous experimental collaborations to parametrize their results. The second exponential (b'-form) is found to give good fits to the data in the full range above p_T of 1 GeV.

In Figs. 9.1 through 9.6, we present plots of $d\sigma/dx_F$ and $d\sigma/dp_T^2$ for the combined D as well as the individual D meson species. Distributions for π, K, and p beams are each shown except in cases where the data is too scarce to break up into bins. As with the forward cross-sections (see discussion in Section 8.3.2), combined π and K beam results are used in comparisons with previous measurements made using negative meson beams. In Section 9.3.2, positive and negative π and K beam results are compared.

In the aforementioned plots, least-squares fits to $d\sigma/dx_F$ and $d\sigma/dp_T^2$ are also shown. The former distributions are fit using the n-form; although this form can be

Beam	x_F range	n	χ^2/dof	C.L.[a] (%)
π	> 0.1	4.4 ± 0.2	0.5	76
	> 0.0	4.03 ± 0.18	1.5	19
K	> 0.1	4.2 ± 0.5	0.4	72
	> 0.0	3.8 ± 0.4	0.7	57
p	> 0.1	7.1 ± 1.1	2.3	13
	> 0.0	6.1 ± 0.7	2.0	13

[a]confidence level (χ^2 upper-tail probability).

Table 9.3: Combined D $d\sigma/dx_F$ fit results.

Beam	p_T^2 range (GeV^2)	b (GeV^{-2})	χ^2/dof	C.L. (%)
π	0 - 4	1.08 ± 0.05	6.8	0.1
K	0 - 4	1.05 ± 0.09	1.7	18
	> 0	1.04 ± 0.08	1.7	15
p	0 - 4	1.08 ± 0.09	0.7	48
	> 0	0.99 ± 0.08	1.4	22

Table 9.4: Combined D $d\sigma/dp_T^2$ fit results, b-form.

used to fit $d\sigma/dx_F$ for all positive x_F, fits over the more limited range $x_F > 0.1$ are shown, primarily to follow the precedent set in earlier E769 differential cross-section papers [6, 9].[8] The p_T^2 distributions are fit using the b-form (solid line) in the p_T^2 range 0-4 GeV^2 and, in cases with data available beyond this range, the FMNR form (dashed line) over the full p_T^2 range. For both x_F and p_T^2 fits, the fitting functions used integrate given parametrizations over the width of a bin rather than returning the value at the bin center. The fits are done using all bins (in the range appropriate to

[8]In [6], inclusion of the first positive x_F bin led to a poor n-form fit to the combined D data. The x_F range in [9] was kept the same to facilitate comparison of D^* results with those presented in [6].

Beam	α	β	χ^2/dof	C.L. (%)
π	1.4 ± 0.3	5.0 ± 0.6	1.1	35
K	2.4 ± 1.6	7.6 ± 3.7	1.5	22
p	2.2 ± 1.5	6.6 ± 3.3	1.2	33

Table 9.5: Combined D $d\sigma/dp_T^2$ fit results, FMNR form.

Beam	p_T range (GeV)	b' (GeV^{-1})	χ^2/dof	C.L. (%)
π	1.0 - 3.742	2.74 ± 0.09	1.4	19
	1.0 - 2.449	2.58 ± 0.10	2.1	10
	0.0 - 3.742	2.28 ± 0.04	6.5	0
K	1.0 - 2.828	3.0 ± 0.3	1.7	17
p	1.0 - 2.828	3.0 ± 0.3	0.6	64

Table 9.6: Combined D $d\sigma/dp_T^2$ fit results, b'-form.

the parametrization) which have at least a 2σ signal (or are bounded by two bins that do). Upper limits[9] are shown for those bins which do not satisfy the above criteria but are adjacent to ones that do. The numerical values of the shape parameters returned by the fitter and information about the quality of the fits are given in Tables 9.3 through 9.14.

In Fig. 9.2, combined D $d\sigma/dp_T^2$ fits using the b'-form are plotted. As can be seen from the unusual binning used, the independent variable is transformed from p_T^2 to p_T by simply taking the square roots of the bin edges and rebinning the histograms. The results of these fits are given in Table 9.6.

As mentioned in Section 9.2, the n and b parameters exhibit a systematic dependence on the fit range chosen. As shown by the combined D $d\sigma/dx_F$ fit results

[9]For empty bins, Poisson statistics are used to obtain the 90% C.L. upper limit (2.3 events divided by the acceptance); for the rest, this limit is calculated through a Bayesian integration of a Gaussian, as described in Section 8.3.1.

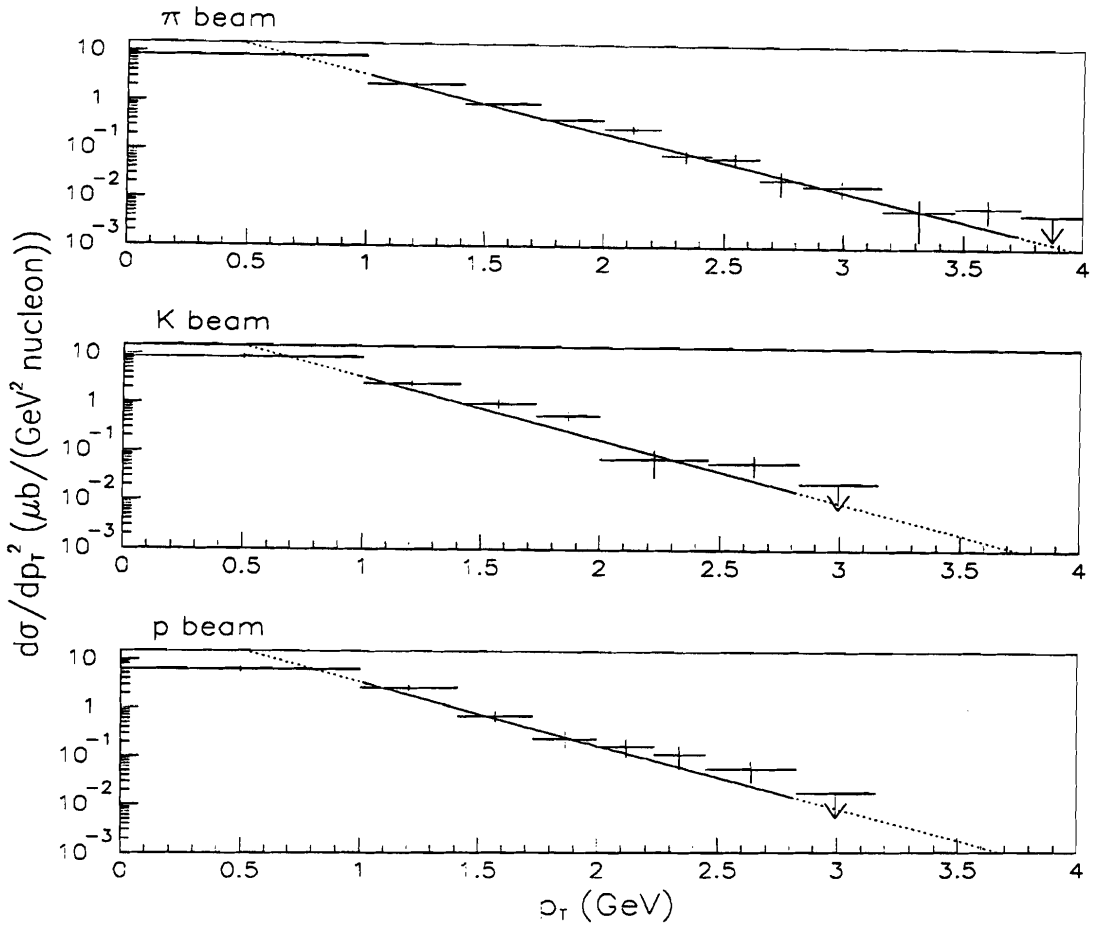

Figure 9.2: Combined $D\ d\sigma/dp_T^2$ (μb/GeV^2) vs. p_T (GeV). Fits using the b'-form are shown as a solid line. Extrapolations beyond the fit range used are indicated by dotted lines.

reported in Table 9.3, the inclusion of the 0.0-0.1 x_F bin in the fit decreases n it by 1-2σ. The use of the standard b-form to fit $d\sigma/dp_T^2$ is also problematic; as indicated by the good data fits obtained using the FMNR form, the cross-section dies out at high transverse momentum much more slowly than is consistent with exponential behavior in p_T^2. Therefore, data fits using the b-form are poor for the well-measured distributions. Even when the b-form fits the data acceptably, b decreases systematically as more of the high-p_T^2 tail is included in the fit range.

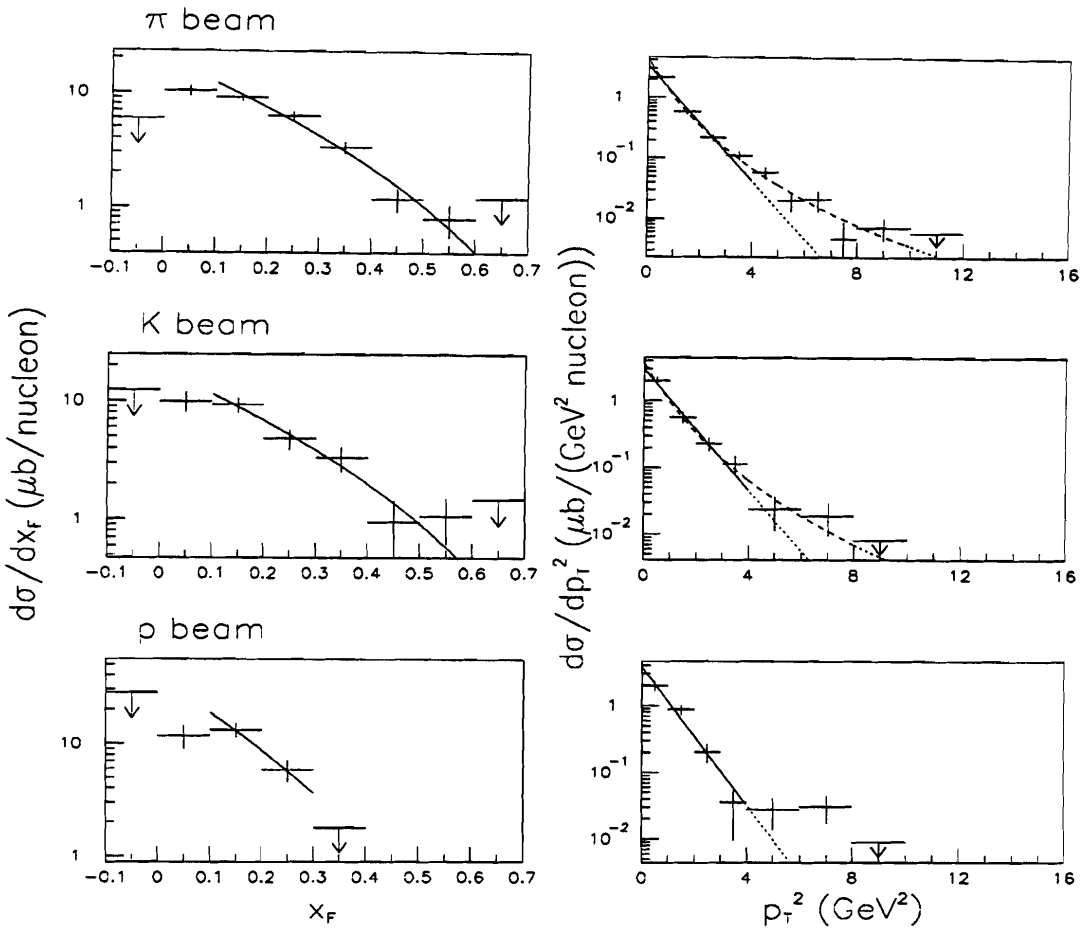

Figure 9.3: D^+ differential cross-sections. See Fig. 9.1 caption.

With these caveats in mind, we can make comparisons to previous measurements of differential cross-section shapes by comparing the standard n and b shape parameters. The FMNR form has not previously been used to fit data, and only E769 has reported b' values (see below). Previous measurements of combined D[10] (D^*) shape parameters are given in Tables 9.15 through 9.17 (Table 9.18). Note the different ranges in x_F and p_T^2 used by the various experiments as well as the changes in beam energy. Theory

[10]The combined D sample used by other experiments and in earlier E769 analyses does not include D_s.

Beam	n	χ^2/dof	C.L. (%)
π	4.2 ± 0.3	1.5	22
K	4.3 ± 0.7	.8	48
p	6.6 ± 2.1	—	—

Table 9.7: D^+ $d\sigma/dx_F$ fit results.

Beam	b (GeV^{-2})	χ^2/dof	C.L. (%)	α	β	χ^2/dof	C.L. (%)
π	1.10 ± 0.06	3.5	3	1.3 ± 0.4	4.7 ± 0.9	0.7	66
K	1.05 ± 0.12	0.9	40	1.4 ± 1.2	5.0 ± 2.9	0.6	64
p	1.19 ± 0.11	1.8	17				

Table 9.8: D^+ $d\sigma/dp_T^2$ fit results.

predicts that as beam energy rises from 200 to 800 GeV, n should rise by about 45% (30%) for $\pi(p)$-N charm production; over the same range in beam energy, b is expected to drop by about 20% (25%) [26].

For π, K, and p beams, the n and b results of the present analysis are largely consistent with previous measurements (including those of E769). Although for π-induced D production, the published b values tend to be significantly lower than those of E769, this can probably be attributed to the much larger p_T^2 ranges used in determining the former. In addition, the present analysis has not led to a significant change in the b' value obtained previously by E769 [6] for π-induced D production: 2.76 ± 0.08 GeV^{-1}, over a p_T range very similar to that used in this analysis. Not enough precise measurements are available to assess the accuracy of the energy dependence of the differential cross-section shapes predicted (for quarks) by perturbative QCD. The magnitudes of n and b expected from theory, however, are consistent with the trend in the data. At E769's beam energy, n is predicted to be about 4 (6.5) for

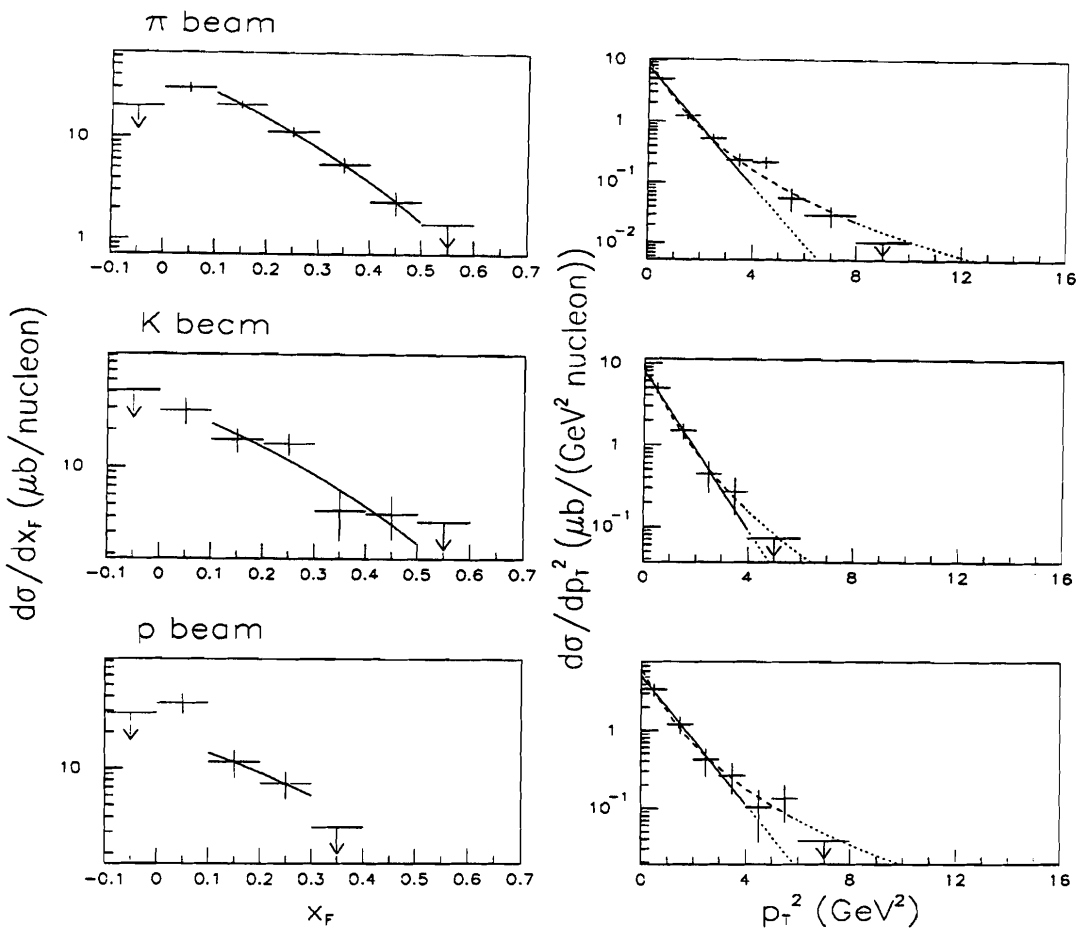

Figure 9.4: D^0 differential cross-sections. See Fig. 9.1 caption.

$\pi(p)$-induced production; b is predicted to be close to 1 GeV^{-2} in both cases [26].

As detailed in Section 2.6, NLO QCD predictions of the shapes of charm quark differential cross-sections (versus x_F and p_T^2) are generated for both π and p beam using the program of Mangano *et al.*; good fits to these distributions are obtained. Fits of the combined D measured distributions to theory, with the normalization kept floating, are carried out as parametrization-independent tests of the agreement between theory and data. The results of these fits are given in Tables 9.19 and 9.20.

Remarkably, D meson $d\sigma/dx_F$ distributions induced by π and p beams are well-fit

Beam	n	χ^2/dof	C.L. (%)
π	4.9 ± 0.5	0.03	97
K	3.8 ± 1.0	1.7	18
p	3.2 ± 2.9	—	—

Table 9.9: D^0 $d\sigma/dx_F$ fit results.

Beam	b (GeV^{-2})	χ^2/dof	C.L. (%)	α	β	χ^2/dof	C.L. (%)
π	1.11 ± 0.08	3.0	5	1.0 ± 0.4	4.0 ± 0.9	1.2	29
K	1.12 ± 0.16	0.4	66	1.4 ± 2.9	4.9 ± 7.3	0.3	56
p	0.96 ± 0.16	0.4	70	0.9 ± 1.1	3.3 ± 2.3	0.4	79

Table 9.10: D^0 $d\sigma/dp_T^2$ fit results.

by the corresponding predictions for charm quarks. These latter shapes are found to be insensitive to variation of parameters typically used to gauge theoretical uncertainty (m_c, μ_R, μ_F) [32, 37]. Furthermore, the π and p beam predictions for $d\sigma/dx_F$ are quite distinct, the former being significantly harder and peaking at 0.03 rather than being symmetric about x_F of zero. Consequently, the precision of the data is more than sufficient for the expected difference in π and p-induced production to be measured; the shape of the π (p) beam distribution is inconsistent with that of the p (π) beam theory. The K beam data is well-fit by the π beam theory, indicating similarity in pion and kaon gluon distributions.

The predicted separation between π and p-induced charm production is not as pronounced for $d\sigma/dp_T^2$ as it is for $d\sigma/dx_F$; the π beam distribution is expected to be somewhat harder. These shapes, further, show a dependence on moderate variations in m_c ($\pm$ 0.3 GeV) which is similar for both beams and on the order of the difference between them (see Section 2.6). The K and p beam shapes are fit well by either

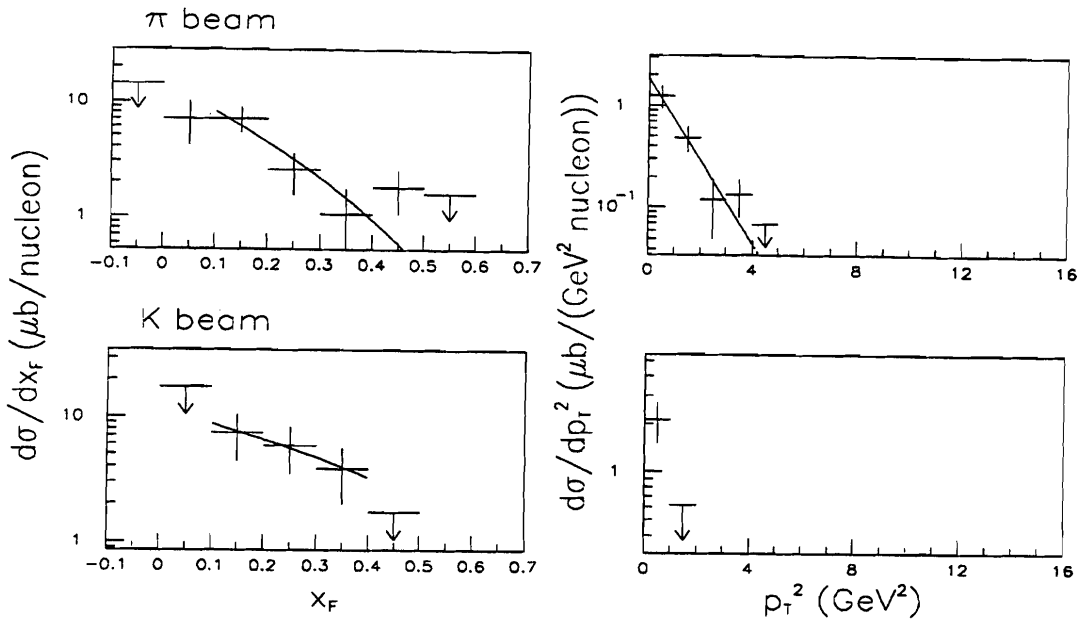

Figure 9.5: D_s differential cross-sections. See Fig. 9.1 caption.

Beam	n	χ^2/dof	C.L. (%)
π	5.3 ± 2.2	1.9	16
K	2.5 ± 2.3	0.02	88

Table 9.11: D_s $d\sigma/dx_F$ fit results.

theory curve. The π beam data distribution, however, while fit well by the theoretical distribution generated using π parton distributions for the beam, is inconsistent with the p beam theory.

These $d\sigma/dx_F$ and $d\sigma/dp_T^2$ data-theory comparisons are plotted in Figs. 9.7 and 9.8, respectively. Normalizations of the π (p) beam theory curves are floated for best fit to the π (p) beam data. It should be emphasized that the theory curves shown are for charm *quarks*; no attempt has been made to modify these predictions to

Beam	b (GeV^{-2})	χ^2/dof	C.L. (%)
π	0.9 ± 0.2	1.1	32

Table 9.12: D_s $d\sigma/dp_T^2$ fit results.

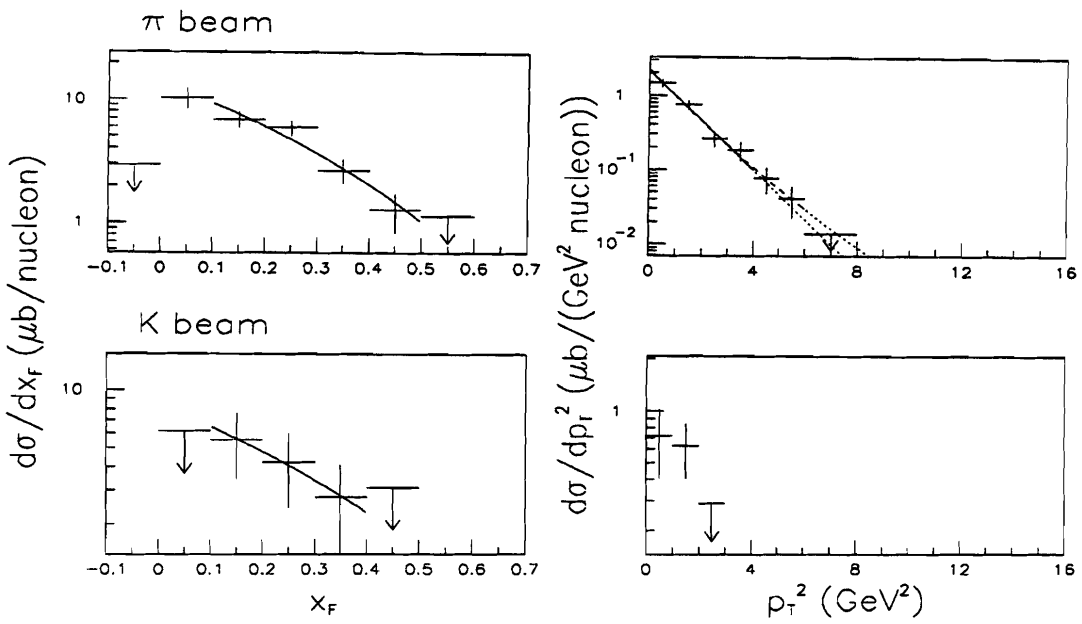

Figure 9.6: D^* differential cross-sections. See Fig. 9.1 caption.

incorporate non-perturbative effects such as intrinsic parton p_T and hadronization. At E769's level of precision, these corrections are evidently unimportant or fortuitously cancel out one another.

9.3.2 Beam particle dependence

As with the absolute cross-section results, we combine oppositely-signed π and K beam samples to obtain our most precise measures of the differential distributions

Beam	n	χ^2/dof	C.L. (%)
π	3.8 ± 0.6	1.3	28
K	2.6 ± 2.3	0.01	92

Table 9.13: D^* $d\sigma/dx_F$ fit results.

Beam	b (GeV^{-2})	χ^2/dof	C.L. (%)	α	β	χ^2/dof	C.L. (%)
π	0.77 ± 0.09	0.8	45	7.4 ± 9.3	14.0 ± 15.6	0.5	67

Table 9.14: D^* $d\sigma/dp_T^2$ fit results.

for the three E769 beam species (π, K, p). This procedure is supported by the arguments presented in Section 8.3.2. In fact, once issues of absolute normalization are ignored, dependence of the distribution shapes on beam particle charge should be further diluted because observed distributions are effectively averages of components which are not expected to be markedly dissimilar (e.g., gg fusion and $q\bar{q}$ annihilation). Results which support these assumptions are presented in this section.

By minimizing the χ^2 between two measured distributions (allowing the normalization of one of the distributions to float), we can obtain quantitative support (χ^2/dof, confidence level) for a statement concerning the (in)consistency of the shapes of the distributions. Of course, the range of the comparison is limited to that of the distribution measured with the lesser precision.

First, we carry out this procedure on the combined D differential distributions for oppositely-charged meson beams. Versus x_F, the π^-/π^+ (K^-/K^+) shape comparison fit returns a χ^2/dof of 1.7 (0.5), indicating consistency at the 14% (74%) confidence level. The evidence for consistency versus p_T^2 is slightly more compelling, with a χ^2/dof. of 1.0 (0.3) corresponding to a confidence level of 45% (79%). For each

Expt.	E_B (GeV)	# events	n (b (GeV^{-2}))	x_F range (p_T^2 range (GeV^2))
NA32	200	114	$2.5^{+0.4}_{-0.3}$	0.0 - 0.7
			$(1.06^{+0.12}_{-0.11})$	(0 - 5)
	230	792	$3.74 \pm 0.23 \pm 0.37$	0.0 - 0.8
			$(0.83 \pm 0.03 \pm 0.02)$	(0 - 10)
E769	250	1307	3.9 ± 0.3	0.1 - 0.7
(1992)			(1.03 ± 0.06)	(0 - 4)
WA75	350	459	3.5 ± 0.5	-0.5 - 0.5
			(0.77 ± 0.04)	(0 - 10)
NA27	360	57	3.8 ± 0.63	0.0 - 0.9
			$(0.83^{+0.18}_{-0.16})$	(0 - 10)
E653	600	676	$4.25 \pm 0.24 \pm 0.23$	> 0.0
			$(0.76 \pm 0.03 \pm 0.03)$	

Table 9.15: Previous measurements of combined D shape parameters, π beam [17,19,6,16,2,29].

individual D species, these findings are corroborated by the consistency of the n and b shape parameters determined for oppositely-charged meson beams. In Fig. 9.9, combined D π^- and π^+ distributions are plotted together.

Next, we turn to the combined D $d\sigma/dx_F$ and $d\sigma/dp_T^2$ results for π, K, and p beams. As expected from the inability of the π (p) beam $d\sigma/dx_F$ theory curves to fit the p (π) beam data, these two data distributions are found to be inconsistent at a greater than 99% confidence level ($\chi^2/dof > 4$).[11] Versus p_T^2, the distributions for π and p beams are found to be consistent. (Recall, however, that this comparison is only conducted over the range of the less-precisely measured distribution, in this case that for p beam.) For both $d\sigma/dx_F$ and $d\sigma/dp_T^2$, K and π beam results are found to be consistent.

[11]The confidence level for *inconsistency* is just 100% minus the confidence level for consistency, previously defined.

Expt.	E_B (GeV)	# events	n (b (GeV^{-2}))	x_F range (p_T^2 range (GeV^2))
NA32	200	34	4.7 ± 0.9	0.0 - 0.6
			$(2.7^{+0.7}_{-0.5})$	(0 - 3)
	230	31	$3.56^{+1.08}_{-0.99} \pm 0.36$	> 0.0
			$(1.36^{+0.32}_{-0.26} \pm 0.04)$	

Table 9.16: Previous measurements of combined D shape parameters, K beam [17,19].

Expt.	E_B (GeV)	# events	n (b (GeV^{-2}))	x_F range (p_T^2 range (GeV^2))
NA32	200	9	$5.5^{+2.1}_{-1.8}$	> 0.0
			$(1.4^{+0.6}_{-0.4})$	
NA27	400	119	4.9 ± 0.5	0.0 - 0.6
			(0.99 ± 0.09)	(0 - 7)
E653	800	96	$6.8^{+2.1}_{-1.9}$	> 0.0
			$(0.84^{+0.10}_{-0.08})$	
E743	800	31	8.6 ± 2.0	0.0 - 0.5
			(0.8 ± 0.2)	(0 - 6)

Table 9.17: Previous measurements of combined D shape parameters, p beam [17,4,30,12].

9.3.3 Hadronization

In principle, we expect hadronization to impact the differential distributions through such non-perturbative effects as color-dragging and leading-particle enhancement. The latter is largely eliminated by combining particle and antiparticle signals together, although differences could persist between neutral-leading production and the average of leading and non-leading production. In addition, the fraction of a particular D meson species that is *directly* produced is relevant.

Expt.	E_B (GeV)	# events	n (b (GeV^{-2}))	x_F range (p_T^2 range (GeV^2))
NA32	200	46	$2.8^{+1.1}_{-0.9}$	0.0 - 0.7
			$(0.9^{+0.3}_{-0.2})$	(0 - 5)
	230	147	$3.14^{+0.40}_{-0.39}$	0.0 - 0.8
			(0.79 ± 0.07)	(0 - 10)
E769 (1994)	250	519	3.5 ± 0.3	0.1 - 0.6
			(0.70 ± 0.07)	(0 - 4)
NA27	360	8.5	$4.3^{+1.8}_{-1.5}$	0.0 - 0.5
			(0.9 ± 0.4)	(0 - 3)

Table 9.18: Previous measurements of D^* shape parameters, π beam [17,19,9,3].

Data	Theory	χ^2/dof	C.L. (%)
π	π	1.9	6
π ($x_F > 0$)		.9	49
K		.5	77
p		5.0	0.2
π	p	20.5	0.00
π ($x_F > 0$)		20.0	0.00
K		6.3	0.00
p		0.9	43

Table 9.19: Data fits to theory shapes, $d\sigma/dx_F$.

In the differential cross-section analysis, the assumption has been made that, for the pseudoscalar mesons D^+, D^0, and D_s, the *differences* in these effects are too small to be seen, given the precision of our shape measurements. (The high-quality fits of charm quark theory to the measured distributions supports a stronger assumption, namely that the sum total of hadronization as well as other non-perturbative effects is itself small.)

Data	Theory	χ^2/dof	C.L. (%)
π	π	1.4	18
K		1.7	14
p		0.9	53
π	p	2.8	0.2
K		1.0	43
p		1.2	33

Table 9.20: Data fits to theory shapes, $d\sigma/dp_T^2$.

The consistency check described in the previous section is also used to justify the combination of the D^+, D^0, and D_s meson distributions into combined D distributions. Using the π beam distributions, we find that the x_F (p_T^2) distributions for the pseudoscalar mesons are all consistent with one another at a 12% (47%) or greater confidence level ($\chi^2/dof < 2\,(1)$).

The issue of direct versus indirect production (Section 8.3.3) is addressed by comparing combined D and D^* results (π beam) for the differential cross-section shapes. Recall that only about 25% of the combined D sample is produced directly. The x_F distributions are found to be consistent at a 70% confidence level. Versus p_T^2, however, the shape comparison fit returns a χ^2/dof of 2.5, indicating inconsistency at a greater than 97% confidence level. It is evident upon comparison of the pseudoscalar and vector D values of b that the emission of a pion or photon leading to indirect D production significantly softens the transverse momentum spectrum (corresponding to a higher b value) with respect to that of the parent D^*. We calculate the magnitude of this effect for the pion emission case:

$$\begin{aligned} p_T^2(D^*) &= (\boldsymbol{p}_T(D) + \boldsymbol{p}_T(\pi)) \cdot (\boldsymbol{p}_T(D) + \boldsymbol{p}_T(\pi)) \\ &= p_T^2(D) + p_T^2(\pi) + 2\, \boldsymbol{p}_T(D) \cdot \boldsymbol{p}_T(\pi). \end{aligned} \tag{9.13}$$

The transverse components of momenta are invariant under boosts along the beam

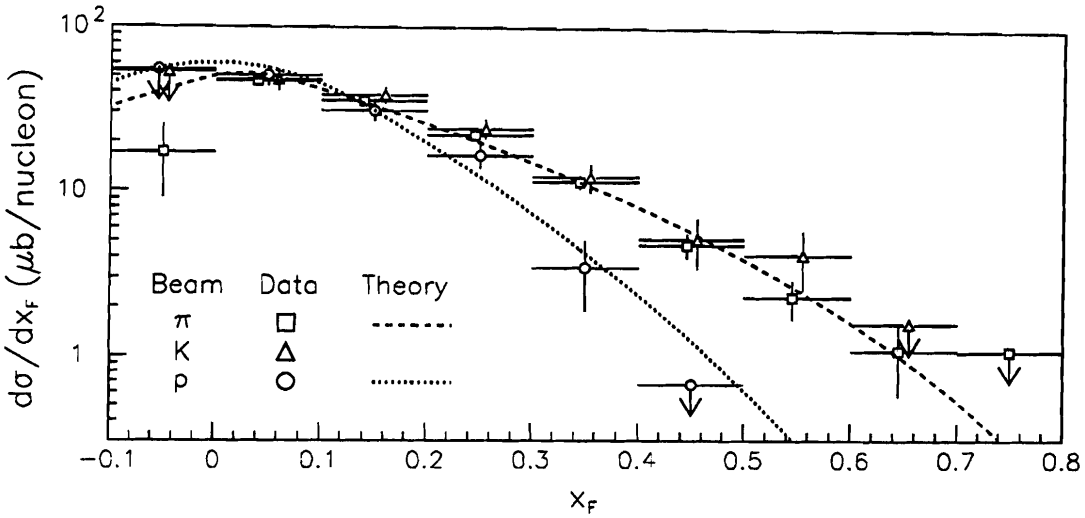

Figure 9.7: Measured D meson (D^+, D^-, D^0, $\overline{D}^0$, D_s^+, and D_s^-) $d\sigma/dx_F$ for production induced by π, K, and p beams and NLO QCD predictions [33] for charm quarks (π and p beams). In addition to the statistical errors shown, there are overall normalization errors of about 6%, 6%, and 9% for π, K, and p results, respectively. The abscissas of some data points are slightly offset to make them easily visible. Arrows indicate 90% confidence level upper limits.

axis; we choose to work in the frame where $p_L(D^*) = 0$. Within the transverse plane, we define the $x(y)$-axis as perpendicular (parallel) to the transverse momentum of the D^*. We now obtain an expression for the D^*-D difference in p_T^2:

$$\begin{aligned}
\Delta &\equiv p_T^2(D^*) - p_T^2(D) \\
&= p_T^2(\pi) + 2\, \boldsymbol{p}_T(D) \cdot \boldsymbol{p}_T(\pi) \\
&= p_x^2(\pi) + p_y^2(\pi) + 2\, (p_x(D)\, p_x(\pi) + p_y(D)\, p_y(\pi)). \qquad (9.14)
\end{aligned}$$

Assuming that the D^* is produced on average with no net polarization, the D and π are produced back-to-back in the D^* rest frame with an isotropic angular distribution. Let ϕ and θ be the azimuthal and polar angles in this (primed) frame, respectively. In this frame, $p(D)' = p(\pi)' \equiv p_{CM} \simeq 36$ MeV, allowing us to express Δ as follows:

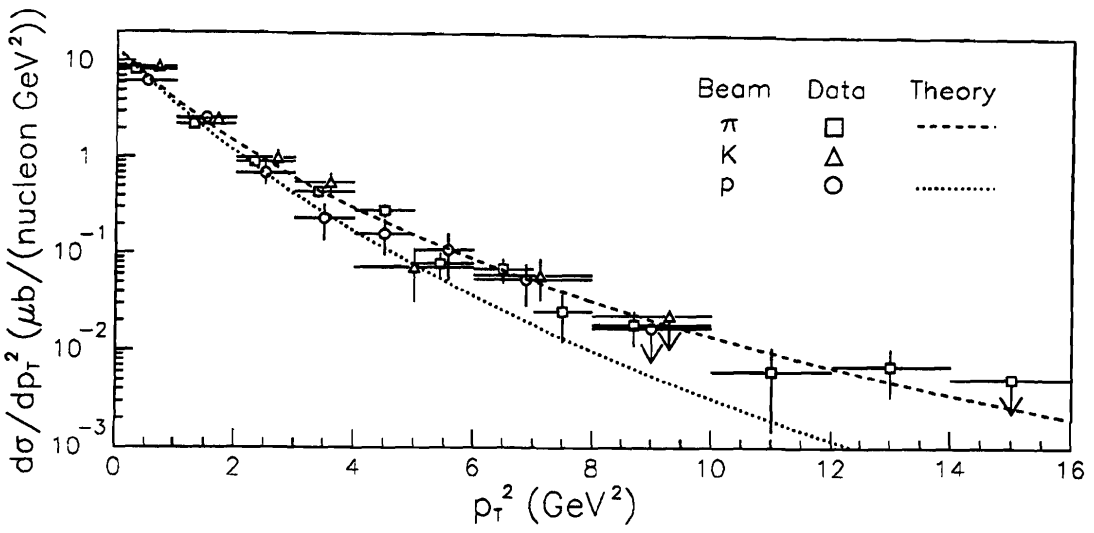

Figure 9.8: Measured D meson (D^+, D^-, D^0, $\overline{D}^0$, D_s^+, and D_s^-) $d\sigma/dp_T^2$ ($x_F > 0$) for production induced by π, K, and p beams and NLO QCD predictions [33] for charm quarks (π and p beams). See explanation in Fig. 9.7 caption.

$$
\begin{aligned}
\Delta &= p_x^2(\pi)' + \gamma^2\,(p_y(\pi)' + \beta\,E(\pi)')^2 + \\
&\quad 2\,(p_x(D)'\,p_x(\pi)' + \gamma^2\,(p_y(D)' + \beta\,E(D)')\,(p_y(\pi) + \beta\,E(\pi)')) \\
&= p_{CM}^2\,\cos^2\phi\,\sin^2\theta + \\
&\quad \gamma^2\,(p_{CM}^2\,\sin^2\phi\,\sin^2\theta - 2\,\beta\,p_{CM}\,E(\pi)'\,\sin\phi\,\sin\theta + \beta^2\,E^2(\pi)') - \\
&\quad 2\,[p_{CM}^2\,\cos^2\phi\,\sin^2\theta + \gamma^2\,(p_{CM}^2\,\sin^2\phi\,\sin^2\theta + \\
&\quad \beta\,p_{CM}\,(E(D)' - E(\pi)')\,\sin\phi\,\sin\theta - \beta^2\,E(D)'\,E(\pi)')], \qquad (9.15)
\end{aligned}
$$

where γ and β define the boost (in the transverse plane) from the D^* rest frame to our work frame.

Due to the low Q value of the D^* decay (5 MeV) with respect to the masses of the decay products, we can approximate the energies of the D and π in the primed frame with the masses of the respective particles. Averaging over the full solid angle, we obtain

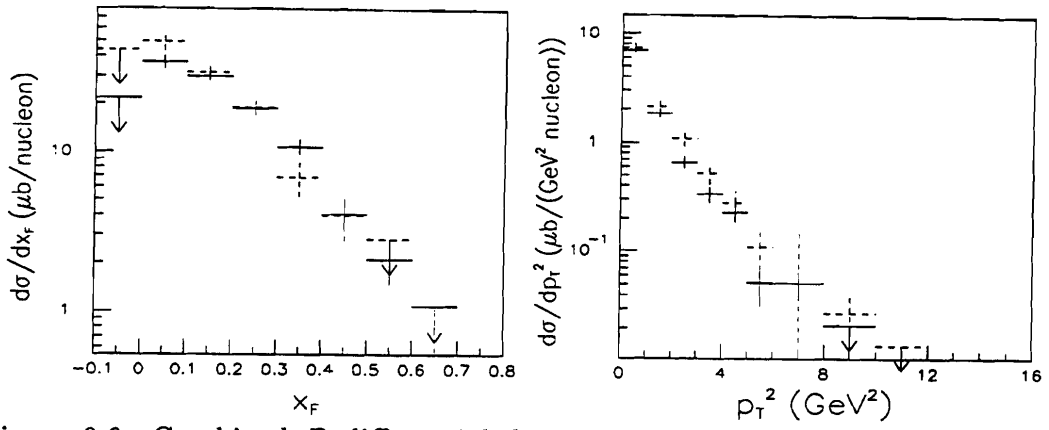

Figure 9.9: Combined D differential distributions compared for π^- (solid) and π^+ (dashed) beams. Left: $d\sigma/dx_F$ (μb/nucleon) vs. x_F, right: $d\sigma/dp_T^2$ (μb/(nucleon GeV^2)) vs. p_T^2 (GeV^2).

$$\begin{aligned}\Delta &= -\frac{p_{CM}^2}{3} + \gamma^2\,(\beta^2\,(2\,m_D + m_\pi)\,m_\pi - \frac{p_{CM}^2}{3}) \\ &= \frac{\beta^2}{1-\beta^2}\,[(2\,m_D + m_\pi)\,m_\pi - \frac{1}{3}\,p_{CM}^2\,\frac{2-\beta^2}{1-\beta^2}].\end{aligned} \tag{9.16}$$

Replacing β^2 with $p_T^2(D^*)/(m_{D^*}^2 + p_T^2(D^*))$, we obtain

$$\Delta = \frac{p_T^2(D^*)}{m_{D^*}^2}\,((2\,m_D + m_\pi)\,m_\pi - \frac{1}{3}\,p_{CM}^2) - \frac{2}{3}\,p_{CM}^2. \tag{9.17}$$

Plugging in numerical values, we obtain

$$\Delta = 0.13 \times p_T^2(D^*) - 0.86\,\mathrm{MeV}^2. \tag{9.18}$$

Assuming that $p_T^2(D^*)$ has an exponential distribution, only the first term on the right-hand side of the equation impacts the relationship between the b values of the parent and daughter D mesons; this constant fractional change in p_T^2 leads immediately to a prediction that $b(D)$ be higher than $b(D^*)$ by about 15%, assuming there is no direct D production and all D^*'s decay to a pion and a D. The prediction for photon emission is obtained by replacing m_π by p_{CM} (~70 MeV in this case) in the

above equations; the effect is about half as large, leading to only a 7% increase in the average b value of the daughter D over that of the D^*.

Our π beam results provide the best measure of the b parameter ratio:

$$\frac{b(\text{combined } D)}{b(D^*)} = 1.40 \pm 0.18. \tag{9.19}$$

Although most D^*'s undergo $D\pi$ decays, we expect the effects derived above to be diluted somewhat by direct production of pseudoscalar D's ($\sim$25% of total). These considerations lead to an expectation that the combined D b value be higher than that of the D^* by 10-15%; our measured results are consistent with this prediction.

Chapter 10

Conclusions

Fermilab E769 is the first experiment in which charm production induced by π, K, and p beams is studied at a common beam energy and using a single target and spectrometer. E769 data, obtained using negatively and positively-charged mixed hadron beams, provides unique information on the beam dependence of charm production. In addition to significant high-statistics contributions to current knowledge on π^- and p-induced production, E769 has published the first precise K^- beam measurements as well as the only measurements for π^+ and K^+. Moreover, few published charm cross-section measurements benefit from full mass reconstruction and identification and momentum determination of secondary particles. In this category, our data set represents a factor-of-two improvement in the number of π-induced charm decays; for K and p beams, ten and three-fold increases in statistics, respectively, are realized [17, 19, 2, 12].

In this thesis, we have presented measurements of forward production cross-sections for a number of charm mesons. Taken together, cross-sections of the pseudoscalar mesons and baryon[1] studied in E769 analyses are expected to constitute the bulk of the total charm cross-section. E769 results, together with previous data, are consistent with the energy dependence predicted by perturbative QCD. The sums of our measured cross-sections suggest a total charm cross-section which is higher than but consistent with theory. In addition to these absolute cross-section results, we

[1]See [10] for E769's Λ_c cross-section results.

have measured differential cross-sections $d\sigma/dx_F$ and $d\sigma/dp_T^2$ for D meson production with sufficient sensitivity to observe their dependence on the gluon distributions of the projectile particles, thereby providing new evidence of the relative hardness of the gluons in pions and kaons compared to those in protons. This agreement between experiment and theory reinforces the applicability of a perturbative framework for high-energy production of charm.

Appendix A

Glossary of Acronyms

DC	drift chamber
DISC	differential isochronous self-collimating Čerenkov counter
HMRSB	proton PDF of Harriman *et al.* [28]
LO	leading order
MC	Monte Carlo
NLO	next-to-leading order
FMNR	theorists Frixione, Mangano, Nason, and Ridolfi [26]
MNR	theorists Mangano, Nason, and Ridolfi [32]
NDE	theorists Nason, Dawson, and Ellis [36, 37]
PMT	photomultiplier tube
PDF	parton distribution function
PDG	particle data group [34, 35]
QCD	Quantum Chromodynamics
SMD	silicon microstrip detector
SMRS2	pion PDF of Sutton *et al.* [28]
TPL	Tagged Photon Lab
TRD	transition radiation detector

Bibliography

[1] LEBC-EHS (NA16) Collaboration, M. Aguilar-Benitez *et al.*, Phys. Lett. B **135**, 237 (1984).

[2] LEBC-EHS (NA27) Collaboration, M. Aguilar-Benitez *et al.*, Phys. Lett. **161B**, 400 (1985).

[3] LEBC-EHS (NA27) Collaboration, M. Aguilar-Benitez *et al.*, Phys. Lett. **169B**, 106 (1986).

[4] LEBC-EHS (NA27) Collaboration, M. Aguilar-Benitez *et al.*, Z. Phys. C **40**, 321 (1988).

[5] M. Aivazis, F. Olness, and W. Tung, Phys. Rev. D **50**, 3085 (1994); M. Aivazis, J. Collins, F. Olness, and W. Tung, Phys. Rev. D **50**, 3102 (1994).

[6] E769 Collaboration, G. A. Alves *et al.*, Phys. Rev. Lett. **69**, 3147 (1992).

[7] E769 Collaboration, G. A. Alves *et al.*, Phys. Rev. Lett. **70**, 722 (1993).

[8] E769 Collaboration, G. A. Alves *et al.*, Phys. Rev. Lett. **72**, 812 (1994).

[9] E769 Collaboration, G. A. Alves *et al.*, Phys. Rev. D **49**, 4317 (1994).

[10] E769 Collaboration, G. A. Alves *et al.*, Phys. Rev. Lett. **77**, 2388 (1996).

[11] E769 Collaboration, G. A. Alves *et al.*, Phys. Rev. Lett. **77**, 2392 (1996).

[12] LEBC-MPS (E743) Collaboration, R. Ammar *et al.*, Phys. Rev. Lett. **61**, 2185 (1988).

[13] B. Anderson, G. Gustafson, G. Ingelman, and T. Sjostrand, Physics Reports **97**, 32 (1983).

[14] B. Anderson, G. Gustafson, and B. Nilsson-Almquist, *A High Energy String Dynamics Model for Hadronic Interactions.* University of Lund, LU-TP-87-6, (1987).

[15] E691 Collaboration, J. C. Anjos *et al.*, Phys. Rev. Lett. **62**, 125 (1989).

[16] WA75 Collaboration, S. Aoki *et al.*, Prog. Theor. Phys. **87**, 1305 (1992).

[17] ACCMOR (NA32) Collaboration, S. Barlag *et al.*, Z. Phys. C **39**, 451 (1988).

[18] ACCMOR (NA32) Collaboration, S. Barlag *et al.*, Phys. Lett. B **247**, 113 (1990).

[19] ACCMOR (NA32) Collaboration, S. Barlag *et al.*, Z. Phys. C **49**, 555 (1991).

[20] M. Benot, J. Litt, and R. Meunier, Nucl. Instrum. Methods **105**, 431 (1972).

[21] S. J. Brodsky *et al.*, Phys. Lett. **93B**, 451 (1980).

[22] J. Collins, D. Soper, and G. Sterman, Nucl. Phys. **B263**, 37 (1986).

[23] B. L. Combridge, Nucl. Phys. **B151**, 429 (1979).

[24] D. Duke and J. Owens, Phys. Rev. D **30**, 49 (1984); J. Owens, Phys. Rev. D **30**, 943 (1984).

[25] D. Errede *et al.*, Nucl. Instrum. Methods Phys. Res., Sect. A **309**, 386 (1991).

[26] S. Frixione, M. Mangano, P. Nason, and G. Ridolfi, Nucl. Phys. **B431**, 453 (1994).

[27] K. Geiger, Phys. Rev. D **48**, 4129 (1993).

[28] P. Harriman *et al.*, Phys. Rev. D **42**, 798 (1990); P. Sutton *et al.*, Phys. Rev. D **45**, 2349 (1992).

[29] E653 Collaboration, K. Kodama *et al.*, Phys. Lett. B **263**, 573 (1991).

[30] E653 Collaboration, K. Kodama *et al.*, Phys. Lett. B **284**, 461 (1992).

[31] E653 Collaboration, K. Kodama *et al.*, Phys. Lett. B **316**, 188 (1993).

[32] M. Mangano, P. Nason, and G. Ridolfi, Nucl. Phys. **B405**, 507 (1993).

[33] M. Mangano, P. Nason, and G. Ridolfi, FORTRAN code HVQMNR, used to generate results presented in [32].

[34] Particle Data Group, J.J. Hernandez *et al.*, Phys. Rev. B **239**, (1990).

[35] Particle Data Group, L. Montanet *et al.*, Phys. Rev. D **50**, (1994).

[36] P. Nason, S. Dawson, and K. Ellis, Nucl. Phys. **B303**, 607 (1988).

[37] P. Nason, S. Dawson, and K. Ellis, Nucl. Phys. **B327**, 49 (1989).

[38] P. Nason, S. Frixione, and G. Ridolfi, in Proceedings of the XV International Conference on Physics in Collisions, Cracow, Poland, 1995, edited by M. Rozanka and K. Rybicki.

[39] R. Scalise, F. Olness, and W. Tung, in Proceedings of DPF96, Minneapolis, 1996.

[40] C. Stoughton and D. Summers, Computers in Physics, 6, 371 (1992); C. Gay and S. Bracker, IEEE Trans. on Nucl. Sci., NS-34, 870 (1987); S. Hansen *et al.*, IEEE Trans. on Nucl. Sci., NS-34, 1003 (1987).

[41] Takach, Stephen. "The Production Distributions of $D^{\pm}$ and $D^0/\overline{D}^0$ from $\pi^- N$ Interactions", Ph.D. dissertation, Yale University, May 1993.

[42] S. P. K. Tavernier, Rep. Prog. Phys. **50** 1439 (1987); J. Appel, Annu. Rev. Nucl. Part. Sci. **42**, 367 (1992).

[43] Wu, Zhongxin, "The Feynman-x Dependence of $D^{\pm}$ Mesons in π^--Nucleon Interactions", Ph.D. dissertation, Yale University, December 1991.